Diss. ETH No. 15793

Influence of Updrafts and Embedded Convection on the Microphysics of Riming

A dissertation submitted to the
SWISS FEDERAL INSTITUTE OF TECHNOLOGY
ZÜRICH

for the degree of
Doctor of Natural Sciences

presented by
BJÖRN BASCHEK
Dipl. Phys. University of Heidelberg
born May 4, 1974
citizen of Germany

accepted on the recommendation of
Prof. Dr. H. Davies, examiner
Dr. E. Barthazy, co-examiner
Prof. Dr. K. D. Beheng, co-examiner
Prof. Dr. H. Richner, co-examiner

2005

Contents

Abstract:

The connection between on one hand updrafts favoring condensation and prolonged residence times of hydrometeors in clouds and on the other hand riming – the accretion of supercooled cloud droplets onto pre-existing ice particles – is generally acknowledged. However, experimental observations of the riming degree of ice crystals together with a quantification of updrafts or embedded convective cells are scarce. Several questions could so far not be answered satisfactorily, for example: What are suitable means for definition and quantification of weak convection? What are the correlations to the microphysics of riming? What are the relevant scales of the embedded convection?

Weather in general and its forecast play an important role in everyday life and agriculture, but also for leisure time, and thus also for tourist industry. For a precise weather forecast, consideration of orographic effects and the prediction of precipitation are necessary but often not adequately represented in numerical weather prediction models. They could be ameliorated by a more detailed knowledge about the interplay of dynamics and microphysics, which would also yield a better interpretation of, for instance, radar data. Though the bulk part of the mid-latitude rainfall originates from so-called cold clouds, snow is so far less well investigated than rain, and riming is besides deposition and aggregation one of the fundamental snow growing mechanisms. Further, this process plays a crucial role for the transfer of, e.g., aerosols from the atmosphere into snow and rain, and thus on precipitation and soil chemistry. This investigation is thought to yield a deeper insight into and a better understanding of the microphysics of ice precipitation, especially of the influence of vertical winds and in stratiform precipitation embedded convection on riming.

Several partly contradictory definitions of convection exist, which are differing especially for weak convection. In this thesis further investigated was, firstly, the definition of convective precipitation as the presence of updrafts that are stronger than the particle fall velocity (CONV I). For a vertically pointing radar, this is equivalent to negative Doppler velocities, and is thus especially useful for the detection of embedded convective cells by means of such a radar. Secondly, a quantification of convection is received by defining convection as the strength of vertical wind velocity (CONV II) – here restricted to updrafts.

To find answers to the open questions, the field experiment **RAMS** (**R**iming, **A**ggregation and **M**ass of **S**now) was carried out at Mt. Rigi in the Swiss Alps by the Institute for Atmospheric and Climate Science (IAC*ETH*) at the Swiss Federal Institute of Technology (**ETH**), Zürich. A unique setup and instrumentation combine remote sensing with in-situ measurements: From a lower measurement station at the base of a mountain, a precipitating cloud is monitored by a mobile, vertically pointing X-band Doppler radar. Simultaneously, microphysical properties of the ice precipitation of the same cloud, especially the distribution of fall velocity, are measured in-situ at a second station close to the top of the mountain by the **H**ydrometeor **V**elocity and **S**hape **D**etector (**HVSD**). Additionally, the degree of riming (RIM) is determined by taking and analyzing Formvar replica of the ice precipitation. Setup and combination of techniques provide a multitude of information, but allow above all the interpretation of processes in the free atmosphere apart from both instrument sites: The Doppler velocity, measured by the radar, is a combination of particle fall velocity and vertical wind speed. The HVSD measures the particle fall velocities directly, and thus the vertical wind speed can be estimated on one height level. Data measured at the lower station is shifted by the time the specific region of the observed system needs to arrive at the upper station. The proposed lag time correction method is based on a cross-correlation of the data sets.

As part of this thesis, the modernized mobile vertically pointing X-band Doppler radar was tested. Further, a software was developed for data acquisition as well as for analysis. This instrument proves to have excellent properties with high time (1 s) and velocity (0.125 m s^{-1}) resolution. Especially this time resolution makes small scale structures visible, which has not been possible in the past.

Therefore, a measure for turbulence was introduced: the Doppler delta. It is defined as the difference between the momentary Doppler velocity and its average over time. This time determines the investigated scale of turbulence. If, as often in snow, the terminal particle fall velocity varies only little, the Doppler delta is equivalent to the deviation of vertical winds from their mean, and thus to turbulence. In this way, turbulent structures of a horizontal scale of approximately 1.6 ± 0.6 km could be shown as well as embedded convective cells with negative Doppler velocity of a size up to about 7.0 ± 2.5 km.

Finally, correlations between, on one hand, vertical winds and embedded convection and, on the other hand, riming can be investigated. Data were filtered on the basis of minimal rain rate and temperature, but also lag time and its correlation coefficients proved to be a powerful tool for filtering data. These ensure that the measurements of both sites were performed on the same region of the precipitation system. Embedded convection in form of negative Doppler velocities was only observed in combination with riming degrees of 3 or above. For the correlation between updrafts and degree of riming, an extension of the method to estimate vertical winds not only on one height level but over a 2 km thick layer showed particularly high correlation coefficients with very strong significance. For a case study chosen to analyze and present in detail, these had values of 0.78 and of 0.70 applying the same filtering rules to all data of the winter season 2002/2003 taken at Mt. Rigi. Thus, the strong influence that vertical winds have on the degree of riming could be shown, and especially that of winds in a thick layer – probably corresponding to the growth region.

However, the data show a considerable spread, but also riming on a given sample is not uniform: The average spread of riming on the filtered Formvar samples is 0.5 RIM, and could thus explain the standard deviation with respect to riming of 0.46 RIM found for the correlation for all cases. But several other possible contributions are discussed, as e.g, altering composition of hydrometeors on the way from above the radar to the upper measurement site. Or, there are possibly other influences on riming as, e.g., habit and size distribution of ice crystals and cloud droplets. Nevertheless, in the observed cases riming was always high, when strong updrafts were observed. This leads to a conceptual model that strong updrafts cause high riming - either by condensation or by an increased particle residence time. But if there are no strong updrafts present, there might be other sources of super-cooled cloud droplets that can lead to higher degrees of riming.

Titel: **Einfluss von Aufwinden und eingelagerter Konvektion auf die Mikrophysik der Bereifung**

Zusammenfassung:

Der Zusammenhang zwischen Aufwinden, die zu Kondensation und längeren Aufenthaltszeiten von Hydrometeoren in Wolken führen, und der Bereifung von Eisteilchen ist im Prinzip anerkannt. Bereifung oder auch Verreifung bezeichnet das Anfrieren unterkühlter Wolkentröpfchen an Eisteilchen. Allerdings sind Beobachtungen des Bereifungsgrades zusammen mit einer Quantifikation von Aufwinden bzw. in stratiformen Niederschlag eingelagerten Konvektionszellen selten. Einige Fragen konnten bisher nicht zufrieden stellend beantwortet werden, z. B.: Was sind geeignete Definitionen für Konvektion bzw. Methoden zur Quantifizierung? Welche Korrelationen bestehen zur Mikrophysik der Bereifung? Was sind relevante Skalen?

Das Wetter im Allgemeinen und seine Vorhersage spielen eine wichtige Rolle in unserem Alltag, für Landwirtschaft und Freizeit und damit auch für die Tourismusindustrie. Für eine genaue Wettervorhersage sind die Berücksichtigung orographischer Effekte und die daraus resultierenden Niederschläge von grosser Bedeutung, was in numerischen Wettervorhersagemodellen oft nicht angemessen vertreten ist. Diese könnten verbessert werden, wenn das Zusammenspiel von Dynamik und Mikrophysik besser bekannt wäre, was z.B. auch zu einer besseren Interpretationsmöglichkeit von Radarbildern führen würde. Obwohl der Grossteil des Regens mittlerer Breiten aus so genannten kalten Wolken fällt, ist Schnee bisher weniger erforscht als Regen. Für Schnee aber ist die Bereifung neben Deposition und Aggregation einer der fundamentalen Wachstumsprozesse und spielt auch eine wichtige Rolle für das Auswaschen von z.B. Aerosolen aus der Luft und damit für die Niederschlags- und Bodenchemie. Diese Untersuchung hat das Ziel einen tieferen Einblick in die Niederschlagsmikrophysik zu gewinnen; insbesondere hinsichtlich des Einflusses von Vertikalwinden und in stratiformen Niederschlag eingelagerter Konvektion auf die Bereifung.

Es gibt einige, teilweise widersprüchliche Definitionen von Konvektion. Die Unterschiede spielen besonders bei schwacher Konvektion eine Rolle. In der hier vorliegenden Arbeit werden zwei Definitionen näher untersucht: Erstens dass Konvektion herrscht, wenn die Aufwindgeschwindigkeiten stärker sind als die Fallgeschwindigkeit der Niederschlagsteilchen. Dies ist für ein Vertikalradar gleichwertig mit negativen Dopplergeschwindigkeiten und deshalb ist diese Definition besonders nützlich, um eingelagerte Konvektion mit Hilfe eines Radars zu finden. Zweitens wird Konvektion als die Stärke des hier auf Aufwinde beschränkten Vertikalwindes definiert, was gleichzeitig als Quantifikation dient.

Um Antworten auf die oben aufgeführten Fragen zu finden, wurde am Berg Rigi in den Schweizer Alpen durch das Institut für Atmosphäre und Klima der Eidgenössischen Technischen Hochschule (IAC*ETH*) das Feldexperiment **RAMS** (**R**iming, **A**ggregation and **M**ass of **S**now) durchgeführt. Ein einzigartiger Messaufbau und die Instrumentierung kombinieren Fernerkundung mit In-situ-Messungen: An einer unteren Station steht ein mobiles Vertikalradar, das nahende Niederschlagsgebiete beobachtet. Parallel dazu werden mikrophysikalische Messungen von derselben Wolke kurz unterhalb der Spitze des Berges durchgeführt. Ein Schneespektrograph (**HVSD**) misst hier Grössen- und Geschwindigkeitsverteilungen der Hydrometeore und Formvar-Proben geben Aufschluss über den aktuellen Bereifungsgrad (RIM). Der Messaufbau und die Kombination der Techniken liefern nicht nur eine Vielzahl von Information, sondern sie ermöglichen vor allem auch die Interpretation von Prozessen, die in der freien Atmosphäre entfernt von beiden Instrumenten stattfinden: Denn die durch das Radar gemessene Dopplergeschwindigkeit ist eine Kombination

aus den Geschwindigkeiten des Vertikalwindes und der anwesenden Teilchen. Da letztere vom Schnee-spektrographen direkt gemessen wird, kann die Vertikalwindgeschwindigkeit auf einer Höhe abgeschätzt werden. Hierzu werden die Daten der unteren Station um die Zeit verschoben, die die entsprechende Region des beobachteten Systems braucht, um an der oberen Station anzukommen. Die vorgeschlagene Methode zur Korrektur der Zeitverschiebung basiert auf einer Kreuzkorrelation der Datensätze.

Als Teil dieser Doktorarbeit wurde das modernisierte mobile Vertikalradar (X-Band) getestet. Zusätzlich wurde eine Software zur Datenerfassung und Analyse entwickelt. Dieses Instrument zeigt hervorragende Eigenschaften mit hoher Zeit- (1 s) und Geschwindigkeitsauflösung (0.125 m s^{-1}). Besonders die hohe Zeitauflösung macht kleinskalige Strukturen sichtbar, was zuvor nicht machbar war.

Deshalb wurde ein Mass für Turbulenz eingeführt: Das Doppler-Delta ist definiert als die Differenz aus momentaner Dopplergeschwindigkeit und deren Mittelwert über eine Zeit, die gleichzeitig die Skala der untersuchbaren Turbulenz bestimmt. Wenn – wie oft in Schnee – die Fallgeschwindigkeit nur wenig variiert, ist das Doppler-Delta äquivalent zur Abweichung des Vertikalwindes von seinem Mittelwert und damit zu Turbulenz. So konnten sowohl turbulente Strukturen mit einer horizontalen Skala von ungefähr 1.6 ± 0.6 km als auch eingelagerte Konvektionszellen von einer Grösse bis zu 7.0 ± 2.5 km mit negativer Dopplergeschwindigkeit gezeigt werden.

Zur Untersuchung der Korrelation von Vertikalwind und eingelagerter Konvektion zur Bereifung, wurden die Daten auf der Basis einer minimalen Regenrate und Temperatur gefiltert. Auch die Methode zur Korrektur der Zeitverzögerung hat sich als wertvoll zur Datenfilterung erwiesen. Mit ihr kann überprüft werden, ob an beiden Stationen dasselbe Gebiet des Niederschlagssystems untersucht wurde. Einge-lagerte Konvektion in Form negativer Dopplergeschwindigkeiten wurde nur in Zusammenhang mit RIM grösser 3 beobachtet. Für die Korrelation zwischen Aufwinden und Bereifung zeigte eine Erweiterung der Methode zur Schätzung des Vertikalwindes besonders hohe Korrelationskoeffizienten mit sehr hoher Sig-nifikanz. Hierbei wird nicht nur die Dopplergeschwindigkeit auf einer Höhe verwendet sondern ein Mittel über eine 2 km dicke Höhenschicht oberhalb der oberen Station. Für eine genauer präsentierte Fallstudie wurden Korrelationskoeffizienten von 0.78 bzw. von 0.70 nach Anwendung der Filterung auf alle an dem Rigi durchgeführten Fälle des Winters 2002/2003 gefunden. Damit wurde der starke Einfluss von Ver-tikalwinden, insbesondere aus einer vermutlich der Wachstumsregion entsprechenden Schicht, auf die Bereifung gezeigt.

Die Daten (für alle Fälle) weisen mit einer Standardabweichung von 0.46 RIM eine beachtliche Streuung auf. Dies könnte damit erklärt werden, dass auch die Bereifungsgrade innerhalb einer Formvar-Probe nicht einheitlich sind: Die mittlere Streuung auf den gefilterten Formvar-Proben ist 0.5 RIM. Andere mögliche Ursachen sind z.B. Veränderungen der Zusammensetzung der Hydrometeore auf dem Weg zwischen den Messpunkten oder andere Einflüsse wie z.B. Habitus und Grössenverteilung von Eiskristallen und Wolkentropfen. In den untersuchten Fällen wurde jedoch bei starken Vertikalwinden immer eine starke Bereifung gemessen. Dies führt zu dem konzeptionellen Modell, dass starke Aufwinde, sei es durch erhöhte Aufenthaltsdauer der Teilchen oder durch Kondensation, immer starke Verreifung verursachen. Falls aber keine starken Aufwinde herrschen, existieren möglicherweise andere Quellen von unterkühlten Wolkentröpfchen, die zu höheren Bereifungsgraden führen.

Chapter 1

Introduction

"Det som göms i snö, ...

... kommer fram i tö."

Swedish saying

1.1 Motivation

"What is hidden in snow, abounds in thaw." This Swedish saying wants to express that, what is in winter hidden from the eye under a beautiful snow cover, becomes visible in spring when thaw starts. But this saying does not only make sense in its literally meaning, we can also apply it in a figurative sense, that in everything a secret is hidden that may be revealed: for instance, we could apply the saying to falling *snow*, where still many secrets are hidden. Though there are many open questions about the precipitation process in general, *snow* is so far less well investigated than its *melted* state: the rain. Additionally, many theories or measurement methods originally developed for rain can be used as a starting point for the investigation of falling snow or ice precipitation, respectively.

But – deviating from the proverb – all the year round, thus also in spring or summer, secrets remain hidden in snow: The bulk part of the mid-latitude rainfall originates from so-called cold clouds, where the temperature is below $0\,^\circ$C and frozen and liquid precipitation particles can coexist (Houze, 1993).

For ice precipitation, riming – the accretion of supercooled cloud droplets onto pre-existing ice particles – is besides deposition and aggregation one of the fundamental snow growing mechanisms. Besides, this process plays a crucial role for scavenging, the transfer of aerosols (or e.g.

1

pollutants) from the atmosphere into snow and rain (e.g. Scott, 1978; Poulida et al., 1998; Dixon et al., 1995), and thus on precipitation and soil chemistry. An effect, in so-far related to riming as supercooled cloud droplets are involved, is the icing of air planes, which potentially holds the hazard of air crashes (e.g. Cooper et al., 1984).

Not only considering risks for avalanches by an establishing snow cover or possibilities for skiing, but also weather in general and its forecast play an important role in everyday life and agriculture, but for many even more for leisure time, and thus also for tourist industry. For a precise weather forecast, consideration of orographic effects and the prediction of precipitation are necessary but often not adequately represented in numerical weather prediction models. For that, a more detailed knowledge about the interplay of dynamics and microphysics would offer possibilities for amelioration, and could be incorporated in high resolution weather models. However, experimental observations of the riming degree of ice crystals together with a quantification of updrafts or embedded convective cells are scarce. This investigation is thought to gain a deeper insight into and a better understanding of the microphysics of precipitation, especially of riming.

1.2   Method

This study considers two different kinds of phenomena, a microphysical one – riming – and a dynamical one – updrafts and embedded convection, where it is hypothesized that they are strongly coupled. Here, the basic theoretical idea is, that updrafts favor condensational growth of droplets and additional nucleation of droplets, and thus enhance riming. In order to support this hypothesis measurements were performed in winter 2002/2003 at Mt. Rigi, Switzerland, during the field campaign **RAMS** (**R**iming, **A**ggregation, and **M**ass of **S**now) of the Institute for Atmospheric and Climate Science at the Swiss Federal Institute of Technology, Zürich.

The measurement setup used in RAMS offers a unique combination of instruments. The experimental work is performed by combining in-situ measurements with a remote-sensing technique. The main instrumental role in this thesis plays a mobile, vertically pointing X-band Doppler radar. It has recently been modernized to improve time and velocity resolution. A large part of the time required for this thesis has been used to develop a software for data acquisition and a multitude of tools for data analysis.

The basic principle is as follows: From the base of Mt. Rigi, the radar monitors the incoming precipitation. Methods were developed in this thesis to detect embedded convective cells and estimate vertical wind velocities. Because a vertically pointing radar measures as Doppler velocity a combination of vertical wind and particle fall velocity, is the combination with in-situ measurements of special importance: Vertical winds are estimated by comparing measurements of the mobile radar with data from the **H**ydreometeor **V**elocity and **S**hape **D**etector (**HVSD**). This instru-

ment measures at a second, higher situated station velocity and size distributions of hydrometeors – as the name indicates. This method for the estimation of vertical winds is presented in this thesis together with necessary algorithms for the correction of time lags between the two different measurement sites. With the so-called Formvar method snow particles are replicated, and later visually analyzed to determine the amount of accreted rime. Thus, correlations between, on one hand, vertical winds and embedded convection and, on the other hand, riming are investigated.

1.3 Scientific background

Ice particle properties and in-situ measurements: At the beginning of last century, "Snowflake Bentley", who was the son of a farmer in Virginia, dedicated his life to photographing snow crystals in their various shapes. These beautiful photos (Bentley and Humphreys, 1931) are an early visualization of ice particles. Later, Schaefer (1956) proposed a method in which falling ice particles are preserved in plastic. In this way, samples can be investigated under a microscope much later and even in a warm environment. This method is used in this thesis to visually analyze the amount of accreted cloud droplets on ice crystals; a classification scheme by Mosimann et al. (1994) is applied to determine the degree of riming. For instance, Harimaya and Sato (1989) disassembled snowflakes into their consisting crystals to determine the riming portion. More modern but also very expensive methods exist that make very detailed images but require complicated instrumentation: Fascinating images can be obtained with the help of low temperature scanning electron microscopy of single crystals as done by Rango et al. (2003).

Several authors have investigated the properties of single ice particles. Locatelli and Hobbs (1974) are often cited for their mass to diameter or diameter to fall velocity relations other examples for studies especially also for rimed particles are by Mitchell et al. (1990), Heymsfield and Kajikawa (1987) as well as by Zikmunda and Vali (1972). However, particles within a given diameter range show – a partly riming and habit dependent – spread of properties as, e.g., of velocities. To account for this, for instance, the HVSD offers possibilities to measure continuously the properties of hydrometeors in natural snow fall (Barthazy et al., 2004; Schefold, 2004). The study of Böhm (1989) provides a theory of hydrodynamics characteristics of ice particles. But measurements can give validation and tests for theory as well as microphysical modelling (e.g. Seifert, 2002; Klaassen, 1988). Because of conservation of mass, mass of ice particles is a parameter of special interest for modelling purposes.

Meteorological remote sensing by radar: The early development of **radar**s (**ra**dio **d**etection **a**nd **r**anging) and their application in meteorology is described in Rinehart (1999). Two milestones in radar evolution were, firstly, the introduction of Doppler radars which measure velocities

with help of the Doppler effect and, secondly, the polarimetric radars that use for transmission and/or reception two different polarizations of radiation. In such a way additional particle and precipitation properties can be deduced. Details on radar technique measurements dedicated to meteorological phenomena are presented by, e.g.: Battan (1973), Doviak and Zrnić (1993), and Bringi and Chandrasekar (2001). Properties of the mobile X-band radar used for the measurements discussed in this thesis can be found in Mosimann (1994) or Göke (1999). Note that these works reflect the radar state before the modernization. At that time, the time resolution was only 60 s (later 30 s) with a velocity resolution of 0.5 m s^{-1} and later 0.125 m s^{-1}. This has been improved to 1 s (and 0.125 m s^{-1}), which can even be further refined for short periods. Consequently, small and short lived structures in precipitation become better visible than those obtained in older otherwise similar studies as, e.g. Mosimann (1995). One of the few comparable radars is used in McGill, Montreal. This radar was used, for instance, to observe supercooled water and secondary ice generation in association with bimodality in Doppler spectra (cf. Zawadzki et al., 2001).

Vertical winds and embedded convection: There is a series of studies describing the mesoscale and microscale structure and organization of clouds and precipitation of midlatitude cyclones basing on field studies of, for instance, cold fronts (Hobbs et al., 1980), occluded frontal systems (Houze et al., 1976), or with respect to vertical air motions (Herzegh and Hobbs, 1981). The classical separation into stratiform and convective regimes of precipitation (Houze, 1997) is quite coarse. A more detailed classification is needed for the investigation of the relation between embedded convection and riming and for explaining differences in the degree of riming. There are various partly contradictory definitions of convection, but in meteorology they have in common that they refer to vertical transport or air motion, resp.[1] A classification of convection has been made by, e.g. Mosimann (1995), for vertical X-band radars via the variability of the mean Doppler velocity by means of a convection index. Depending on the used definition, areas with updrafts are not identical with embedded convection. In this study different definitions are discussed, and mainly vertical winds are considered. Also earlier studies use methods to deduce vertical wind velocities from Doppler velocity measured by vertically pointing radars: For rain, there are studies by, e.g., Barthazy and Joss (2000), (Göke, 1999) or Klaassen (1983). For snow, Battan and Theiss (1966) subtracted also from the radar Doppler velocity the particle fall velocities, but used for the latter only one fixed estimated value. Herzegh and Hobbs (1981) deduced ice particle velocity from reflectivity measurements with an empirical relation by Atlas et al. (1973).

Influences of wind on riming: Houze and Medina (2003) investigated orographic enhancement of precipitation and observed without further quantification, that "cellular overturning" (Smith, 1979) in stratiform precipitation could be a possible reason for riming. Orographic effects on the

---

[1]cf. Section 4.3 for more details

formation of snowfall were studied in Japan by Harimaya and Nakai (1999). They found increased riming with an increase in *horizontal* wind speed, and postulated that these horizontal winds lead to an increase of *updrafts* and thus to the observed riming. Vohl et al. (1999) made experiments in a wind tunnel, showing that there is a tendency to faster drop growth via turbulence. They explain this effect with enhanced collision and coalescence, which are related to the riming process.

1.4 Outline

After this introduction (Chap. 1), the following Chapter 2 will start with a basic introduction to the theory of the processes that play a role for the microphysics of snow (Sec. 2.1) and especially for riming. Here more examples for relevant literature are given. In Section 2.2, applications and theory of radars in meteorology will be addressed and Section 2.3 deals with some aspects of cloud dynamics.

Following a presentation of the applied instrumentation (Chap. 3), in Chapter 4 the methods are explained that have been developed for this thesis: the ameliorated correction of time lags (Sec. 4.1), and the estimation of vertical wind velocity (Sec. 4.2). Additionally Section 4.3 discusses different definitions related to convection and makes new proposals.

In Chapter 5 data and results of the field campaign RAMS are presented. They are together with general considerations discussed in parallel in the same chapter. Finally, Chapter 6 will conclude the results, and in Chapter 7 an outlook will be given.

Chapter 2

Theoretical background

2.1 Microphysics of precipitation

In this chapter basics of nucleation and growth as well as of characteristics of various hydrometeor types are presented. A special focus lays on the microphysics of riming.

2.1.1 Nucleation, growth, and properties of water droplets

Homogeneous nucleation

The term nucleation denominates the generation process of a droplet (or ice particle). Droplets can form by homogeneous nucleation out of pure water vapor. Here, water vapor molecules collide with each other, stick together, and start to form a droplet. Such a very small droplet, also called embryo, can persist if the free energy released by the molecules that pass over from gaseous to liquid phase, is sufficient to form the curved water-air interface; i.e. the energy for the surface tension $\sigma_{vl}(T)$ has to be provided. If these two energies are balanced, a critical minimum radius R_c is given by Kelvin's formula

$$R_c = \frac{2\,\sigma_{vl}(T)}{n_l\,k_B T \ln\left(e/e_s(T)\right)} \tag{2.1}$$

as function of the temperature T and of the ambient vapor pressure e. k_B is Boltzmann's constant, and n_l the number of water molecules in liquid phase per unit volume. A droplet has to reach R_c in order not to re-evaporate. In this formula, the amount of water vapor in the surrounding air is described in terms of the ratio of the ambient partial pressure of water vapor e to the saturation water vapor pressure $e_s(T)$ at a given temperature T [K]: $e/e_s(T)$. This is closely related to

7

relative humidity $rH = 100 \cdot e/e_s(T)\,[\%]$. Theoretical considerations show that under typical tropospheric conditions relative humidities of $400 - 500\%$ would be necessary for homogenous nucleation of pure water (Houze, 1993). In this form, this process plays practically no role in natural clouds, because supersaturation

$$S = 100 \cdot \left(\frac{e}{e_s} - 1 \right) \quad [\%] \tag{2.2}$$

is in the atmosphere rarely higher than 1% (Houze, 1993). But the physics described in this section is also relevant for the heterogeneous nucleation of drops and ice particles that we will discuss now:

Heterogeneous nucleation

In the earth atmosphere droplet nucleation occurs in the presence of suspended solid particles, the aerosol particles; this kind of nucleation is named heterogeneous nucleation. Aerosol particles that can contribute even at low supersaturation to the initiation of droplet growth are called cloud condensation nuclei (CCN). Two mechanisms are involved: Firstly, if water molecules diffuse onto a wettable surface of an water-insoluble aerosol-particle, a spherical water cap can be built more easily and with less water molecules contributing than in the homogeneous case. Secondly, a water-soluble CCN can absorb water vapor molecules in a moist or supersaturated environment by passing through quasi-equilibrium states described by the famous Köhler equation (Pruppacher and Klett, 1997). If the critical radius is reached, the CCN is called activated and a droplet continues to grow if sufficient supersaturation remains, and a macroscopic cloud drop is formed. Such a drop can grow further by condensation, i.e. by absorbing water vapor molecules transported by diffusion to the drop. To reach a net growth, the ambient water vapor pressure has to be larger than that at the drop's surface. For droplets with radii larger than about 20-30 μm, a second growth process becomes possible, namely, coagulation. Hereby, two colliding drops form a single larger one. In this way, rain drops are created. Drops might shrink by evaporation or split by break-up of larger drops. All these processes are also relevant for rain drops formed by melted ice particles.

Some properties of droplets

Growing rain drops are accelerated by gravitation, but are also retarded by frictional forces proportional to the fall velocity. In equilibrium, for a given air density ρ_a a constant terminal fall

velocity

$$v_T = \sqrt{\frac{2mg}{\rho_a A_{\text{eff}} C_D}}$$

(2.3)

is reached, where m is the mass of the drop, g the gravitational acceleration, A_{eff} an effective surface (exposed to the flow) and C_D the drag coefficient. Only drops with radii larger than $0.1\,\text{mm}$ have a significant fall speed v_T. Therefore, this size is considered to be the threshold between cloud droplets and precipitation drops (Houze, 1993).

The most common way to describe drop size distributions in rain is in form of an exponential law first presented by Marshall and Palmer (1948). Here, the number $n(D)dD$ (with $n(D)$ in m^{-3} mm^{-1}) of particles with diameters between D and $D + dD$ [mm] is given by

$$n(D) = n_0 \, e^{-\Lambda D} \quad ,$$

(2.4)

where the parameters are $\Lambda = 4.1 R^{-0.21}$ and $n_0 = 8 \cdot 10^3$ m^{-3} mm^{-1}. R denotes the rainfall rate in mm h^{-1}. Waldvogel (1974) showed that n_0 is dependent on the microphysical processes that lead to rain formation and is thus variable.

An important parameter is the rainfall rate R that can be calculated from a distribution of drop sizes (DSD) and corresponding velocities v_T [m s^{-1}]. By assuming spherical drops it yields

$$R\,[\text{mm}\,\text{h}^{-1}] = 6\pi \cdot 10^{-4} \int_0^\infty D^3 n(D) v_T(D) \, dD$$

(2.5)

with D given in mm. For measured $n(D)$ the integral is replaced by a sum accordingly.

2.1.2 Ice nucleation and supercooled droplets

Homogeneous nucleation

Ice particles can either be homogeneously nucleated from pure water vapor or from the liquid phase. For homogeneous nucleation of an ice particle within a supercooled droplet, there is – in analogy to Kelvin's formula (Eq. 2.1) – the critical radius

$$R_{ci} = \frac{2\beta_i \sigma_{il}(T)}{\alpha_i n_i k_B T \ln(e_s(T)/e_{s,i}(T))} \,,$$

(2.6)

where α_i and β_i are shape parameters for the nucleated ice particle. $\sigma_{il}(T)$ is the surface tension of an ice-liquid interface and is defined as the increase of the free energy F with increasing surface Ω of the droplet ($\sigma = \delta F/\delta \Omega$). Further, n_i is the number of water molecules in solid phase per unit volume (Houze, 1993). $e_{s,i}(T)$ is the water vapor pressure at saturation with respect to a flat *ice* surface. For $T < 0\,^\circ\text{C}$ it is lower[1] than with respect to a flat *water* surface $e_s(T)$ (Pruppacher and Klett, 1997).

Supercooled cloud droplets are, under atmospheric conditions, found in a temperature range from -0 to -40 $^\circ$C. Below this threshold droplets freeze spontaneously, whereas homogeneous nucleation of ice particles directly from vapor does not occur in the atmosphere (Houze, 1993).

Heterogeneous nucleation

Heterogenous nucleation is for temperatures down to -40 $^\circ$C the most important process for the nucleation of ice particles (Houze, 1993), but the percentage of aerosols which are capable to act as ice nuclei is small compared to the percentage of nuclei for drop formation (cf. Sec. 2.1.1). The most common concepts of processes that could lead to heterogeneous nucleation are:

Deposition: Ice crystals can form by deposition of vapor molecules on an aerosol particle that has, for example, a similar grid structure as ice has.
Immersion freezing: A potential ice nucleus is already included in a droplet which is cooled down and can be "activated", i.e. as soon as it becomes cold enough, it causes freezing.
Condensation freezing: This is a special case of the immersion freezing, in a sense that the aerosol particle included in the droplet also caused the condensation of this droplet.
Contact freezing: In this case, a droplet starts to freeze after collision with a suitable aerosol.

Generally, the lower the temperature, the higher is the chance for a given aerosol particle to act as an ice nucleus. An empirical formula for the number N_n of ice nuclei per liter of air is given by (approx. equivalent to Fletcher (1962))

$$\ln N_\text{n} = a_i (253 - T) \quad . \tag{2.7}$$

Here, T is the temperature [K] and a_i is a location dependent parameter that ranges between 0.3 and 0.8. After Equation 2.7, there is at 253 K ($-20.15\,^\circ$C) only one aerosol per liter of air that can be an ice nucleus. This formula also shows that, with $a_i = 0.6$, N_n increases tenfold if the temperature decreases by 4 $^\circ$C (Houze, 1993). For drops that are transported to regions with colder temperatures, freezing may begin at temperatures anywhere between -4 and -40 $^\circ$C,

---

[1]This has important effects on depositional growth of ice particles, as e. g. on the Bergeron-Findeisen-process.

depending on the present CCN (Emanuel, 1994).

2.1.3 Growth processes of ice particles

Once an ice particle is formed, it can continue to grow by deposition, by aggregation or by riming, which is the freezing of supercooled droplets on the surface of an existing ice particle. The particle can also shrink by sublimation, break-up or melting.

Deposition, aggregation and crystal shapes

If water vapor molecules are transported by diffusion to and deposited onto an ice particle, this particle grows in mass and size, and a regularly formed crystal can develop. Figure 2.1 gives an overview over resulting crystal shapes, also called habits, depending on temperature and level of supersaturation. As a rule of thumb, at a given temperature a higher supersaturation results in a higher surface-to-volume ratio of a crystal (Houze, 1993).
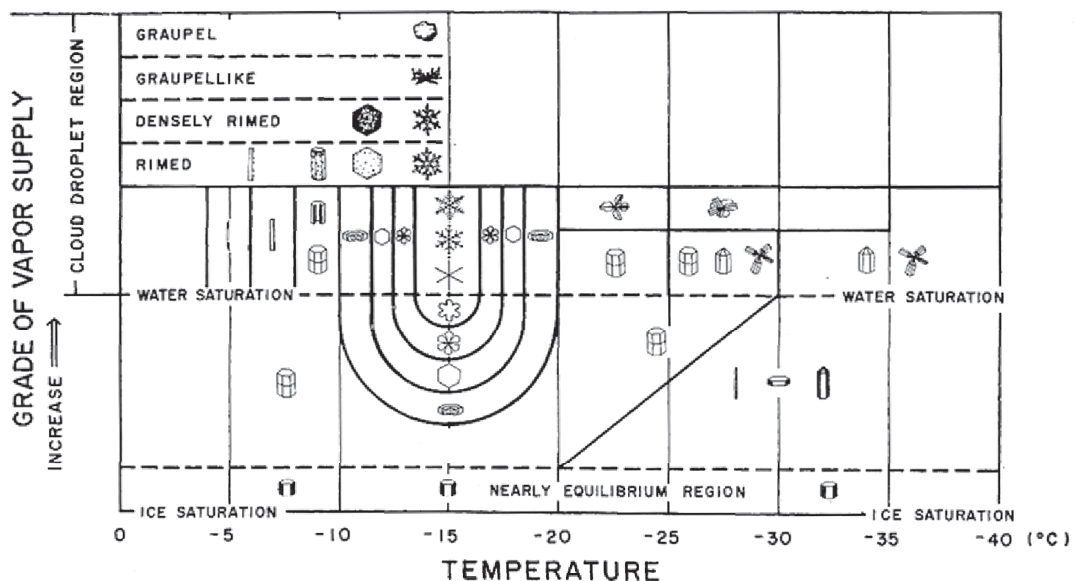
Figure 2.1: *Ice crystal habits in dependence of temperature and supersaturation. From: Prupacher and Klett (1997, p. 44) after Magono and Lee (1966).*

The process in which two ice particles collide and result in one large particle is referred to as aggregation: These resulting aggregates are commonly called snowflakes. Aggregation does not increase the total ice mass. Its efficiency depends besides others on number concentration, temperature, and crystal habit. A maximum probability for adhesion exists for temperatures above

-5 °C, when the surface of the ice particles becomes sticky. For temperature ranges, where dendritic crystal growth predominates, a secondary maximum of aggregation probability exists: the arms of the dendrites can get mechanically stuck with each other (Houze, 1993).

There are several classification schemes for ice particles. Two examples are the very detailed scheme by Magono and Lee (1966), and a more basic one by The International Commission on Snow and Ice (Colbeck et al., 1990). From the latter one, the classification of ice precipitation particles is shown in Table 2.1.

Table 2.1: *Subclasses of ice precipitation particles after the classification scheme by The International Commission on Snow and Ice (Colbeck et al., 1990).*

Nr.	Subclass	Symbol	Shape	Physical process
1 a	Columns	cl	Short prismatic crystal, solid or hollow	Growth at high supersaturation: -3 to -8 and below -22 °C
1 b	Needles	nd	Needle-like, approx. cylindrical	Growth at high supersaturation: -3 to -5 °C
1 c	Plates	pl	Plate-like, mostly hexagonal	Growth at high supersaturation: 0 to -3 and -8 to -25 °C
1 d	Stellar dendrites	sd	Six-fold, star-like, planar or spacial	Growth at high supersaturation: -12 to -16 °C
1 e	Irregular crystals	ir	Clusters of very small crystals	Polycrystals growing at varying environmental conditions
1 f	Graupel	gp	Heavily rimed particles	Heavy riming of particles by accretion of supercooled water
1 g	Hail	hl	Laminar internal structure, translucent or milky, glazed surface	Growth by accretion of supercooled water
1 h	Ice pellets	ip	Transparent, mostly small spheroids	Frozen rain

2.1.4 Riming

"Riming" denotes the process when an ice particle comes in contact with a supercooled cloud droplet that subsequently freezes on the surface. This is also referred to as accretion. Rime can be found on all ice crystal habits. The amount of frozen drops on the ice particle surface can range from single drops to several layers. If there are several layers, the habit of the ice crystal

that originally grew by deposition might no longer be discernible. These particles are named graupel.

Most classical schemes (see Sec. 2.1.3), as e.g. Magono and Lee (1966) or Colbeck et al. (1990), only provide a coarse definition of the classification for the amount of riming. But there are several more precise scales. A basis for the determination can be an optical analysis of ice particle samples, e.g. attained by the Formvar replication method (Schaefer, 1956, cf. Sec. 3.7). Rango et al. (2003) provide very detailed images of single rimed particles with the help of low temperature scanning electron microscopy. In this thesis, the six-step scale by Mosimann et al. (1994) has been used; in their paper they also give a comparison of their scale to other existing riming scales. The different forms of optical appearance of different amounts of supercooled cloud droplets on an ice crystal are described, classified, and numbered with increasing number of cloud droplets. Table 2.2 shows the detailed classification criteria for the degree of riming (RIM) and Figure 2.2 gives examples in form of photographs of ice particles on Formvar slides.

Table 2.2: *Original classification of the degree of riming by optical appearance (Mosimann et al., 1994).*

RIM	Name	Description
0	Unrimed	No accreted cloud droplets on the crystal surface
1	Lightly rimed	Few cloud droplets on the crystal surface. Droplets usually scattered instead of clumping together. Rimed covered crystal's surface < 25%.
2	Moderately rimed	Planar crystals: edges and branches undoubtedly droplet covered; inner part only lightly rimed or even unrimed. Rime coverage visually seems insignificant, but small droplets ($D \sim 10~\mu$m) at edges can significantly contribute to accreted mass. Columnar crystals: rime coverage approx. 50%.
3	Densely rimed	Whole crystal surface nearly completely covered with one layer of droplets. Crystal shape still identifiable at first glance; shape not deformed by cloud droplets. Planar crystals: more than one layer of accreted cloud droplets only found at edges.
4	Heavily rimed	Large amount of accreted cloud droplets; original shape barely recognizable. Thickness clearly increased and surface no longer visible: multiple layers of droplets.
5	Graupel	All kinds of graupel: lump, conical, and mature hexagonal graupel.

This riming scale is non-linear with respect to increase in mass. There is, for instance, less mass
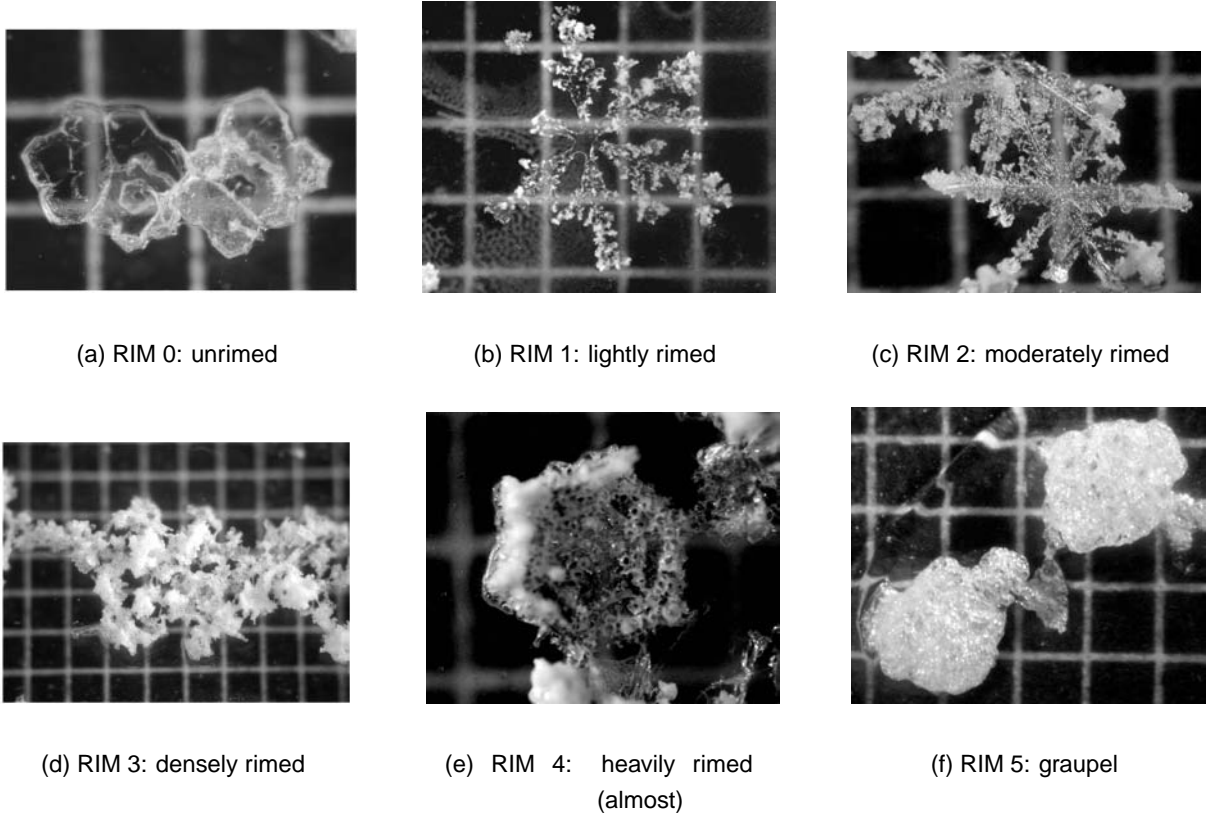
(a) RIM 0: unrimed

(b) RIM 1: lightly rimed

(c) RIM 2: moderately rimed

(d) RIM 3: densely rimed

(e) RIM 4: heavily rimed (almost)

(f) RIM 5: graupel

Figure 2.2: *Photos of Formvar replicas of ice crystals with varying degree of riming* RIM*. The grid size is 1* mm*.*

of accreted droplets added, if a particle goes from RIM values of 0 to 1 than from 4 to 5. The fraction of rime mass

$$f_r = \frac{m_r}{M} = \frac{m_r}{m_u + m_r} \tag{2.8}$$

is defined as the ratio of mass of accreted rime m_r to the total mass of the rimed particle M; m_u is the unrimed portion grown by deposition. f_r is a linear and theoretically more objective quantification, but is in practice difficult to measure. Mosimann et al. (1994) give an empirical relation between their degree of riming scale RIM and the rimed mass fraction in the general form

$$f_r(\mathrm{RIM}) = \frac{b(a^{\mathrm{RIM}} - 1)}{1 + b(a^{\mathrm{RIM}} - 1)} \quad , \tag{2.9}$$

where a and b are empirical fit parameters. They specify values of $a = 3.1$, $b = 0.020$ for planar

crystals, and of $a = 3.6$, $b = 0.012$ for columnar crystals, and $a = 3.6$, $b = 0.017$ as an approximation for all crystal types. But these values have to be taken with care, because they are based on other empirical results as, for instance, mass-size relations, and are based only on a limited number of measured ice crystals.

Influences on riming

Collection growth is the process, when one relatively large particle grows by collecting smaller particles. For spherical particles, the increase in mass m_l with time t can be described by (Pruppacher and Klett, 1997, p. 617)

$$\frac{dm_l}{dt} = \frac{4\pi\rho_w}{3} \int E_c \cdot \pi(a_l + a_s)^2 \cdot (v_{T,l} - v_{T,s}) \cdot a_s^3 \, n(a_s) \, da_s \quad , \tag{2.10}$$

where a_l and a_s are the radii of the large and the small particles; $v_{T,l}$ and $v_{T,s}$ are the corresponding fall velocities. ρ_w is the density of water and $n(a_s)da_s$ the number of small particles with radii between a_s and $a_s + da_s$. The collision efficiency E_c is the ratio between actual collision cross section and geometric cross section (Pruppacher and Klett, 1997, p. 569). It depends on the actual flow field around the particles (Tables can be found in Pinsky and Khain (1998)). In approximation, the large particle can be seen as an ice particle collecting supercooled cloud droplets. This equation shows the importance of the cloud drop size distribution on riming. The relative velocity $v_{T,l} - v_{T,s}$ of two particles can be influenced by wind, at least until a new equilibrium is reached. Updrafts will mainly prolong the time the particle has for growing until it falls out of the respective growing region. Also size and habit of the ice particles influence riming (e.g., Tab. 2.2).

The literature values for sizes of cloud droplets which can accrete on ice particles, span a wide range. While, for instance, Black and Hallett (1998) name diameters of only $10 - 20$ μm, and Pruppacher and Klett (1997) give a range of $10 - 80$ μm. Rango et al. (2003) report diameters as large as up to 100 μm for accreted elongated drops. They performed investigations with the help of low temperature scanning electron microscopy and found also that if a single snow crystal is rimed, the cloud droplets are often only found on one side of the crystal. Rime, however, is more randomly spread on aggregates. In the early stages of riming the accreted drops freeze in the form of flattened hemispheres. In later stages, the frozen drops become more elongated. For that, a possible explanation might be that at the beginning the surface of the ice particle that faces the fall direction comes into contact with the droplets. If riming proceeds, the aerodynamical properties of the ice particles change and they may turn upside down. Now the flow field around the rimed particle may transport cloud droplets to the trailing face of the crystal, where they freeze. Pruppacher and Klett (1997, p. 660) give a criterion that determines the shape of the

accreted drop: It depends on the kinetic energy of the impact, the surface tension of the drop that promotes spherical shapes, and how fast a drop freezes. Lew et al. (1986) deduced from wind tunnel experiments that porous surfaces rime better than nonporous ones.

Of course, an ice particle can simultaneously grow by riming and by deposition. But, for air that is saturated with respect to water the supersaturation can be up to 21% with respect to ice (Emanuel, 1994). Thus, under such conditions ice crystals can grow via deposition at the cost of supercooled cloud droplets, and thus by a process competing with riming. This is the Bergeron-Findeisen-process. For riming, there are two different growth modes: the dry and the wet growth regime (Ludlam, 1958). For dry growth, the temperature stays below 0 °C, despite the released latent heat of the freezing droplets. But during wet growth the released latent heat warms up parts of the conglomerate to temperatures of more than 0 °C. If ice particles grow by riming to sizes larger than 5 mm, they are referred to as hailstones (Pruppacher and Klett, 1997, p. 41). In hailstones the temperature may be several degrees warmer than the environment. Spongy ice (List, 1965) incorporates both air bubbles and liquid water. An overview over studies of the density of accreted rime as function of, for example, the impact velocity can be found in Pruppacher and Klett (1997, p. 661 and p. 65): the bulk density of graupel particles varies between 50 and 890 kg m^{-3}.

Ice multiplication

Often, far more small ice particles are measured in natural clouds than expected from experiments in air expansion chambers with activated ice nuclei (cf. Eq. 2.7). Houze (1993, p. 89) explains that the regions where this ice enhancement is found are rather in older than in younger parts of clouds. They occur along with supercooled cloud droplets, especially if the largest of those exceed diameters larger than 20 μm. Ice nuclei concentrations can rise rapidly. For example, Houze (1993) reports increases from 1 to 1000 small ice particles per liter in less than 10 min. He also mentions several hypotheses to explain this effect: The nucleation efficiency might be increased with higher supersaturation. Furthermore, ice splinter might have been produced, either through fragmentation of existing ice particles by the Hallett-Mossop effect. This process is also called ice multiplication. Hallett and Mossop (1974) performed laboratory experiments, in which small ice splinters were produced, when supercooled droplets with a diameter $> 23\,\mu$m collided with an ice surface at speeds ≥ 1.4 m s^{-1} and temperatures between -3 and -9 °C. Saunders and Hosseini (2001) extended these experiments to higher collision velocities and observed that for the velocity range 1.5 to 12 m s^{-1} the maximum of secondary ice production is at 6 m s^{-1}.

By ice multiplication, a large number of small ice particles can be produced. For a production of an equivalent amount by heterogeneous nucleation, a large number of aerosols than can serve as ice nuclei would be necessary, but these are relatively rare. If there is enough water vapor

available, the ice particles continue to grow. Then, the gain of precipitation is amplified by ice multiplication. Similar results are received by the seeder-feeder effect. Here, the production of a precipitation in low level cloud is enhanced through ice particles falling into it from a higher level cloud.

Influence of riming on the ion concentration of rain water

Riming plays an important role for the transport of aerosol particles from the atmosphere to the ground. This transport is also called precipitation scavenging. Collett and Steiner (1992) stated that for graupel a ratio of one is reached between the ion concentration in cloud water and in precipitation. Whereas, if a particle grows via the Bergeron-Findeisen process, much less aerosol particles resp. pollutants are transferred from the supercooled droplet to the ice particle (Scott, 1978). Under conditions of higher precipitation intensities, riming appears to be the dominant transfer mechanism for the incorporation of the major ionic species into snow (Dixon et al., 1995; Poulida et al., 1998).

2.1.5 Fall speed and mass of ice particles

A general equation for the terminal fall speed of solid hydrometeors can be found in Böhm (1989). Experimental results can, for example, be found in studies published by Locatelli and Hobbs (1974) as well as by Zikmunda and Vali (1972) or Schefold (2004).

Table 2.3 gives an overview over fall velocities v_T and masses m of selected ice particle types. Mass is given in form of mass-diameter relations of the type

$$m = a_m \cdot D^{b_m} \quad , \tag{2.11}$$

with particle specific empirical parameters a_m and b_m, and D as diameter resp. characteristic length of the particle. Generally one can say the more rimed a particle the larger is the increase in fall speed with size (Houze, 1993, p. 90).

The complete version of Table 2.3 can be found in Locatelli and Hobbs (1974). There, it is deduced that: for graupel, $v_T \propto D^{0.6}$ and $m \propto D^3$; for densely rimed columns, dendrites, or radiating assemblages of dendrites, $v_T \propto D^{0.2}$ and $m \propto D^2$; for densely rimed aggregates, $v_T \propto D^{0.3}$ and $m \propto D^2$; and for unrimed aggregates $v_T \propto D^{0.2}$ and $m \propto D^2$ (units as in Tab. 2.3). However, it should be noted that the description of riming is similar but not identical to Mosimann et al. (1994). For all ice particles, properties as mass and fall velocity do not follow a close relationship

but show a large scatter. This can, e.g., be seen in the experimental results based on a large number of natural ice particles by Schefold (2004).

Table 2.3: *Fall speed and masses for selected types of ice particles. The first four rows are based on data by Locatelli and Hobbs (1974), the last two are two extreme values by Heymsfield and Kajikawa (1987). Diameters of aggregates are determined by reassembling their arms into an area equivalent circle. The maximum dimensions D are given in mm, and the masses in mg; the units of the fall speed v_T are m s^{-1}. Thus, b_m is dimensionless, and a_m is given in mg mm$^{-b_m}$.*

Particle type	Velocity-size relationship	Mass-size relationship	Range of maximal dimensions [mm]
Lump graupel $0.1 < \rho < 0.2$ mg m^{-3}	$v_T = 1.3D^{0.66}$	$m = 0.078D^{2.8}$	0.5 to 3.0
Graupel-like snow of lump type; intermediate density	$v_T = 1.1D^{0.28}$	$m = 0.059D^{2.1}$	0.5 to 2.2
Densely rimed dendrites	$v_T = 0.62D^{0.33}$	$m = 0.015D^{2.3}$	1.8 to 4.0
Aggregates of unrimed radiating assemblages of dendrites, or dendrites	$v_T = 0.8D^{0.16}$	$m = 0.073D^{1.4}$	2.0 to 10.0
Stellar with rimed spatial branches	$v_T = 0.43D^{0.24}$	$m = 0.013D^{1.74}$	3.0 to 6.2
Hexagonal plate	$v_T = 0.41D^{0.86}$	$m = 0.018D^{3.31}$	0.3 to 1.5

2.2   Radar as a tool for the investigation of precipitation

A **radar** (**Ra**dio **d**etecting **a**nd **r**anging) sends out electromagnetic radiation that is focussed by an antenna to a narrow beam. A part of this radiation is scattered back to the source by either precipitation targets or by targets that are unwanted for weather applications as for example mountains. The latter produce the so called clutter. All radiation that is reflected back to the antenna is collected, amplified, and analyzed. This way of "remote-sensing" has advantages compared to in situ-measurements (as, e.g., by rain gauges): precipitation can be qualitatively detected over a large area in a short time. But as will be discussed in this chapter, the quantitative and sometimes also the qualitative translation of radar data into descriptions of precipitation that are meteorologically useful holds problematic issues.

2.2.1   Radar equation for Rayleigh scatterers

Single scatterers

The electromagnetic radiation transmitted by a radar is focussed by an antenna to a beam. The directional gain of an antenna

$$g(\theta, \varphi) = \frac{S_t(r, \theta, \varphi)}{P_t/(4\pi r^2)}$$ (2.12)

is a measure for the capacity of an antenna to concentrate the transmitted energy in a given direction (θ, φ) at a distance r. $g(\theta, \varphi)$ is the ratio of the electromagnetic power flux $S_t(r, \theta, \varphi)$ to the flux that would result if the total transmitted power P_t was isotropically distributed. The directional gain does not depend on r. If θ and φ point in the direction of the beam axis, we write $g_{\max}$, because this is the direction of the maximal gain.

For most radars, only one antenna is used for transmitting as well as for receiving. The power density S_r which is radiated back to this antenna depends on the scatterers in the beam. For a single scatterer the back scattering cross section

$$\sigma_b = \frac{4\pi r^2 \cdot S_r}{S_t} \quad .$$ (2.13)

is an apparent area and a measure of the scatterer's back scattering ability. The scatterer "converts" the incoming power flux S_t at its position into a total isotropically re-radiated power $4\pi r^2 \cdot S_r$ that leads to a power flux S_r at the (detecting) antenna.

The ratio of the power P_r technically received by the radar to the power flux S_r at the antenna position caused by the scattered radiation is the effective antenna area $A_e = P_r/S_r$; it quantifies

the receiving efficiency of this antenna. Theoretical considerations connect the effective antenna area to the antenna gain by

$$g_{\max} = \frac{4\pi \cdot A_e}{\lambda^2} = \frac{4\pi \cdot P_r}{\lambda^2 \cdot S_r} \quad , \tag{2.14}$$

where λ is the wavelength of the emitted radiation (Rinehart, 1999).

A combination of Equations 2.12, 2.13, and 2.14 yields the radar equation for a single scatterer

$$P_r = \frac{P_t \, g_{\max}^2 \, \lambda^2 \, \sigma_b}{64 \, \pi^3 \, r^4} \quad . \tag{2.15}$$

This equation relates the power received by the radar to the radiation scattered by a single scatterer with cross section σ_b (and vice versa). Here, effects as for example attenuation and losses in the wave guides to the receiver are neglected.

Multiple scatterers

Some changes have to be made in the radar equation for the observation of a real precipitation system which has multiple scatterers in the volume $V_{\mathrm{res}}(r)$ simultaneously illuminated by the radar. This resolution volume

$$V_{\mathrm{res}}(r) = \pi \Theta^2 \left(\frac{r}{2}\right)^2 \frac{c\tau_p}{2} \tag{2.16}$$

depends on the geometry of the beam and for a pulsed radar on the pulse duration τ_p. Here, a gaussian beam profile with a circular cross section is assumed and side lobes are neglected. The opening angle Θ [rad] or 3 dB beamwidth is defined as the angle that spans the range where the microwave radiation is at least one-half of its peak intensity or where the power deviates by less than 3 dB from its peak value (Doviak and Zrnić, 1993), respectively. Figure 2.3 shows a simplified beam geometry and explains the abbreviations.

Assuming the scatterers are uniformly distributed in the radar volume, isotropically scattering, and not interacting with each other, the radar reflectivity per unit volume of air

$$\eta = \sum_{V_{\mathrm{res}}} \frac{\sigma_b}{V_{\mathrm{res}}} \tag{2.17}$$

is the sum of the back scattering cross sections of the individual scatterers σ_b in the resolution volume V_{res}. To arrive at a radar equation valid for multiple scatterers, it has to be noted that
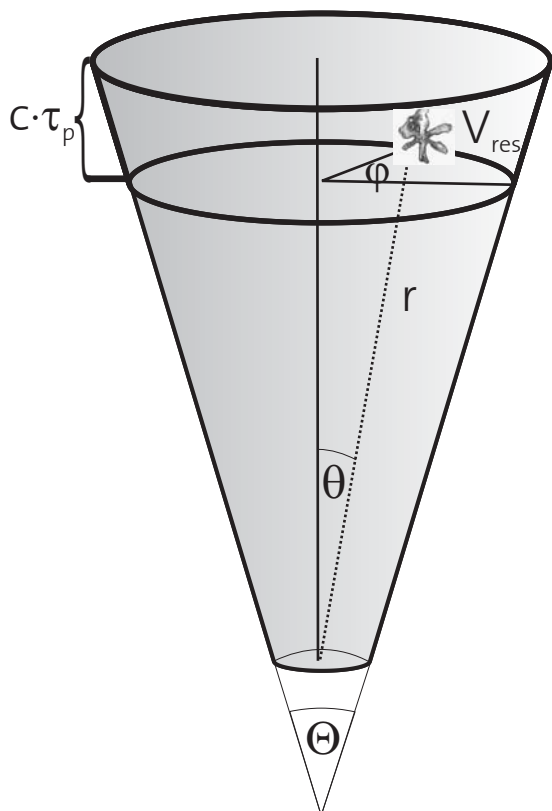
Figure 2.3: *Simplified geometry of a radar beam with circular cross section. The angles θ, φ and the distance r describe a position in the beam in spherical coordinates. Θ is the beamwidth. In radial direction is the third dimension of the resolution volume V_res given by the pulse duration τ_p times the speed of light c.*

Equation 2.14 is valid only for the maximal directional gain g_max in the direction of the beam symmetry axis. Accounting for a Gaussian beam profile the corrected gain

$$g_c = g_\mathrm{max} \sqrt{\frac{1}{2 \cdot \ln 2}} \tag{2.18}$$

describes the capacity of the antenna to concentrate energy within the beamwidth limits (Rinehart, 1999). To go from a single scatterer (Eq. 2.15) to multiple scatterers the corrected gain g_c (Eq. 2.18) is used instead of g_max and the radar reflectivity per unit volume of air η (Eq. 2.17) is taken for the back scattering cross section σ_b. In addition, the received power is averaged over a series of pulses in order to account for quickly fluctuating relative positions of scatterers in the illuminated volume. Thus, the averaged received power is given by the weather radar equation

$$\overline{P}_r = \frac{P_t\, g_\mathrm{max}^2\, \lambda^2\, \Theta^2\, \tau_p\, c\, \eta}{512(2\ln 2)\,\pi^2\, r^2} \quad . \tag{2.19}$$

The average time has to be long enough to give stable results and short enough for the measurements to be still correlated (Doviak and Zrnić, 1993, p. 84).

Rayleigh scattering

If a scattering particle is spherical and its diameter small compared to the wavelength, i.e. for drops $D \leq \lambda/16$ (Doviak and Zrnić, 1993, p. 40), Rayleigh scattering theory applies and the back scattering cross section is given by (Doviak and Zrnić, 1993)

$$\sigma_{\mathrm{b}} = \frac{\pi^5}{\lambda^4} |K|^2 D^6 \quad , \tag{2.20}$$

where K is defined as

$$K = \frac{m^2 - 1}{m^2 + 1} \quad . \tag{2.21}$$

$m = n - in\kappa$ is the complex refractive index, where n is the real part of the refractive index and κ determines the attenuation (Born and Wolf, 1964, p. 613). For water, $|K|^2 = 0.93 \pm 0.004$ for temperatures between 0 and 20 °C and wavelengths λ between 3 and 10 cm (Battan, 1973, p. 38). Thus, we will use $|K|^2 = 0.93$ for rain drops and in this case write $|K_w|^2$ for $|K|^2$.

Reflectivity factor

There is a practical need to relate the measured reflectivity per unit volume (Eq. 2.17) to meteorological meaningful units. For this purpose, the radar reflectivity factor

$$Z_w := \frac{1}{V_{\mathrm{res}}} \sum_{V_{\mathrm{res}}} D^6 = \int\limits_0^{\infty} N(D) D^6 \, dD \tag{2.22}$$

has been introduced. It is defined as the sum of the drop diameter to the power of six over the resolution volume. The sum can be substituted by an integral, if a drop size distribution $N(D)$ is given. For spherical Rayleigh scattering water drops (Eq. 2.20), the reflectivity η (Eq. 2.17) can be written as

$$\eta = \frac{\pi^5}{\lambda^4} |K_w|^2 Z_w \quad . \tag{2.23}$$

Here, $|K_w|^2$ is 0.93 (cf. Eq. 2.21). Even, if the assumptions for Rayleigh scattering water spheres does not hold as, for instance, in snow, it is common practice to simply use the same Equations 2.22 and 2.23, and to rename Z_w to the effective reflectivity factor Z_e. This is done, because normally the composition of hydrometeors in the resolution volume is unknown.

Finally, we get an equation for the reflectivity factor as a meteorologically relevant microphysical quantity and the power P_r, which is received by the radar. For this, the reflectivity η is substituted in the radar weather equation (Eq. 2.19) by the (effective) reflectivity factor using Equation 2.23. Thus, Z_e can be written as

$$Z_e \left[\frac{\text{mm}^6}{\text{m}^3} \right] := \frac{\overline{P}_r r^2}{|K_w|^2} \frac{P_t \, g_{\text{max}}^2 \, \lambda^2 \, \Theta^2 \, \tau_p \, c}{512(2\ln 2)\,\pi^2} \quad . \tag{2.24}$$

The values of Z_e can span a range of a couple of orders of magnitude, thus, it is useful to use logarithmic units. It is the preferred way to write

$$\text{dBZ}_e := 10\log \frac{Z_e}{\left[\frac{\text{mm}^6}{\text{m}^3} \right]} \quad . \tag{2.25}$$

In practice, the difference between reflectivity η (Eq. 2.17) and effective reflectivity factor Z_e (Eq. 2.24) is often neglected and both are named reflectivity. In the following chapters we thus will simply write Z for Z_e and call it reflectivity unless the difference to the real reflectivity η is important.

2.2.2 Measurements of scatterer distance and velocity for pulsed radars

So called "Doppler radars" offer the possibility to determine the radial velocity of scatterers in addition to their distance from the radar. They send out not a continuous signal, but pulsed signals with normally one distinct pulse repetition frequency (PRF). The distance

$$r = \frac{c \cdot t}{2} \tag{2.26}$$

between a scattering target and the radar can be determined via the travel time t of the signal from antenna to target and back to the antenna. Here, c is the propagation velocity of the radiation, which is the speed of light.

Ambiguities arise if there are scatterers beyond the distance that a signal can cover to reach a scatterer and to return before the next pulse is transmitted. The maximum unambiguous range is given by

$$r_{\text{max}} = \frac{c}{2 \cdot \text{PRF}} \quad . \tag{2.27}$$

The reflection of a scatterer at distance r_1 that is larger than r_{max} comes back after the next pulse is emitted and is not distinguishable from the return signal by a scatterer at distance

$r_2 = r_1 - r_{\mathrm{max}}$. Techniques exist to determine and to correct for these "second trip echoes", which play a role in data of horizontally observing radars.

Doppler velocity for single scatterers

The radial velocity of a single scatterer can be determined with the help of the Doppler effect. This effect causes only small changes to the high frequency used by radars and these are technically difficult to measure. Instead, the phase shifts between two subsequent pulses (pulse pair technique) are used to determine the radial velocity of the scatterer in direction towards or away from the radar. Technically, the oscillation on which the emitted pulse is based is "memorized" as a reference in a local oscillator and compared to the phase of the received signal.

The radiation backscattered by a target that is hit by a pulse in distance r_1 from the radar has the phase

$$\Phi_1 = \Phi_0 + 2\pi \frac{2 \cdot r_1}{\lambda} \quad , \tag{2.28}$$

where λ is the wavelength. Φ_0 includes a possible phase offset as well as a phase shift during scattering. If the target is moving, it is reached at a distance r_2 by the subsequent pulse, and the received phase is

$$\Phi_2 = \Phi_0 + 2\pi \frac{2 \cdot r_2}{\lambda} \quad . \tag{2.29}$$

For a single scatterer, the difference between the phases Φ_2 and Φ_1 divided by the time between two pulses yields the scatterer's velocity

$$v = \frac{\Delta r}{\Delta t} = \frac{r_2 - r_1}{1/\mathrm{PRF}} = \frac{(\Phi_2 - \Phi_1) \cdot \lambda \cdot \mathrm{PRF}}{4\pi} = \frac{\Delta\Phi \cdot \lambda \cdot \mathrm{PRF}}{4\pi} \quad . \tag{2.30}$$

Multiple scatterers: Doppler spectra and their moments

For the case of multiple scatterers, the phase shift in the return signal is a composite of the contributions of all present scatterers. A Fast Fourier Transform is performed (FFT) over a series of pulses in order to split the phase shift into contributions from particles combined into velocity bins. For this, the returns of a series of n_p subsequent pulses are selected at run times corresponding to the same distance from the radar (cf. Eq. 2.26). A Doppler radar usually emits pulses with one

distinct pulse repetition frequency (PRF). This PRF determines together with the wavelength and the number of selected pulses n_p the maximal possible velocity resolution

$$v_{\text{res}} = \frac{\lambda \, \text{PRF}}{2 \, n_p} \quad .$$

(2.31)

In Section 2.2.1 the time was discussed over which the returning power in the weather radar Equation (Eq. 2.19) has to be averaged. In analogy, the possible range for n_p is limited by the minimum necessary number of samples to average out the random signal fluctuations; on the other hand, the sampling time should be short compared to the time in which the composition of scatterers significantly changes. Especially scanning radars which have moving antennas need short sampling times.

From the FFT a "Doppler spectrum" (Fig. 2.4) results. The total reflectivity Z is split into the contributions to the reflectivity Z_v of those scatterers which have velocities in a bin between v and $v + dv$. Here, dv is given by v_{res} (Eq. 2.31).
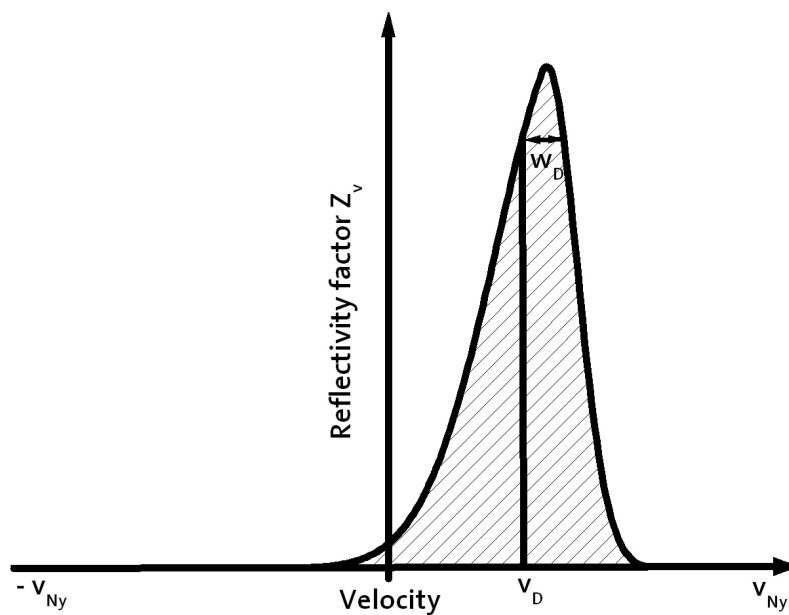

Figure 2.4: *Sketch of a Doppler spectrum and its moments. The reflectivity corresponds to the shaded area. The Doppler velocity v_D is given by the normalized first (Eq. 2.33), and the spectrum width w_D by the normalized second moment (Eq. 2.34).*

The zeroth moment of the Doppler spectrum

$$Z = \int_{-\infty}^{+\infty} Z_v \, dv$$

(2.32)

is equivalent to the total reflectivity Z. Whereas, the so called Doppler velocity v_D is defined as the first moment of the Doppler spectrum normalized by the zeroth moment

$$v_D = \frac{\int\limits_{-\infty}^{+\infty} Z_v \cdot v \cdot dv}{Z} \quad . \tag{2.33}$$

The second (normalized) moment gives us w_D, the width of the spectrum,

$$w_D^2 = <\sigma>^2 = \frac{\int\limits_{-\infty}^{+\infty} Z_v \cdot (v - v_D)^2 \cdot dv}{Z} \quad . \tag{2.34}$$

As the Doppler spectrum is not known continuously but only at discrete values (spaced by v_{res}) the integral can be substituted by a summation.

Similar to the case of second trip echoes (Eq. 2.27) ambiguities exist if there are velocities that are so high so that they result in a phase shift larger than $\pm\pi$. Using Equation 2.30, this marginal velocity which is named Nyquist velocity can be derived:

$$v_{\mathrm{Ny}} = \frac{\pi \cdot \lambda \cdot \mathrm{PRF}}{4\pi} = \frac{\lambda \cdot \mathrm{PRF}}{4} = \frac{v_{\mathrm{res}} \cdot n_p}{2} \quad . \tag{2.35}$$

The velocities $v_n = v \pm 2n \cdot v_{\mathrm{Ny}}$, with $n = 0, 1, 2...$ result in phase shifts that differ by multiples of 2π (cf. Eq. 2.30). These are not distinguishable by measurement. If particles with velocities higher than v_{Ny} are present, the spectra are "folded". For scanning radars special unfolding or "de-aliasing" techniques exist (e.g. Zawadzki, 1991; Wüest, 2001).

2.2.3 Constraints for radar measurements

There is a multitude of constraints and possible sources of error to radar measurements. Examples are effects due to side lobes, anomalous propagation, and refraction of the beam on inhomogeneities of the air, clutter, and attenuation.

The latter, attenuation, comprises the loss of radiation on the way between radar and scatterer and back. To get an idea for the order of magnitude, as an example, the one-way attenuation in dry snow at 0 $^\circ$C is given by Battan (1973, p. 74) as well as by Doviak and Zrnić (1993, p. 44)

$$K_s [\mathrm{dB\,km}^{-1}] = 3.5 \cdot 10^{-2}(R^2/\lambda^4) + 2.2 \cdot 10^{-3}(R/\lambda) \quad , \tag{2.36}$$

where R is the snow fall rate in form of melted snow [mm h^{-1}] and λ the wavelength [cm]. The first term is due to scattering, the second due to absorption. This gives, for instance, with $R = 1$ mm h^{-1} and $\lambda = 3.2$ cm an K_s of only 0.001 dB km^{-1}. Though attenuation is higher in wet snow, most of the effects mentioned in the beginning of this section are more relevant for scanning radars than for a vertically pointing radar like the one described in this thesis. A detailed discussion of the constraints can be found in the relevant literature (e.g. Battan, 1973; Bringi and Chandrasekar, 2001; Doviak and Zrnić, 1993).

2.2.4 Calculation of hydrometeor reflectivity

Rain

The determination of drop size distributions from Doppler spectra is ambiguous. On the other hand, the calculation of reflectivity from measured or theoretical particle size distributions is in theory – at least for rain – non-ambiguous. For solid hydrometeors difficulties arise because of different complex refraction indices, complicated and strongly varying shapes or densities. Rain drops are, if looked at from below – like a vertically pointing radar does – in good approximation spherical. Hence, computation of reflectivity can be done straight forward by using the reflectivity factor (Eq. 2.22). Additionally, also the rainfall rate can be obtained from drop size distributions (Eq. 2.5).

Adaption to different types of ice precipitation

For snow, the calculation of reflectivity from a particle size distribution could be done the same way as for rain (see Sec. 2.2.1 and 2.2.4), if we had dry solid ice in a spherical form with known density. The calculation had only to be adapted to the different complex refractive index and the different dielectric factor of ice $|K_i|^2$. For $\lambda = 3.2$ cm the dielectric factor of water is $|K_w|^2 = 0.93$ and for ice $|K_i|^2 = 0.176$ (Battan, 1973). The reflectivity of ice is thus approximately 5 times smaller. The effective radar reflectivity factor (Eq. 2.24) has therefore to be corrected by a factor

$$C_c = \frac{|K_i|^2}{|K_w|^2} \tag{2.37}$$

to exchange the dielectric factor for rain by the one for ice. Otherwise we would receive a reflectivity that is expressed in linear units five times too high resp. 6.9 dBZ too high in logarithmic units.

To account for densities deviating from the one of solid ice and for other crystal habits, we use the assumption of Smith (1984): For irregular shaped particles that can be considered almost spherical the backscatter cross section is equal to the one of an ice sphere with same mass (A more detailed discussion can be found in Löffler-Mang and Blahak (2001)). This assumption results in a second correction factor

$$C_{d,j} = \left(\frac{D_{eq,j}}{D_j} \right)^6 = \left(\frac{6\, m_j/(\rho_i\,\pi)}{D_j^3} \right)^2 = \left(\frac{6}{\rho_i\,\pi} \right)^2 \cdot a_m^2\, D_j^{2b_m-6} \quad , \tag{2.38}$$

which is specific for each particle j in the resolution volume V_{res}. The total number of particles is N. $D_{eq,j}$ is the equivalent diameter of a sphere with the density of ice ($\rho_i = 0.917$ mg mm^{-3}) and the mass m_j of particle j with $m_j = \frac{1}{6}\pi\rho_i D_{eq,j}^3$. The right part of Equation 2.38 is derived by a mass-size relation of the form $m_j = a_m D_j^{b_m}$ (cf. Sec. 2.1.5), where a_m has the units mg mm$^{-b_m}$.

Thus, we can re-write Equation 2.22 by using Equations 2.37 and 2.38 so that we yield the effective reflectivity factor for snow

$$Z_{e,s} = \frac{C_c}{V_{res}} \sum_j^N C_{d,j} D_j^6 = \frac{1}{V_{res}} \left(\frac{6}{\rho_i\,\pi} \frac{|K_i|}{|K_w|} \right)^2 \sum_j^N a_m^2 D_j^{2b_m} \propto \sum_j^N m_j^2 \quad . \tag{2.39}$$

As the density of snow is smaller than the density of solid ice, we will overestimate the reflectivity factor, if we use the sixth power of the diameter as in Equation 2.22. For instance with values for a_m and b_m for graupel-like snow of medium density (Sec. 2.1.5), this means a reflectivity factor proportional to the sum over the diameters to the power 4.2 instead of 6. It is remarkable that in Equation 2.39 the effective reflectivity factor is proportional to the sum of the squares of the particle masses.

Mie scattering

In the Rayleigh scattering regime that is the dipole approximation, the scattered energy is distributed nearly isotropically by particles which are small compared to the wavelength. In the Mie regime (Mie, 1908) that is the multipole approximation, larger particles scatter a larger part of the energy in the forward direction, i.e. away from the incident beam. For even larger particles, the scattering behavior comes closer to that of plane surfaces. This corresponds to geometrical optics and the back scattering cross section can be written as (Born and Wolf, 1964, p. 41)

$$\frac{4\sigma_b}{\pi D^2} = \frac{|m-1|^2}{|m+1|^2} \quad , \tag{2.40}$$

where m is again the complex index of refraction. The formulae for the Mie back scattering cross sections are even for spherical particles complicated. They are combinations of spherical Bessel and Hankel functions with the argument m (Battan, 1973). In Figure 2.5 the normalized Mie back scattering cross section $(4\sigma_b/(\pi D^2)$ is plotted as function of diameter. Solutions are given for a wavelength of 3.2 cm and for water as well as for ice spheres with varying thicknesses of the surrounding water shells. The figure shows that for a precise Mie calculation detailed knowledge of the scatterer shapes and composition would be required.
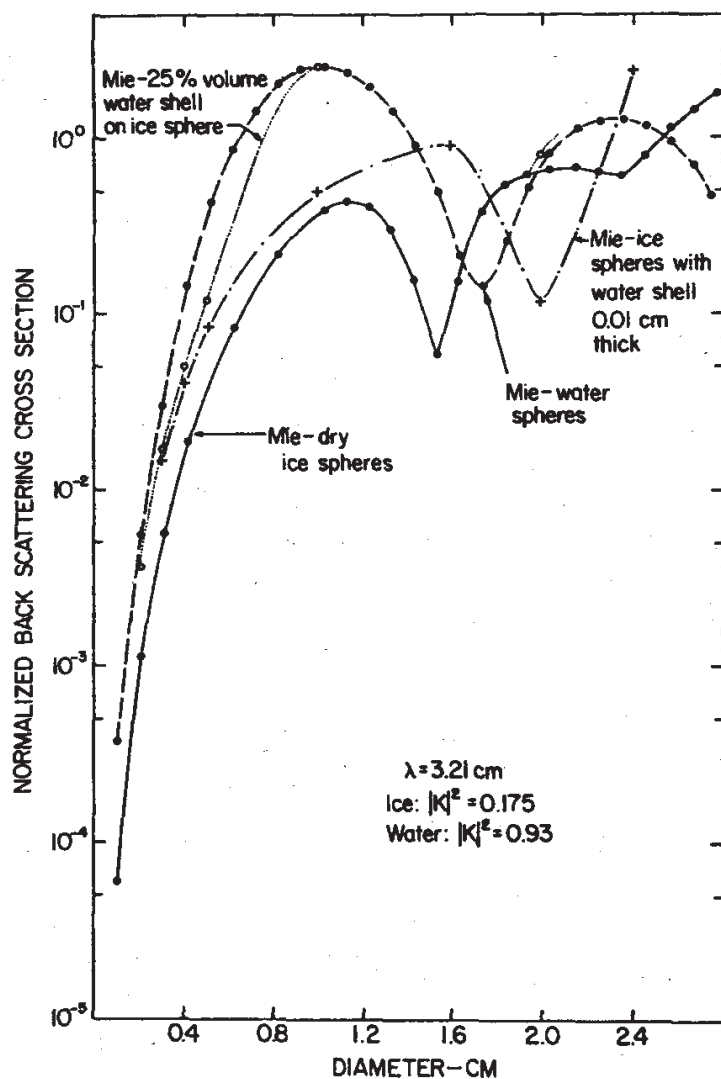
Figure 2.5: *For Mie scattering, the normalized back scattering cross section is shown as function of the particle diameter. λ is 3.2 cm. The solutions are given for water and ice spheres with varying thicknesses of surrounding water shells. From: Battan and Theiss (1968) in Battan (1973, p. 143).*

2.3   Aspects of cloud dynamics

2.3.1   Classical definition of stratiform and convective precipitation

Classically[2], precipitation processes are split into two distinct types. This is primarily a classification based on updraft velocities. If the updraft velocity w (upward positive sign) is small compared to the terminal fall velocity v_T (downward positive sign) of the present ice and snow,

$$w < v_T \quad , \tag{2.41}$$

the precipitation process is named stratiform (Houze (1993, p. 199), Houghton (1968)). Otherwise, we talk about convective precipitation. The microphysical processes as well as the appearance in radar images vary between stratiform and convective precipitation. Convective precipitation appears in cells, which are "horizontally localized patches or cores of intense radar reflectivity. In a vertical cross section, a cell is a tall, thin column of high reflectivity" (Houze, 1997). This definition goes back to Byers and Braham (1949). Small weakly convective areas enclosed in stratiform precipitation are called embedded convective cells. The type of clouds associated with strong convection are cumulus and cumulonimbus clouds; whereas stratiform precipitation falls from nimbostratus clouds (Houze, 1993). In the upper levels of nimbostratus, ice particles fall ($w < v_T$), but a weak updraft of the order of a few tens of centimeters per second is required to maintain high supersaturation and to allow for a continuing growth of particles by vapor deposition and thus to keep the precipitation process alive (Houze, 1993, p. 198).

2.3.2   The bright band

Stratiform precipitation forms – from a radar point of view – horizontally layered structures, which are mostly recognizable by a bright band, i.e. the melting layer, where reflectivity is very high. Figure 2.6 shows such a for stratiform precipitation typical vertical reflectivity and velocity profile. At the top, ice particles are small and result in small reflectivity. The particles fall and grow (Sec. 2.1.3). Shortly above the melting layer where temperatures are close to 0 °C the ice particles are often aggregate and large compared to rain drops, but they have a smaller reflectivity due to their lower dielectric factor. In this temperature range, the probability for aggregation is enhanced. When the particles start to melt, they become wet on the outside and appear to the radar more like water spheres. This results, together with aggregation, in the zone of high reflectivity that builds the bright band.

---

[2]Other, partly contradictory definitions of convection will be discussed in Section 4.3.

With lower altitude and warmer temperature the inner icy cores of the particles start to collapse. Besides, rain drops ($v_T \sim 5 - 10$ m s^{-1}) fall faster than ice ($v_T \sim 1 - 3$ m s^{-1}) particles, so that there are smaller particles and less per unity volume, which results in a decreased reflectivity (Houze, 1993).
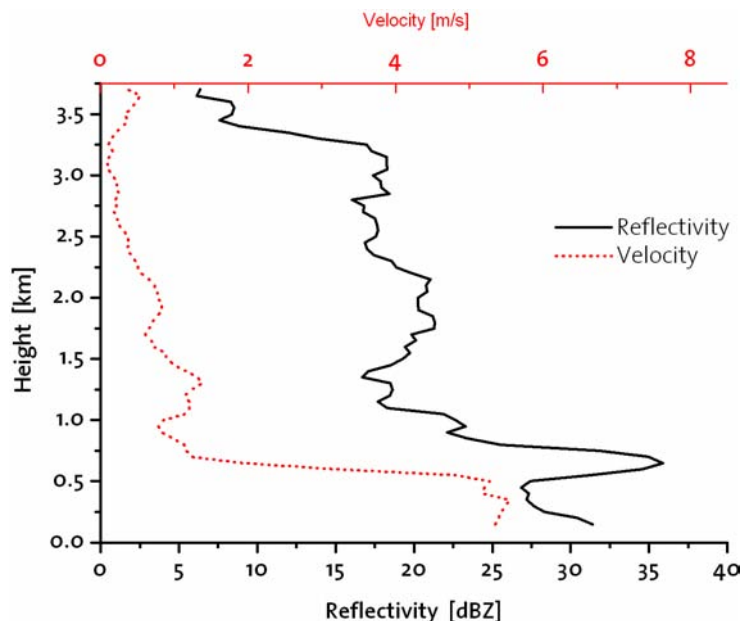

Figure 2.6: *Typical vertical reflectivity and velocity profiles for stratiform precipitation.*

2.3.3 Stability of stratification

Temperature gradients

A process where no heat exchange takes place between a subsystem and its environment is called adiabatic. If a dry air parcel rises adiabatically, the temperature decreases with the dry-adiabatic lapse rate by

$$\Gamma := -\frac{dT}{dz} = \frac{g}{c_p} = 0.00981 \, \mathrm{K} \, \mathrm{m}^{-1} \quad , \tag{2.42}$$

where c_p is the specific heat of dry air at constant pressure. A definition often used in this context is the potential temperature θ. This is the temperature an air parcel would have, if it was brought dry-adiabatically to sea level pressure. The temperature of a rising water saturated air parcel

decreases less, because the latent heat of evaporation L_e is released due to a phase transition from gas to liquid. The saturated-adiabatic lapse rate is (Pruppacher and Klett, 1997)

$$\Gamma_s\,[K/m] := -\frac{dT}{dz} = \frac{g}{c_p + L_e\frac{d\rho_{w,\text{sat}}}{dT}}\quad, \tag{2.43}$$

where $\rho_{w,\text{sat}}$ is the saturation density of the water vapor in the air. It is assumed, that the parcel is in hydrostatic equilibrium with its environment.

Quantification of stability

In order to receive a criterion for stability, we investigate now the reaction of a moist but unsaturated air parcel (index p) of density ρ_p on an infinitesimal vertical displacement δz. The time rate of change of vertical velocity w (positive for updraft) can be written

$$\frac{dw}{dt} = \frac{d}{dt}\left(\frac{d\delta z}{dt}\right) = -\frac{1}{\rho_p}\frac{dp_p}{dz} - g\quad. \tag{2.44}$$

We assume an ideal ambient fluid (index a) with density ρ_a, and that the rising air parcel is in hydrostatic equilibrium with the ambient air, i.e. $p_p = p_a$ and $\delta p_a/\delta z = dp_p/dz$, where with the ideal gas law

$$\frac{\delta p_a}{\delta z} = -\rho_a g\quad. \tag{2.45}$$

Thus, a combination of the Equations 2.44 and 2.45 yields

$$\frac{d^2(\delta z)}{dt} = -g\left(1 - \frac{\rho_a}{\rho_p}\right)\quad. \tag{2.46}$$

With the definition of buoyancy

$$B := -g\left(\frac{\rho_a - \rho_p}{\rho_p}\right) \tag{2.47}$$

we can re-write Equation 2.46

$$\frac{dw}{dt} - B = \frac{d^2\delta z}{dt^2} - \frac{\delta B}{\delta z}\delta z = 0. \tag{2.48}$$

The term $-\delta B/\delta z$ is the square of the buoyancy or Brunt-Väisälä frequency N_B which is a measure for stability. It quantifies the reaction of an air parcel to the infinitesimal displacement δz. N_B^2 is positive for stable, negative for unstable, and zero for neutral stratification. In Emanuel (1994) it is shown that the buoyancy frequency for moist, unsaturated air is given by

$$N_B^2 = -\frac{\delta B}{\delta z} = \frac{g}{\theta_v}\frac{\delta\theta_v}{\delta z} \quad , \qquad (2.49)$$

where θ_v is the virtual potential temperature. This is the potential temperature dry air had at the same density and pressure as given moist air.

Also if conditions are stable, convection can be triggered by forced upward motion or by perturbations of moisture or temperature (Hultgren, 2002). The Rayleigh-Bénard theory describes aspects of the influence of thermal instability. Another possible source for instabilities is the vertical shear of the horizontal wind, as described by the Kelvin-Helmholtz instability (Houze, 1993, p. 57).

If a moist air mass is forced upward, e.g. by orographic effects, it reaches saturation at a certain altitude. Calculations for the supersaturation of water vapor in clouds can be found in Korolev and Mazin (2003). It is difficult to determine, if supersaturation prevails or when it is reached, and what drop size distributions result. This depends strongly on the presence and type of cloud condensation nuclei.

In the case of thermally induced convection, saturation is reached at the convective condensation level (CCL). This is the level where the ambient air has the temperature that corresponds to the dew point temperature of air parcels close to the ground. If such a parcel is heated to such an extent that it reaches the so-called convective temperature, it can rise dry-adiabatically to the CCL and becomes at this level saturated. For the case of forced convection, the height level where saturation is reached is called the lifting condensation level (LCL). If the upward forcing continues or other (thermal) effects are added, and the stratification of the surrounding air is sufficiently dense, a point can be reached, from where an air parcel continues to rise without forcing. This is the level of free convection (LFC). From here, the parcel moves actively until it reaches the level of neutral buoyancy (LNB). The amount of potential energy is called CAPE (convective available potential energy) and can be determined by soundings. The CAPE of a parcel at level i is given by (Emanuel, 1994, p. 169)

$$\text{CAPE}_i = \int_i^{\text{LNB}} B\,dz \quad , \qquad (2.50)$$

which is only defined for buoyancy $B > 0$ (see Eq. 2.47). If there is no background wind shear,

the maximum kinetic energy a parcel can gain is given by the potential energy and the maximum possible vertical velocity w_{max} can be estimated by

$$w_{\text{max}} = \sqrt{2 \cdot \text{CAPE}} \quad . \tag{2.51}$$

Additionally during lifting, entrainment can take place, which is the mixing of surrounding air into the considered air parcel. More complicated effects can be caused by precipitation particles. For example, downdrafts are produced if water evaporates or ice particles melt. In that case, the ambient air has to provide a part of the latent heat. Thus, it is cooled down and its density increases. Additionally, sedimenting condensed water exerts a drag on the air (Emanuel, 1994, p. 338). Or, if a supercooled cloud droplet freezes on graupel latent heat is released, the surrounding air becomes warmer and a positive buoyancy is induced.

2.3.4   Flow over and around a mountain

If no thermal effects take place, the potential energy necessary to lift an air mass over a mountain top has to be provided by its kinetic energy. The sum of potential and kinetic energy

$$\frac{1}{2}u^2 + g(H + h_m) = \text{constant} > 0 \tag{2.52}$$

is positive. H is the thickness of the fluid, h_m the height of the mountain, and u the horizontal velocity of the air flow. It can be shown (Houze, 1993, p. 516) that the smaller the value of the Froude number

$$\mathrm{F}r := \frac{u^2}{gH} \quad , \tag{2.53}$$

the greater the probability that the flow is blocked and can not flow over the mountain. Further, it is shown in Houze (1993, p. 516), that for a continuously stratified fluid blockage occurs if the term

$$\frac{u^2}{N_B^2 h_m^2} \ll 1 \quad . \tag{2.54}$$

N_B is the buoyancy frequency (Eq. 2.49). In case of a three dimensional peak, the air searches its way laterally around it. If $u^2/(N_B^2 h_m^2) \gg 1$ the air flows over the mountain.

Chapter 3

Instrumentation and preparation of data

3.1   Design of the measurement setup

The basic idea of the measuring setup is to be able to make measurements on different height levels and to combine in-situ and remote sensing techniques. The ideal situation would be to monitor a precipitating cloud from the distance with a vertically pointing radar and to simultaneously perform directly above the radar in-situ measurements. The latter could be, for instance, size and velocity measurements with the hydrometeor velocity and shape detector (HVSD) or Formvar sampling. A method was chosen which is, compared to airborne measurements, cheaper and easier feasible: the in-situ measurements are done on a mountain. It has to have a steep slope towards the mean flow. On this front side, there should be a measuring station at the base of the mountain with the vertically pointing radar.

The location should be, on one hand, chosen in a way that the distance from the sloping terrain is large enough that the flow is not strongly orographically influenced. On the other hand, it should be close enough that the time for possible changes in the hydrometeor composition is short. Also, if there are any preliminary mountains, they should be significantly lower in order not to disturb the approaching flow. Thus, a proper choice would be to have two measuring sites at two different height levels, which are vertically as distant as possible but horizontally close.

For the field campaign RAMS (Riming, aggregation and mass of snow) during winter 2002/03, Mount Rigi was chosen as measuring site. It has a height of 1798 m and is situated in Switzerland close to Lake Lucern (8° 29' E, 47° 03' N). Figure 3.1 shows a schematic of the setup. The steep slope of Mount Rigi, where the radar is situated at the base, faces to north-west. Thus, this lower site, which is at 438 m above sea level, is appropriate for the most frequent west to north wind conditions. The higher elevated site is not at the top of Mt. Rigi but at Rigi Staffel at a height of 1610 m above sea level or 1172 m above the radar, resp. The horizontal distance is approximately 3650 m and corresponding to a direction of $\approx 280^\circ$ (with north corresponding to 0°, cf. Fig. 3.2).
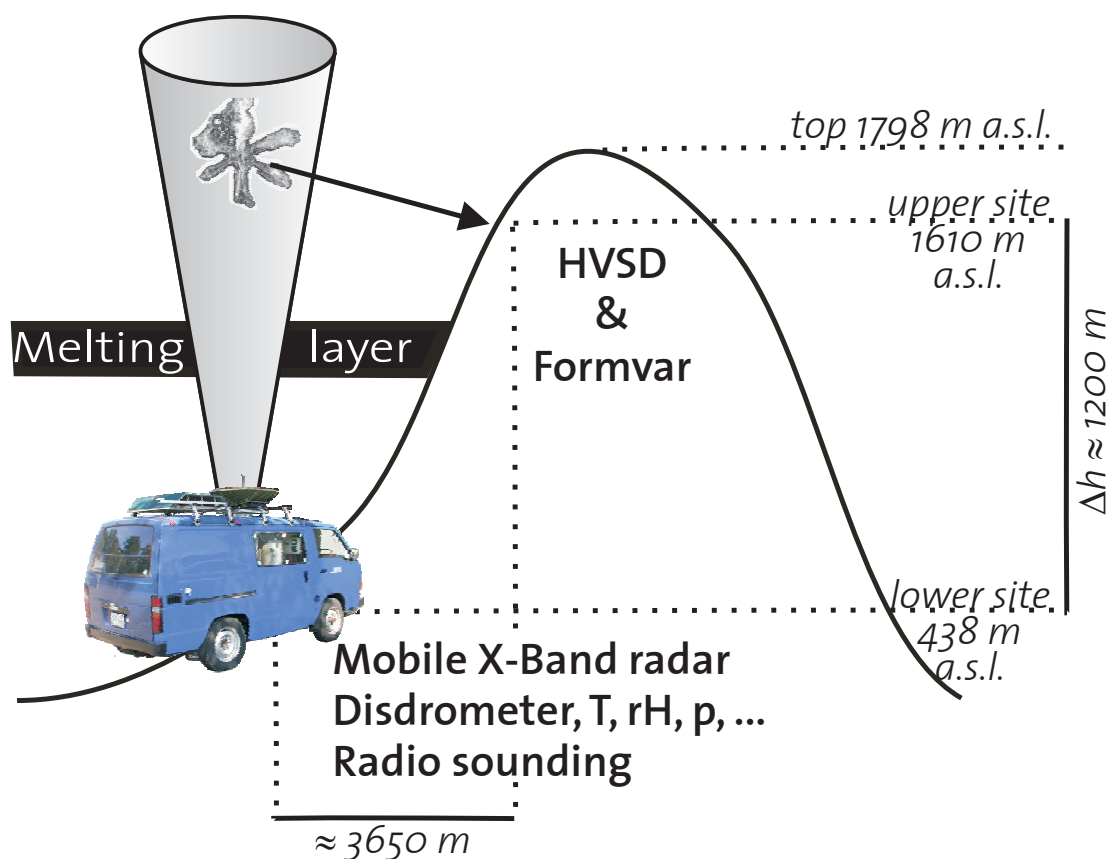
Figure 3.1: *Setup scheme with two locations, one at the base and the second close to the top of the mountain. The lower site is for the most frequent west till north wind conditions on the upwind side.*

At the base station there were the mobile X-Band radar and a Joss-Waldvogel-disdrometer for measuring raindrop size distributions as well as standard meteorological instruments. Also radio soundings were performed. In most of the cases, the melting layer was at a height in between the two sites. At the upper station, there was the HVSD and, in addition, Formvar samples were taken. The region of the measuring site was monitored with two scanning C-band Doppler radars: One is by the Swiss Federal Institute of Technology (ETH) at Zürich-Hönggerberg, and the other one by MeteoSwiss at Mt. Albis. Because these two radars and Mt. Rigi are approximately on one line, the radial Doppler velocity information is redundant. Therefore a dual-Doppler wind field retrieval is for this measuring area of restricted value, and only single-Doppler wind fields have been used. Figure 3.2 shows a sketch of the surrounding of Mt. Rigi including the two measuring sites and the direction towards the ETH scanning radar.
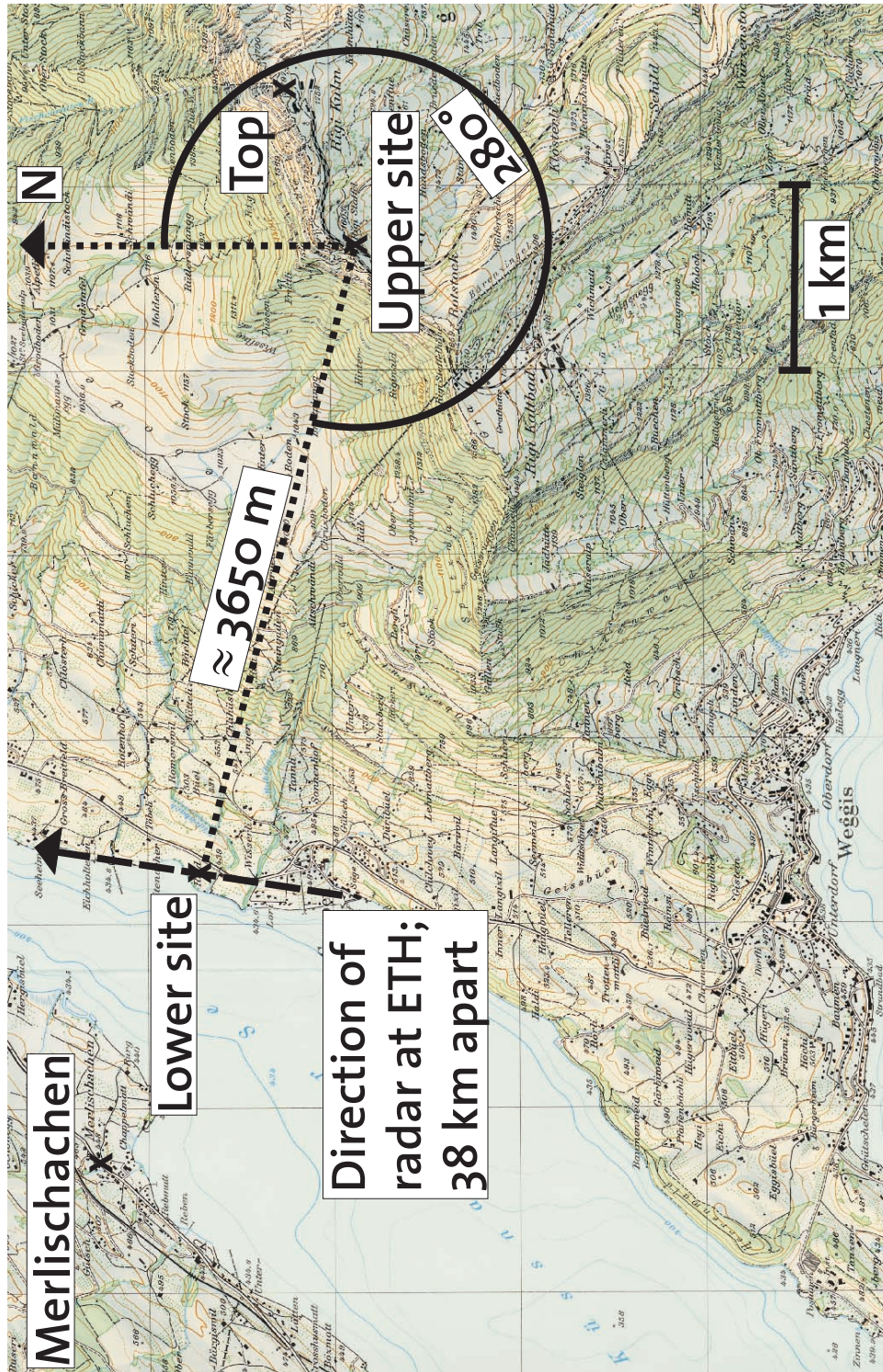
Figure 3.2: *Surrounding of Mt. Rigi including the two measuring sites (Underlying map reproduced with permission of swisstopo (BA046566).)*

3.2   Mobile X-band radar

3.2.1   Technical data and modernization

The mobile radar of the Institute for Atmospheric and Climate Science (IAC*ETH*) at ETH-Zürich is a vertically pointing, non-scanning Doppler radar with a wavelength of 3.2 cm. This is in a wavelength range which is called X-band. The radar (Photo in Fig. 3.3) is mounted onto a small van and is thus easily transportable. It only needs a standard power supply to run.

Table 3.1 summarizes its most important specifics. With the wavelength of 3.2 cm the radar is very well suitable for research on microphysics of precipitation. The high Nyquist velocity (see Eq. 2.35) of ± 32 m s^{-1} together with the high velocity resolution (see Eq. 2.31) of 0.125 m s^{-1} makes it suitable for the broad range of hydrometeors from slowly falling snow over rain up to hail.

Figure 3.3: *Photo of the van on which the X-band radar is mounted. The antenna is on the roof.*

Table 3.1: *Overview over the technical data of the mobile vertically pointing X-band radar of the Institute for Atmospheric and Climate Science (IACETH) at ETH-Zürich.*

Wavelength	3.2 cm (X-band)	Antenna	vertically pointing
Nyquist velocity	32 m s^{-1}	Beamwidth	2.4°
Height resolution	50 m	Peak power	90 kW
Time resolution	1 s (adjustable)	Average power	80 W
Number of FFT samples	512 (adjustable)	Maximum height	in practice limited by amount of data
Velocity resolution	0.125 m s^{-1} (adjustable)	Pulse repetition frequency	4.0 kHz

Modernization

During the duration of this thesis, the radar has been modernized, mainly by computerizing the data acquisition part. Figure 3.4 shows a photo of the interior of the radar van. The radar itself is on the right, the main steering unit in the middle and the computer for data acquisition on the left.

Figure 3.4: *Photo of the interior of the van with the radar. The radar itself is on the right, the main steering unit in the middle and the computer for data acquisition on the left.*

Figure 3.5 gives a schematic overview on the data transmission. The steering unit contains a Quartz, which synchronizes the pulse repetition frequency (PRF = 4 kHz) of the radar, the trigger signal (4 kHz) for the start of the data acquisition and the sampling rate (3 MHz). The PRF is the frequency, with which pulses are transmitted. The returning signal received by the antenna is logarithmically amplified and converted by the steering unit into three channels: reflectivity, cosine and sine component of the phase. Started by the trigger, all three channels of 512 (standard, but adjustable) subsequent pulses are scanned by the data acquisition card. The sampling rate determines here the height resolution to 50 m. 1 s (standard, but adjustable) after the previous one the next set of pulses starts. As part of this thesis, a software has been written in the graphical programming language Labview (by National instruments: www.ni.com) which handles the complete analysis, storage and display of the data.

Thus, because of the modernization high time and velocity resolutions are reached, and a storage of huge data amounts is feasible. The radar has now the capability of saving the full Doppler spectrum information for all height steps. The combination of values chosen for maximum height h_{max}, number of samples per FFT n_p, and time resolution t_{res} determine the amount of data. For example, one hour of measurement results with h_{max} = 10 km, n_p = 512, and t_{res} = 1 s in 2 gigabyte of data, if stored in a special binary format. If changing this parameter combination, the limiting factors that are disk writing speed and capacity of the two processors have to be considered. Doppler spectra, reflectivity and velocity are displayed in real time on the screen. The Doppler spectra can also be displayed off-line as a movie. Examples for images by the radar are given in Figure 3.6 for reflectivity and Doppler velocity.[1]

---

[1] Examples for Doppler spectra can be found in Figure 5.14.
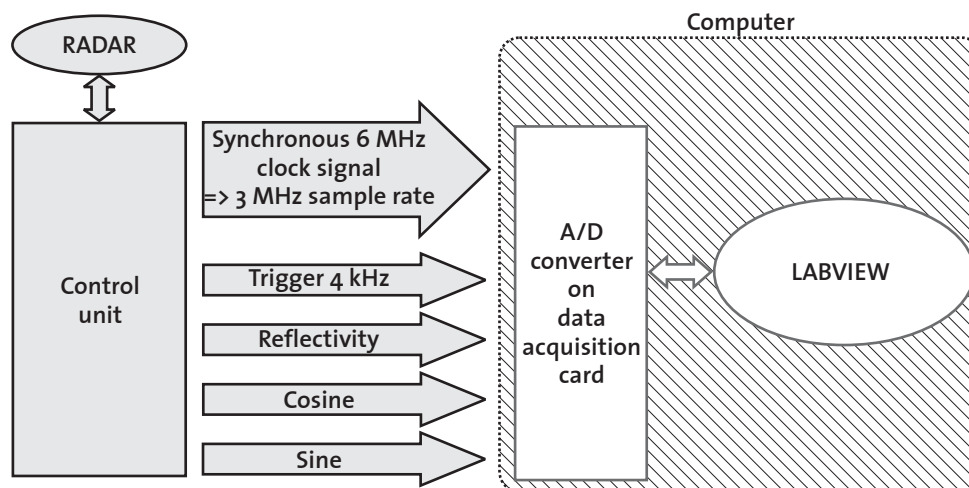
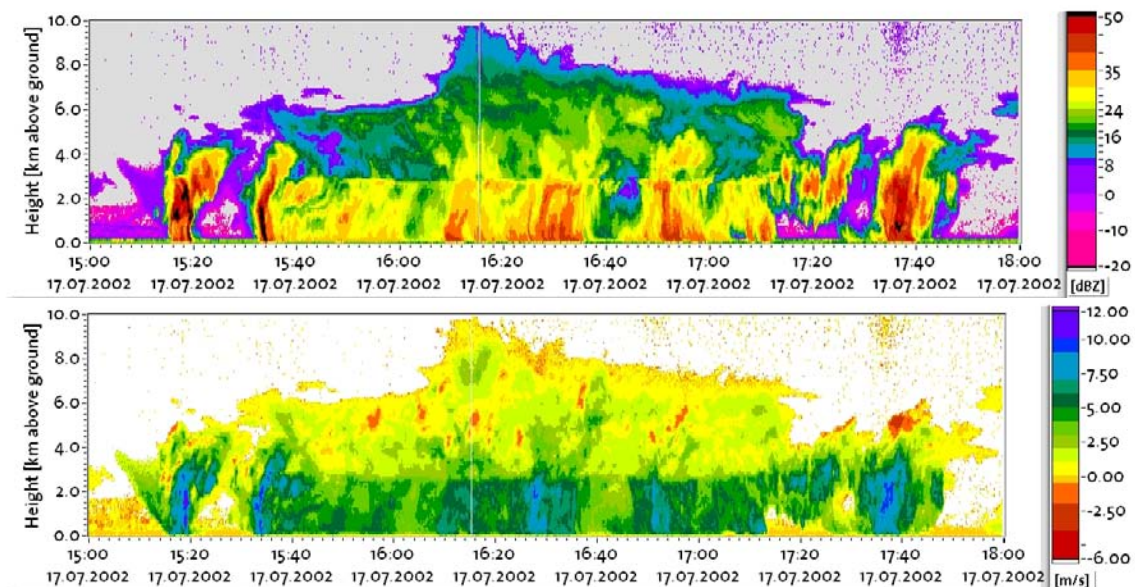**Figure 3.5:** *Schematic overview over the data transmission.*

Figure 3.6: *Example for reflectivity and velocity displays in strongly convective rainfall.*

3.2.2 Calibration

Despite of the difficulties with calibration for radars, it is necessary to find a relation between the power of the electromagnetic radiation at the receiving antenna and the voltage at the data acquisition card after amplification and pre-processing. The 12 bit digital data acquisition card has output values n_V between 0 and 4096. Because logarithmic amplification is used, a linear relation is expected between reflectivity in logarithmic units and n_V

$$Z[dBZ] = a_V \cdot n_V + b_V \quad . \tag{3.1}$$

To determine the parameters a_V and b_V, a microwave generator was mounted instead of the feed in the middle of the radar antenna. Microwaves with known power were generated and sent through an absorber into the wave guide. In the weather radar Equation (Eq. 2.19), there is a dependency of the received power from the distance r of a scatterer. Therefore, a constant injected microwave power is equivalent to varying reflectivity depending of the distance of the source. Different distances are realized through different run times of the signal. These are the times between transmission of the trigger and the arrival of the signal (cf. Eq. 2.26). In order to eliminate the influence of distance from the measurement, the logarithmic amplifier has a time dependent amplification, which is triggered synchronously with the pulse repetition frequency. Finally, for calibration with an artificial constant microwave signal, the radar equation has to be inverted. Figure 3.7 shows for the performed calibration the simulated equivalent reflectivity versus distance from the radar. Each curve indicates a constant microwave power, which was varied between 0 and -60 dBm through a directional coupler. Due to varying attenuation by, e.g. cables, additionally up to 60 dB, have to be subtracted.
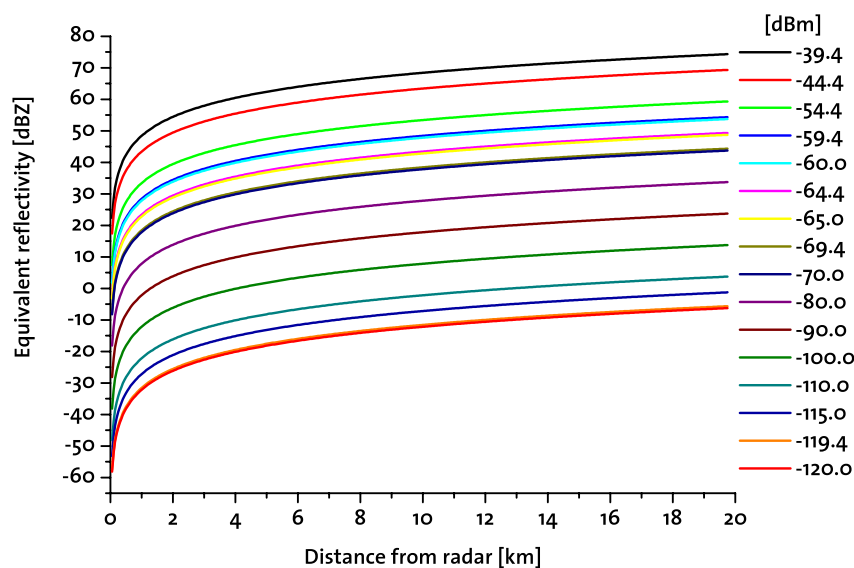
Figure 3.7: *Simulation of reflectivity with a microwave generator for calibration purposes. The graph shows the simulated equivalent reflectivity over distance from the radar.*

The digital output values n_V were converted into reflectivity values with Equation 3.1. A least square fit yields in $a_V = 20.98$ and $b_V = 2519.8$. These parameter values have been used for evaluation of the radar data.

In Figure 3.8 the reflectivities measured with this calibration are compared to the generated values. The thick blue line marks unity. Some points (non-filled symbols) deviate stronger from unity. They all come from the same data set and have been filtered out. Technically, there is a gas-discharge cell in the radar which prevents the sensitive receiver from damage by the trans-

mitted power. It takes a short while until the effects of the gas-discharge have dissolved. Hereby, stronger deviations for low distances r can be explained. Deviations from the unity line come from the with respect to Equation 3.1 not ideal behavior of, for instance, the amplifier. They could be corrected for by a distance and reflectivity dependent correction matrix.
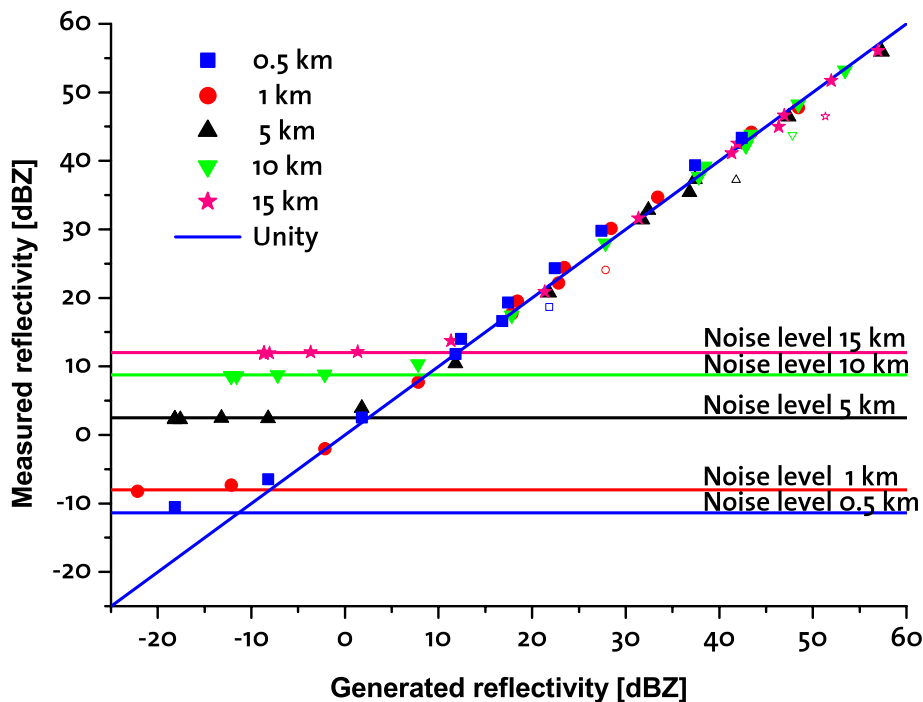

Figure 3.8: *Comparison between reflectivities measured with the calibration parameters $a_V = 20.98$ and $b_V = 2519.8$ and the generated value. The distance dependent noise levels are marked, too.*

Due to the non-linear amplification also the noise is amplified distance dependent. The noise levels can be obtained from Figure 3.8, where the measured values become for low reflectivities constant, if the distances become smaller. The distance dependent noise level [dBZ] is composed in Figure (3.9). This gives also the sensitivity of the radar. This noise level is reached about 15 min after start up of the radar.

Reflection of radar radiation by ground or other non-meteorological targets, is called clutter. For a vertically pointing radar, this comes often from side lobes which are secondary maxima of a non-ideal beam. For a specific measurement site, clutter maps could be used to filter data.
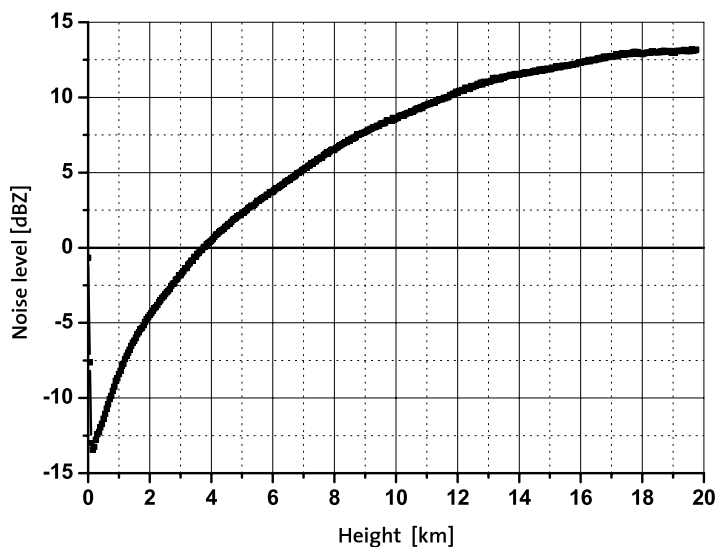
Figure 3.9: *Plot of distance or height dependent noise level, respectively. This gives also the sensitivity of the radar.*

Disdrometers[2] measure drop size distributions of rain. With Equation 2.22 the reflectivity factor can be calculated, and then an expected received power is obtained with relation 2.24. As a meteorological test for the technical calibration of the radar a comparison with data from a Joss-Waldvogel-disdrometer was done. It is common practice to use the results for an additional meteorological calibration. This has not be done for the data in this thesis, because there was already a good consistency after the technical calibration.

For comparison a convective summer case was chosen, which had a strong variation in rain rate and thus also in reflectivity. Noise filtered reflectivity and Doppler velocity are shown in Fig. 3.6. In Figure 3.10 disdrometer data is compared for a two hour period with reflectivity at a height of 200 m. This distance from the ground was chosen to minimize the influence of the effects of the gas-discharge cell to reduce the received power and thus the measured reflectivity on the lower height levels (Sec. 3.2.2). If the minimum compared reflectivity is set to 5 dBZ, there is a correlation of 0.87 between these data sets with a standard deviation of 3.99 dBZ. But the strong convective character of the cells that are present in the beginning and at the end of the shown phase can lead to errors in comparison, i.e. the radar sees hydrometeors 200 m above the ground that are different from those observed by the disdrometer. Restricting the considered time to 15:45 till 17:00 LT, the correlation becomes 0.96 and the standard deviation 1.78 dBZ, which is a good agreement.
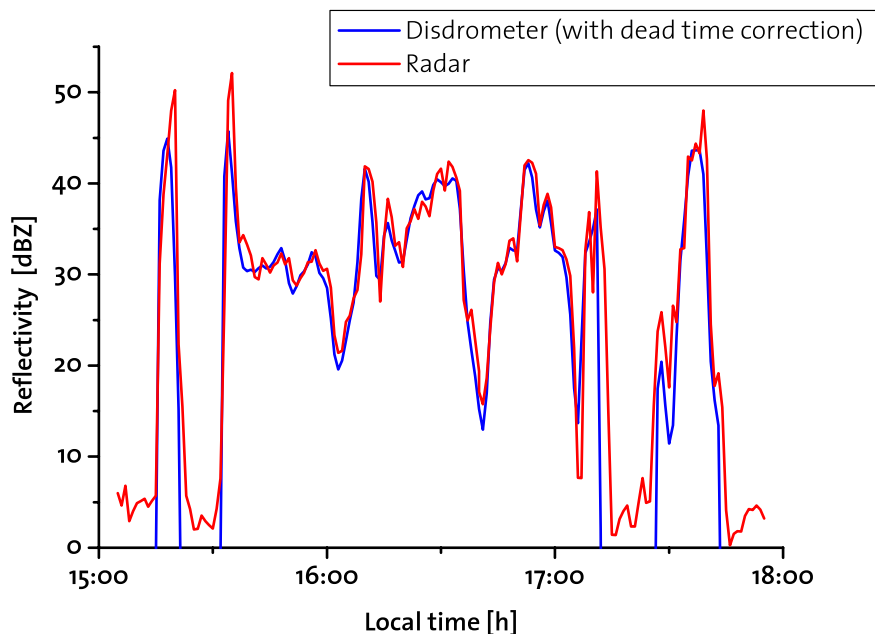
---

[2]cf. Sec. 3.5

Figure 3.10: *Comparison between reflectivity computed from disdrometer data and measured reflectivity 200 m above ground for a two hour period of convective summer case.*

3.2.3   Preparation of radar data

Figure 3.11 shows a schematic of the algorithms for the computation of reflectivity, Doppler velocity and Doppler spectra out of the three channels entering the computer via the data acquisition card. After calibration (Sec. 3.2.2), the digital data from the reflectivity channel can be converted to dBZ units (Eq. 3.1). The same number of subsequent pulses n_p is used for the fast Fourier transformation as well as for averaging the reflectivity. System noise can be removed by comparing the signal with the noise curve (Fig. 3.9). The two channels for sine and cosine are used to reconstruct the complex radar signal. For every height, the n_p input values are weighted with reflectivity and smoothed with a Hamming window. On the complex signal, a fast Fourier transform is performed and the Doppler spectra result. Doppler spectra split up reflectivity into the contribution of each velocity bin. Before computation of the moments, a running average over three pulse sets of n_p pulses (typically 3 seconds) is calculated. Now the moments can be computed for every height step. The reflectivity can either be obtained from the zeroth moment (Eq. 2.32) of the Doppler spectrum or by averaging the reflectivity channel. Only small differences exist between these two values because of the running average and windowing. Doppler velocity is given by the first (Eq. 2.33) and spectrum width by the second (Eq. 2.34) moment.
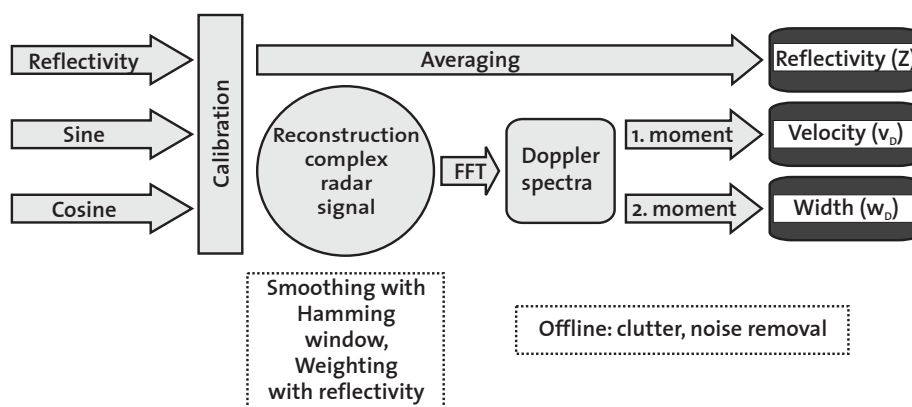
Figure 3.11: *Schematic of the algorithms for the computation of reflectivity, Doppler velocity and Doppler spectra out of the three radar channels.*

3.3   Scanning C-band Doppler radar

Technical data for the scanning C-band Doppler radar by the Swiss Federal Institute of Technology (ETH) at Zürich-Hönggerberg (cf. map in Fig. 3.2) can be found in Table 3.2. This radar has been used for observation of precipitation patterns in the area of the measuring site. Though radars only measure the radial component of wind velocity, 3D wind fields can be obtained by either combining the information from several scanning Doppler radars or by making assumptions about the wind field to be non-divergent. Techniques of single or dual Doppler wind field retrieval and de-aliasing of folded wind fields are described in detail in Wüest (2001). But, for Mt. Rigi only the single Doppler technique has been used, because the second available scanning radar by MeteoSwiss is installed on Mt. Albis (cf. map in Fig. 3.2) which is in line with the ETH scanning radar and Mt. Rigi and thus providing redundant velocity information.

Table 3.2: *Overview over the technical data of the scanning C-band Doppler weather radar at ETH Zürich-Hönggerberg.*

Wavelength	5.33 cm (C-band)	Pulse repetition frequency	1200 Hz
Nyquist velocity	16 m/s	Pulse width	0.5 μs
Antenna	scanning	Longitude	8.512°
Antenna gain	40 dB	Latitude	47.408°
Peak power	280 kW	Altitude	540 m above sea level
Beamwidth	1.65°		

3.4   MeteoXrad

Standard meteorological parameters have been measured with the automatic meteorological sta-
tion "MeteoXrad" which is mounted in and on the radar van. A new software, written in Labview,
has been developed during this thesis for data acquisition and evaluation. The measurements
are repeated and saved every 10 s. The wind information is averaged over the first 5 s of each
period. Table 3.3 lists the measured parameters and some technical data.

Table 3.3: *Parameters measured by the instruments of the automatic meteorological station "Me-
teoXrad" and the Joss-Waldvogel-disdrometer (cf. Sec. 3.5)*

Parameter	Producer/Instrument	Range
Temperature	Vaisala Humicap, Pt 100	-50 to 50 $^\circ$C
Relative humidity	Vaisala Humicap, Pt 100	0 - 100 %
Air pressure		$>$ 800 hPa
Wind velocity	Vaisala; cup anemometer	
Wind direction	Vaisala; vane	
Rain total	Tipping bucket rain gauge	resolution 0.1 mm
Drop size distribution	Joss-Waldvogel-disdrometer	

3.5   Joss-Waldvogel-disdrometer

Disdrometers are used to measure drop size distributions (DSD) in rain. A Joss-Waldvogel-
disdrometer (Joss and Waldvogel (1967); photo in Fig. 3.12) is mounted on the roof of the radar
van. A falling raindrop translates its momentum onto a stiff foam body and a membrane. The
momentum is converted into an electromagnetic signal with help of a coil. Finally, from this signal
the mass and the diameter of the raindrop can be deduced assuming a distinct fall velocity-
diameter relation. After a large drop moved the coil, the system needs a short instant to be
sensitive again for small drops. This can be corrected for by a so-called dead time correction.
But, this can only be done by assuming certain regularities in the drop size distributions. The
data of small droplets that can not be detected, if there are strong background noises can not
be recovered. During the case studies, dead time correction was normally not applied. The
size classes, into which the diameters of drops are divided by the disdrometers, can be found in
Table 3.4. Besides drop size distributions, rain rate (Eq. 2.5), rain total and reflectivity (Eq. 2.22)
can be calculated out of disdrometer data.

Figure 3.12: *Photo of a Joss-Waldvogel-Disdrometer.*

Table 3.4: *Diameter classes for the Joss-Waldvogel-disdrometer.*

class	mean diameter [mm]	diameter range [mm]	class	mean diameter [mm]	diameter range [mm]
0	0.359	< 0.406	10	1.9115	1.80 - 2.10
1	0.455	0.40 - 0.50	11	2.269	2.10 - 2.45
2	0.5495	0.50 - 0.60	12	2.5995	2.45 - 2.75
3	0.6565	0.60 - 0 .71	13	2.8915	2.75 - 3.05
4	0.774	0.71 - 0.83	14	3.1885	3.05 - 3.35
5	0.9135	0.83 - 1.01	15	3.541	3.35 - 3.75
6	1.1135	1.01 - 1.21	16	3.944	3.75 - 4.15
7	1.3315	1.21 - 1.42	17	4.385	4.15 - 4.65
8	1.5130	1.42 - 1.60	18	4.882	4.65 - 5.20
9	1.6625	1.60 - 1.80	19	5.4475	> 5.2

3.6   Radio soundings

Radio soundings have been performed from the lower site directly beside the mobile radar. A software was developed in Labview for the communication with the decoder and analysis of the data. The soundings measure in one second intervals temperature, relative humidity and pressure. For these sounding, there was neither wind measurements available nor could the horizontal position be followed. Only for one case, additional soundings which include wind information could be obtained from the Swiss military weather service. They were launched from the area of Merlischachen (see map in Figure 3.2).

3.7   Replication of ice precipitation by the Formvar method

The preparation of snow crystal replicas with the Formvar method is described in detail in Schaefer (1956). Polyvinyl formal (Formvar) is dissolved in ethylene dichloride to get a solution between 0.5 and 3 per cent per weight. This solution is stored optimally between 0 and -5° C. Before sampling, a thin layer of the solution is put onto a microscope glass slide. This slide is exposed to snowfall for 10 to 30 seconds, depending on snowfall intensity, until about half of the surface of the glass plate is covered with ice particles. These will, on one hand, partly sink into the solvent and, on the other hand, the solvent has the property to creep over the ice surface. Thus, if the amount and concentration of the solution is chosen correctly for the size of the particles, the whole surface of the ice particles will be coated. After the exposure the plate has to be kept cold in a dry environment until the excess of the solvent is evaporated. A thin hardened plastic membrane will build, which is like a transparent skin, following the surface of the ice particle. If these replica are now taken to the warm, the originate snow crystals melt and evaporate through the coating. The resulting, three dimensional footprints are now preserved for years and can be studied under a light microscope for, e.g., determining crystal habit and riming degree. Examples for images of differently rimed ice particles on Formvar replica can be found in Section 2.1.4.

Every sample is analyzed with a stereo microscope. Crystal habit and the degree of riming (cf. Sec. 2.1.4 and Mosimann et al. (1994)) is determined for every sample. The degree of riming was analyzed separately for every crystal type. Finally, an averaged degree of riming was given to every sample. Additionally, a quality factor was given for the quality of each Formvar sample.

3.8 Hydrometeor velocity and shape detector (HVSD)

3.8.1 Measuring principle

The hydrometeor velocity and shape detector (HVSD, see photo in Figure 3.13 a) was developed and built by the Institute for Atmospheric and Climate Science at ETH, Zürich (cf. Barthazy et al., 2004). It measures size and velocity distributions of naturally falling hydrometeors. Figure 3.13 b and c show a schematic drawing of the instrument. The optical part consists of two parallel light sheets, which illuminate two rows of photo cells with 512 elements each. If a part of one of the beams is blocked by an ice particle, the blackening of the corresponding photo cells is recorded. The whole particle is scanned rapidly (with 9470 Hz), while it is falling through the measurement area. Thus, a side view shadow image is received. The second beam is 9.45 mm below the upper one. By measuring the time a hydrometeor needs for the distance between the two beams, the fall velocity can be calculated. To be able to assign to an image from the upper beam a partner from the lower line camera, the images go through a matching process. This is especially important in case of sampling ice particles: If high numbers of ice particles pass the measurement area simultaneously or if they turn around, matching can become difficult. Thus, some particles can not be matched. Then, only size information can be obtained. Detailed descriptions of the instrument and the matching process can be found in Barthazy et al. (2004) and Schefold (2004).

The matching process goes in parallel with the determination of snow particle dimensions. Figure 3.14 points out some of the dimensions, measured by the HVSD. The inner width d_{in} is the maximum extension in any of the horizontal lines of the particle image. It can be measured independently from the velocity of particle motion, because the particles can be considered slow with respect to the scanning frequency. Thus, this parameter can be obtained for both matched and unmatched particles. The outer diameter d_{out} is the maximal horizontal extension of a particle over different lines. Its measurement is influenced by horizontal particle movement which is shearing the particle. It can be corrected for, with help of the difference in horizontal position on upper and lower line camera and thus of the horizontal velocity.

The vertical size resolution is dependent on the vertical particle velocity. A slowly falling particle is scanned more often than a fast one. Thus, the inner height h_{in} has to be stretched or compressed by using the vertical velocity. After height and width are corrected, an ellipse can be fitted to the particle and the major axis gives the maximum dimension d_{max}. Table 3.5 summarizes technical data of the HVSD.
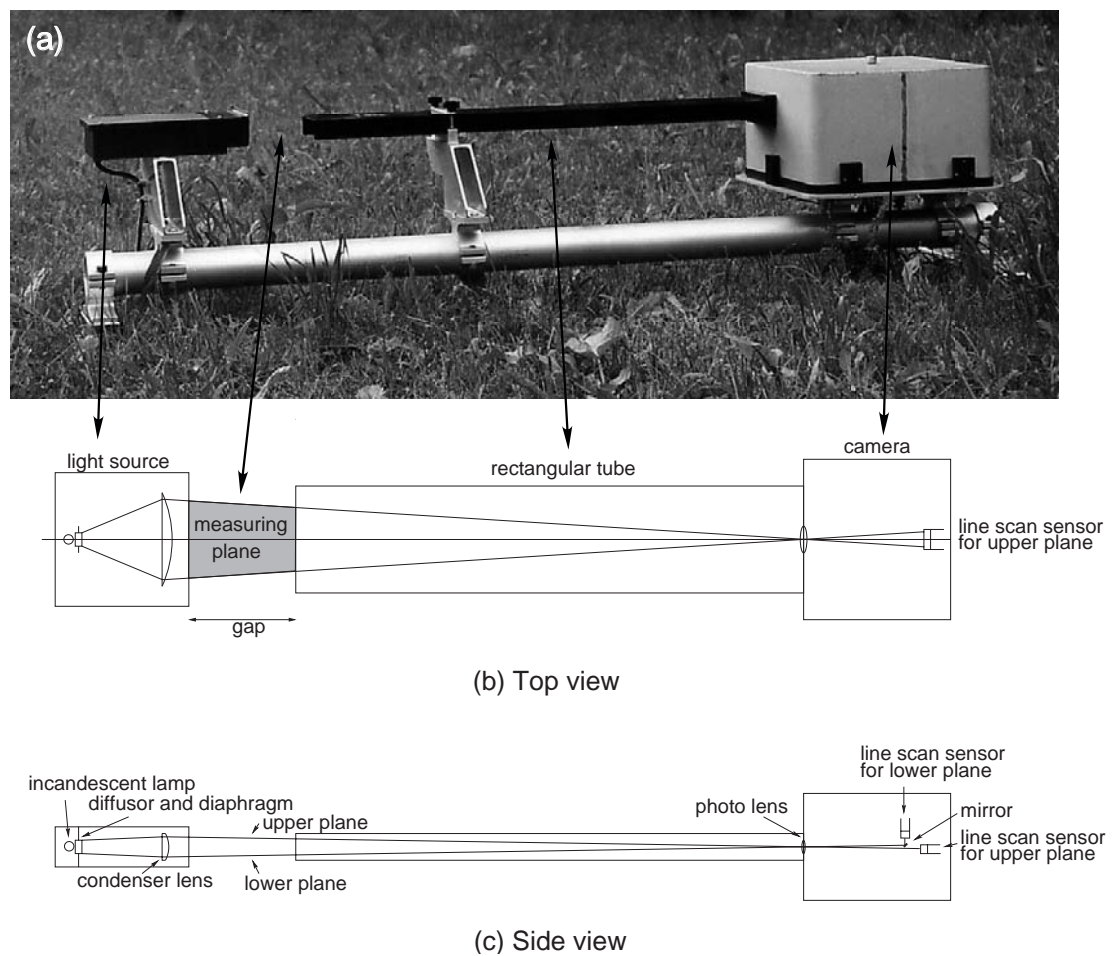
(b) Top view

(c) Side view

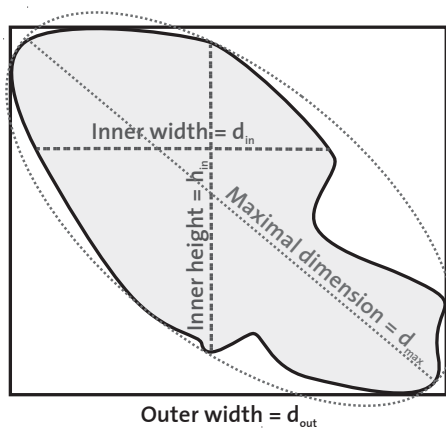**Figure 3.13:** *Picture (a) and schematic drawing in side (b) and top view (c) of the HVSD. From: Barthazy et al. (2004).*

Figure 3.14: *Overview over different diameter types measured by the HVSD.*

Table 3.5: *Technical data of the HVSD.*

Scan rate	9470 Hz
Number of pixels per line	512
Number of measurement planes	2
Vertical distance between planes	(9.45 ± 0.55) mm
Size of measuring planes	$(76.75 \pm 4.25) \times 108.5$ mm
Resolution	(0.15 ± 0.008) mm

3.8.2 Preparation of data: reflectivity, Doppler spectra and velocity for HVSD

For this thesis, the computation of reflectivity and Doppler velocity is the most important of the many possible uses of the HVSD data. Equation 2.39 can be used to calculate the reflectivity from the measured ice particle size distribution. A mass-size relation (Eq. 2.11) has either to be measured or assumed. But the data measured by the HVSD has first to be converted from an area measurement into volume data. For this, the fall velocity is the key issue. But no velocity was measured for particles which could not be matched. Therefore, velocities are estimated from the velocities of matched particles with same diameter range. The diameters are divided into bins. For each bin, the median of the velocities is taken as fall velocity for the unmatched particles corresponding to this diameter bin.

The total size of an particle that is only partly on the images of the line cameras can not be determined. Therefore, particles which touch the edge have been removed. Thus, the active measurement area

$$A_a\,[\text{m}^2] = \frac{(76.75 - D)(108.5 - D)}{1000^2} \tag{3.2}$$

is smaller than the physical dimensions of $(76.75 \pm 4.25) \times 108.5$ mm (Tab. 3.5); A_a is dependent from the particle diameter D which is here given in mm.

The distance h covered by a particle j during the measurement interval Δt is determined by the fall velocity v_j which is measured by the HVSD. Thus the volume V_j for which the particle j is representative is $V_j = A_a \cdot h = A_a \cdot \Delta t \, v_j$. Thus, V_j has to be inserted in Equation 2.39 as a for each particle individual resolution volume. Finally, the reflectivity factor Z_{HVSD} can be computed out of the HVSD data with

$$Z_{\mathrm{HVSD}} \left[\frac{\mathrm{mm}^6}{\mathrm{m}^3} \right] = \sum_j^N Z_j = \left(\frac{6}{\rho_i \pi} \frac{|K_i|}{|K_w|} \right)^2 \sum_j^N a_m{}^2 \frac{D_j^{2b_m}}{V_j}$$

$$= 0.821 \, a_m{}^2 \sum_j^N \frac{1000^2 \cdot D_j^{2b_m}}{(76.75 - D)(108.5 - D) \cdot \Delta t \cdot v_j} \quad , \tag{3.3}$$

where Z_j is the individual contribution of a single particle j to reflectivity. The sum goes over all N particles registered by the HVSD during the measurement interval Δt [s] (typically 60 s). The density of ice is ρ_i = 0.917 [mg mm^{-3}]. D is in mm and v_j in m s^{-1}. a_m and b_m are parameters of the mass-diameter relation (Eq. 2.11), where b_m is dimensionless and a_m has the units mg mm$^{-b_m}$.

The various dimensions measured by the HVSD have been presented in Section 3.8. For comparison, reflectivity has been computed with three diameters D, the inner (d_{in}) and outer (d_{out}) width, and the maximum dimension (d_{max}). The differences will be discussed later. For unmatched particles divided into bins, d_{out} and d_{max}, respectively, have been obtained in a similar way as the fall velocities from the corresponding medians of the matched particles' properties.

For a measurement interval, a velocity value can be computed which is weighted by the reflectivity in the same way as the Doppler velocity for the radar (Eq. 2.33). This "Doppler velocity" for the HVSD can be written

$$v_{D,\mathrm{HVSD}} = \sum_j^N \frac{Z_j \cdot v_j}{Z_{\mathrm{HVSD}}} \quad . \tag{3.4}$$

The particles measured by the HVSD can be split into velocity bins. By computing reflectivity separately for each of these bins a Doppler spectrum is achieved.

3.9   Snow video spectrograph (SVS)

The snow video spectrograph is an instrument constructed by the Desert Research Institute (DRI), Reno, Nevada, to measure the mass of snow particles. It also provides some information about habit and riming degree. In a repeating cycle, a teflon band is first exposed to precipitation for a certain time. The ice particles are kept cold with a cold air stream. Then, the casing is closed and the band heated through a hot fan. The ice particles are filmed during the melting process. Habit and riming can be determined from the images before melting, and the mass out of the diameter of the melted drop. Detailed descriptions about instrument and analysis can be found in Borys et al. (2003) and in Borys (2003). In collaboration with the IAC***ETH***, the NCAR, Boulder, contributed with the snow video spectrograph to some cases of RAMS.

Chapter 4

Methods

4.1 Lag time correction

4.1.1 Motivation for lag time correction

Within a precipitation system, the composition of hydrometeors varies with respect to their number, habit and size distribution. This is valid even within one height level. Thus we have to consider a lag time, if we want to compare hydrometeor properties measured according to the setup described in Section 3.1, i.e. above the lower site by remote sensing and with in-situ data from the upper site. This is the time given regions of the moving precipitation systems need to travel the distance between the two measuring sites. The lag time depends on horizontal velocity and direction of the motion of the hydrometeors. The individual, falling hydrometeors observed at the top station will have been at a higher level, when they were above the radar, if they arrived there earlier. But, these hydrometeors will have grown and thus have changed their properties. However, we can assume, that within a certain horizontal region at a given height level hydrometeors with a similar growth history and composition follow from greater heights. Thus, if the lag time is short compared to the life time of a region within a precipitation system, we can use for comparison the data from that height above the radar which equals the height of the upper station.

Figure 4.1 displays the motivation for lag time correction. The lag time in this case is given by the difference between the time, when the horizontal region of the moving precipitation systems is at the upper site, t_1, and above the lower measuring site, t_0. If in-situ data is used, which is measured at the time t_2 directly at the lower site, different lag times are received; they are given by the difference, $t_1 - t_2$. In both cases, positive lag times mean a later arrival at the upper site. Already Mosimann et al. (1994) used a rough by eye lag time correction, this method is refined in the following sections.
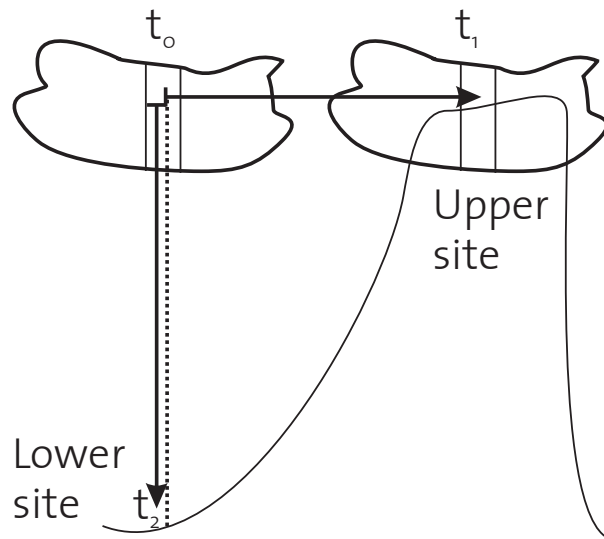
Figure 4.1: *Motivation for lag time correction. Horizontal regions of a moving precipitation system need time to cover the distance between above the lower measuring site and the upper site.*

4.1.2 Computation of lag times

For the computation of lag times t_{lag}, a multitude of quantities could possibly be used, depending on the specific instrumentation. This could either be pairs of data sets from identical instruments, or, data sets, out of which a common quantity is computed. In this thesis, we will use reflectivity as a basis for the computation of lag times. In the given setup (Sec. 3.1), the vertically pointing X-band radar (Sec. 3.2) measures reflectivity directly by remote-sensing; and for the upper site, reflectivity is computed out of the HVSD (Sec. 3.8) data. For this purpose, it has been chosen from the variety of the measured snow flake dimensions: the inner width (d_{in}), outer width (d_{out}) and maximum dimension (d_{max}) (Sec. 3.8). The pre-processing of the HVSD data and the computational steps are described in Section 3.8.2. If not otherwise mentioned, a mass-size relation for graupel-like snow of intermediate density was used: $a_m = 0.059$ and $b_m = 2.1$ (cf. Sec. 2.1.5).

Figure 4.2 shows an overview over the reflectivity computed for all three HVSD-diameters for the period 8:30 until 15:45 LT of the case Nov. 7, 2002. As would be expected, the resulting reflectivities are highest for the maximum dimension, followed by the outer and then by the inner width. The maximum dimension is more susceptible to errors during the matching of snow flake pairs. d_{max} is sensitive to correct matching (cf. Sec. 3.8), mostly because wrong matching leads to errors in vertical and horizontal velocity and thus in wrong corrections performed to receive d_{max}. Occasionally an artefact is produced by the HVSD, which has the highest impact on d_{max}. These errors amplify by raising corresponding diameters to high power in the reflectivity calculation. A filtering would be necessary to avoid these peaks, which stick out in the maximum dimension curve.
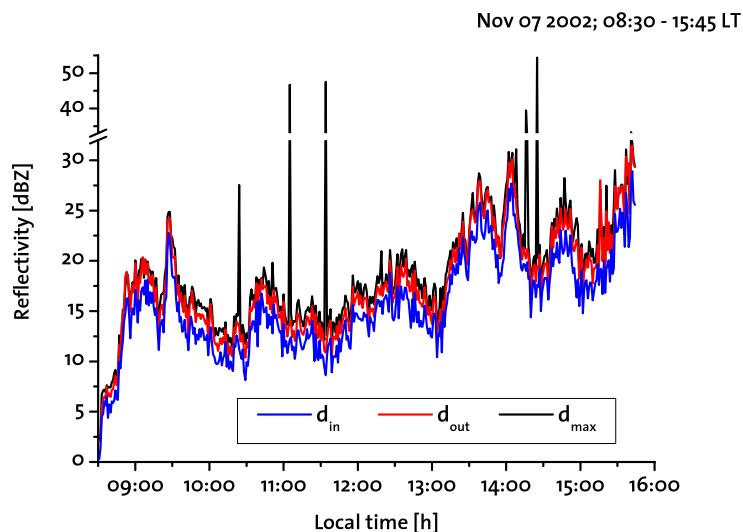
Figure 4.2: *Reflectivity computed out of the HVSD data for three different diameters for the period 8:30 until 15:45 LT of the case of Nov. 7, 2002.*

Finally, a cross correlation (App. B) between the reflectivity computed out of the HVSD data and the directly measured radar reflectivity (height 1200 m above the radar) is performed. For this, one of the data sets was shifted in 5 second steps and each time the correlation between the sets was re-calculated. Figure 4.3 shows the change of the correlation coefficient with varying time shift. The maximum determines the lag time; they are practically identical for inner and outer width. The values are $r = 0.92$ and lag time $t_{\mathrm{lag}} = 355\,\mathrm{s}$ for the inner and $r = 0.91$ and $t_{\mathrm{lag}} = 345\,\mathrm{s}$ for the outer width. The curve for the maximum dimension shows lower correlation (0.79) and slightly different lag time ($315\,\mathrm{s}$). This can mostly be explained by the errors in reflectivity computation for the maximum dimension, which can be seen as peaks in Figure 4.2.
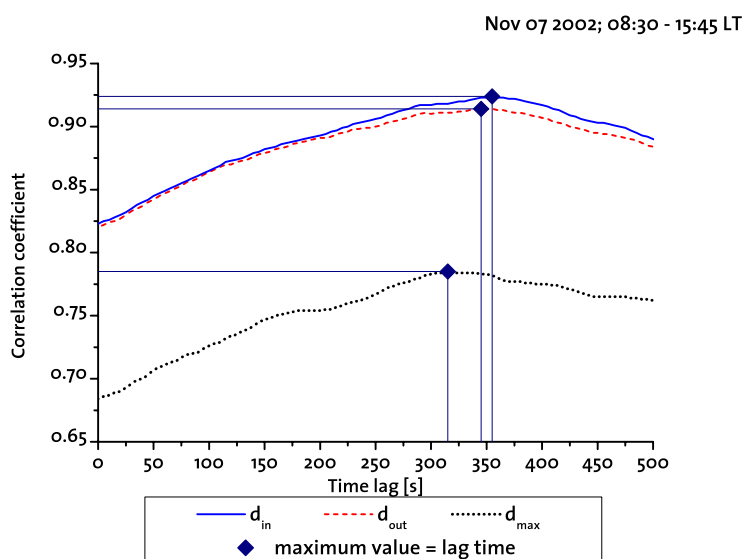
Figure 4.3: *Changes of the correlation coefficient with varying time shift between the data sets, computed for three different HVSD-diameters. The maximum determines the lag time.*

As a test for the robustness of determination of the lag time, correlations have been computed for the three diameters in two additional ways. Firstly, not the logarithmic units of reflectivity [dBZ], but the linear ones [mm^6 m^{-3}] have been correlated. This emphasizes strongly the influence of high reflectivities. For the two values of width similar results are obtained. For the maximum dimension errors are even more emphasized and the results are not anymore useful. Secondly, instead of the normal correlation a rank correlation (App. B) has been performed, which is a test not for linear but for monotone relations. Figure 4.4 gives an overview over the cross correlations and Table 4.1 summarizes the results. For the example case, the averaged lag time is $352\,\mathrm{s}$ if weighting with the correlation coefficients. As there are no mayor differences between the resulting lag times, for the following investigations d_{out} was used.

Table 4.1: *Overview over lag time and correlation values for different ways of computation of reflectivity for the case of Nov. 7, 2002.*

diameter type	correlation		linear units		rank correlation	
	lag time (s)	r	lag time (s)	r	lag time (s)	r
d_{out}	345	0.91	325	0.77	350	0.91
d_{in}	355	0.92	345	0.82	360	0.91
d_{max}	315	0.79	1000	0.09	345	0.88
weighted average over all values: lag time = $352\,\mathrm{s}$						

Figure 4.4: *Graphical overview over lag time and correlation values for different ways of computation of reflectivity for the case of Nov. 7, 2002.*
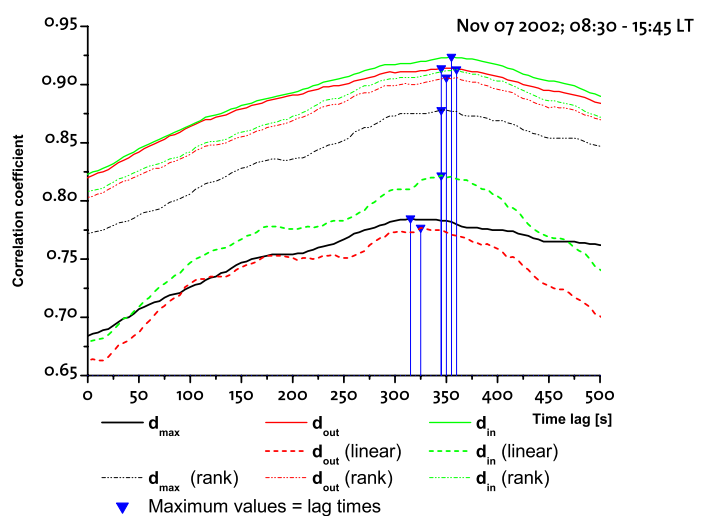
4.1.3 Amelioration of the lag time method

During a case, the lag time will vary if the direction and horizontal translation velocity of the precipitation system changes. Thus, it would make sense to split one case in several periods, which are long enough that each includes a significant amount of data points. For this splitting, it is difficult to define an objective criterion. Therefore, a different approach was chosen. As described in Section 3.8.2, the reflectivities are computed from the HVSD data in one minute time intervals. Each of these time intervals is further referred to as one data point. To receive enough data points for the cross correlation, for each data point the adjacent $\pm$ 15 minutes were selected and correlated to a half an hour of radar data which was shifted in time. In this way a "correlation coefficient field" is received. For demonstration, an example for the case Nov. 7, 2002, of RAMS is shown in Figure 4.5.
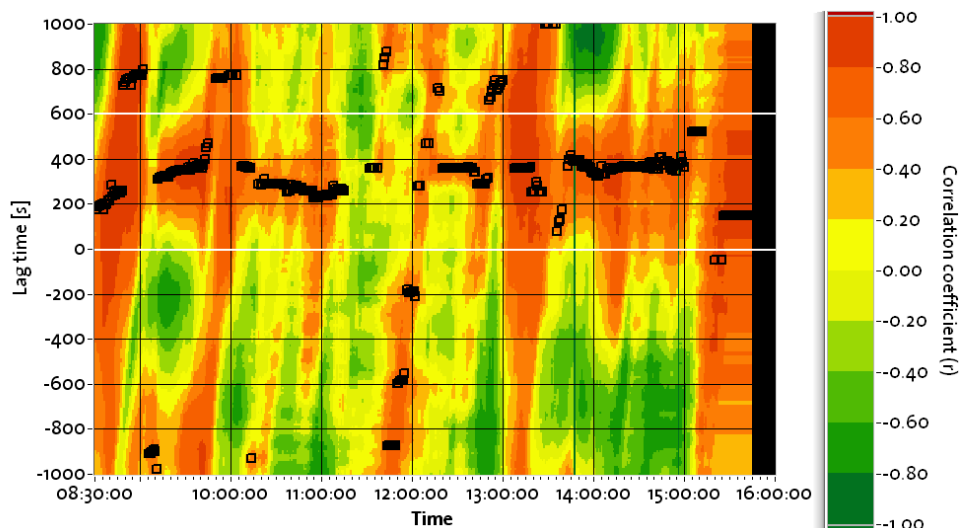
Figure 4.5: *Correlation coefficient field for case Nov. 7, 2002 (with $b_m = 2.1$). The black boxes indicate the resulting lag times.*

Lag time can depend on the choice of parameters in the mass-size relation of the form $m = a_m D^{b_m}$ (cf. Sec. 2.1.5), because they have a strong influence on the computed reflectivity: in linear units, the reflectivity is proportional to the sum of the squared masses of the scattering particles (Eq. 2.39). But the parameter a_m can be drawn outside the sum. And, since correlations are neutral to linear transformation, the choice of the value of a_m has no influence on the resulting correlation coefficient field. Two more lag time fields were calculated with other values for b_m than the standard value $b_m = 2.1$: $b_m = 1.74$ corresponding to stellar crystals with rimed spatial branches and $b_m = 3.31$ for hexagonal plates (cf. Sec 2.1.5). For each of the in total three lag time fields, the highest correlation coefficient was chosen. Thus, three different lag time values were obtained. Only data points with a correlation coefficient greater than 0.5 were considered, and the mean value of the three lag times gave the lag time which was used. A data point was

also discarded, if the standard deviation between these three points was larger than 60 s. The resulting lag times are marked in Figure 4.5 by black boxes. The effect of this ameliorated lag time correction can be seen in Figure 4.6. It shows the radar reflectivity with and without lag time correction compared to the HVSD reflectivity based on the d_{out} and the mass-size relation of graupel-like snow of intermediate density. The correlation between HVSD and radar reflectivity is improved by this method from a correlation coefficient of 0.81 (standard deviation ± 3.00 dBZ) to 0.94 (standard deviation ± 1.77 dBZ), where for the calculation of the two correlation coefficients, the same number of data points have been used. Nevertheless, lag time correction is more important for the investigation of vertical velocities than for reflectivity.
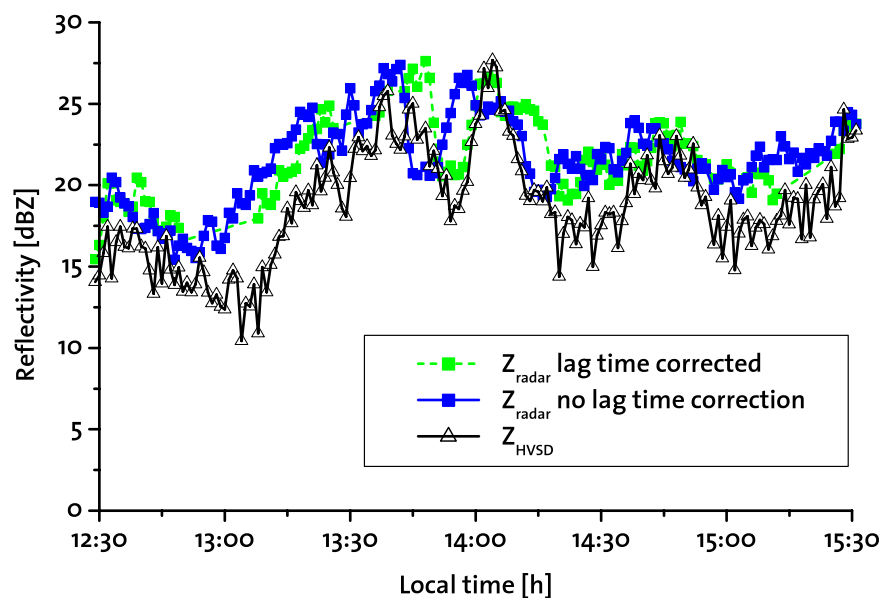
Figure 4.6: *Influence of lag time on reflectivity. For a 3 hour period of Nov. 7, 2002, Z_{HVSD} and Z_{radar} are plotted. The latter is shown with and without lag time correction.*

Lag times and their correlation coefficients can be used for filtering data. They also provide a test for the assumption that if a specific region of the precipitation system moved from above the radar to the upper measuring site, a similar hydrometeor composition can be found in the same height. But this test is restricted by the quality of reflectivity computation. By filtering out data for which a certain maximum lag time (e.g. $< 600\,\mathrm{s}$) is exceeded, the time is reduced in which changes could take place. If, furthermore, only positive lag times are admitted, situations are filtered out, where clouds moved from the mountain towards the radar and the radar would not be on the upwind side. The received lag times deliver combined information about translation direction and velocity. They can be compared with the wind field data retrieved by scanning radars.

4.2 Estimation of vertical wind velocity

As discussed in the introduction (Sec. 1), vertical winds are difficult to measure but play an important role for the microphysics of many precipitation processes. Especially, they have a strong influence on the transport of water vapor (Sec. 2.3.3, p. 33) that effects condensational growth of cloud droplets changing the drop spectra. Thus, also the riming process is directly influenced. A method has been developed to estimate the strength of vertical winds. For this, a combination of in-situ HVSD data (disdrometers could be used in a similar way in rain) and remote sensing radar data is used.

Figure 4.7 explains the basics on which the method for the estimation of vertical winds is based. The radar is measuring the reflectivity and the Doppler spectrum away from ground. The Doppler velocity v_D measured by the radar is defined as the reflectivity weighted first moment of the velocity distribution (Eq. 2.33). If the integral over the resolution volume is replaced by a sum over all n particles j within this volume, v_D becomes

$$v_D = \sum_j^n v_{D,j} = \sum_j^n \frac{Z_j \cdot v_j}{Z} \quad , \tag{4.1}$$

where Z_j is the reflectivity of a single particle and Z the total reflectivity within the volume. For a vertically pointing radar, the contribution to the Doppler velocity by a single particle j is

$$v_{D,j} = v_{T,j} - w \ ; \tag{4.2}$$

this is the sum of the "intrinsic" terminal fall velocity $v_{T,j}$ of the particle j and the vertical wind speed w (updrafts positive sign; v_T positive as particles are falling). Hereby, it is assumed that all particles within the pulse volume are equally influenced by the vertical wind (independent of their size); further, the influence of the finite opening angle of the radar beam is neglected, which makes the measured velocities partly be deviating from the vertical direction.

The HVSD is measuring size distribution and velocity of hydrometeors at ground. With the boundary condition that vertical winds are zero ($w = 0$) at ground, the measured velocity is for a particle j equal to the intrinsic fall velocity: $v_j = v_{T,j}$. The computation of a reflectivity weighted "Doppler" velocity from the HVSD data $v_{D,\text{HVSD}}$ has been discussed in Section 3.8.2 (esp. Eq. 3.4 that is analogous to Eq. 4.2).

Finally, the vertical wind speed for one height can be estimated. For that, the Doppler velocity measured by radar at the equivalent height of the mountain station and in practice averaged over 60 s is subtracted from the Doppler velocity computed from the HVSD data:

$$w = v_{D,\text{HVSD}} - v_{D,\text{radar}} \quad . \tag{4.3}$$
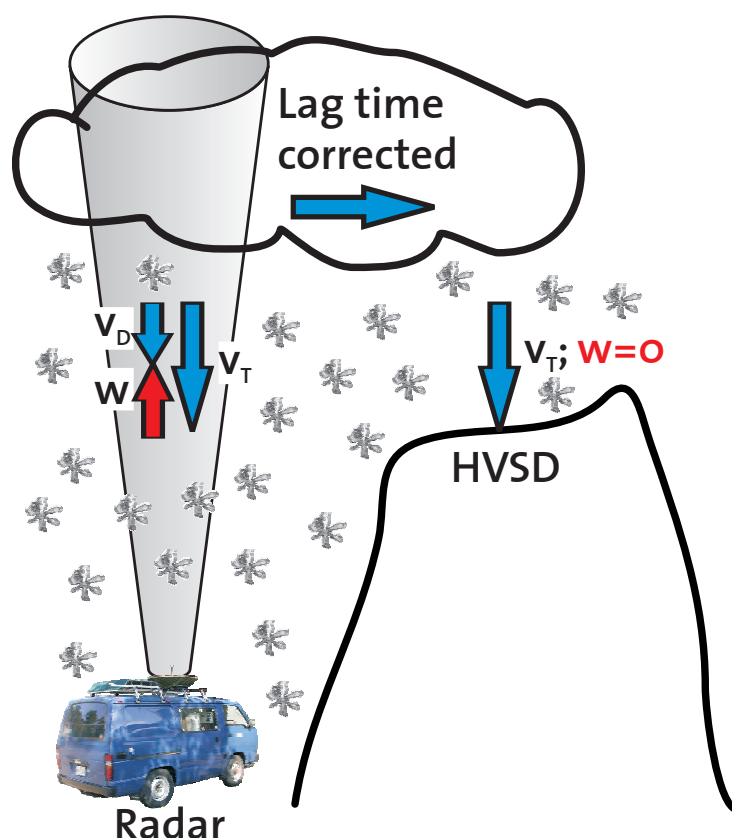
Figure 4.7: *Principle of the method for the estimation of vertical winds.*

Here, the data from the HVSD is taken from a time which is a lag time later than the radar data. Confer the algorithm for evaluation of lag times in Section 4.1.

This method assumes that the distribution of hydrometeors present in the cloud above the radar is not significantly different from the distribution which is a lag time later at the HVSD.

In addition to the estimation of vertical wind speed for a fixed height that has been described above, a second estimate has been introduced that also accounts for the radar Doppler velocities measured at higher altitudes. For that, $v_{D,\mathrm{radar}}$ in Equation 4.3 is substituted by $\langle v_{D,\mathrm{radar}}\rangle_{2\,\mathrm{km}}$. The latter is $v_{D,\mathrm{radar}}$ averaged over a height range (here 2 km) above the height of the upper measurement station. Though the particle fall velocity v_T will in reality not be constant over this height range, $v_{D,\mathrm{HVSD}}$ gives an estimate. Thus, with $\langle v_{D,\mathrm{radar}}\rangle_{2\,\mathrm{km}}$ Equation 4.3 yields an estimate for a mean vertical wind speed for this height range. This approximation will be denoted as $\langle w\rangle_{2\,\mathrm{km}}$.

4.3 Quantification of convection

4.3.1 Definitions

The word convection originates from the Latin verb "convehere" that means "to bring together". There are various definitions of convection. A basic one that is used in physics is closely linked to the Archimedes principle. It states that a buoyant force appears, if parts of a gas or liquid is warmer (or colder) than the other ones. Here, gravitational forces act on the resulting density variations. Emanuel (1994) proposes for meteorological applications a definition restricting the above to relatively small scale circulations caused by the action of gravity upon unstable vertical distributions of mass. The World Meteorological Organization (WMO) defines convection as "organized motions within a layer of air leading to the vertical transport of heat, momentum, etc." (WMO, 1992). By this definition convection is distinguished from turbulence that is defined as "random and continuously changing air motions which are superposed on the mean motion of air" (WMO, 1992). In Section 2.3.1 we introduced the classical definition of stratiform and convective precipitation in the form that convective precipitation is addressed, if the updraft velocity is higher than the fall velocities of the respective particles. This definition is more based on resulting phenomena than on the origin of convection. Neither the WMO definition nor the definition of convective precipitation (Sec. 2.3.1) do explicitly exclude dynamical or orographic reasons of the vertical movement.

The differences between these definitions become negligible for strong convection, in which updraft velocities can reach several tens of meters per second. But in weak convection they can become essential, especially for in stratiform precipitation embedded weak convective cells and if the influences on the microphysics of precipitation are investigated. Further, the threshold between stratiform and convective precipitation, where updraft velocity equals fall velocity, is not without ambiguity. It could be realized by small, slowly falling particles (≈ 0.5 m s^{-1}) and a very weak updraft as well as by faster falling graupel (≈ 3 m s^{-1}) and accordingly stronger updrafts. And there is generally a strong variation of particle fall velocities within a precipitation system.

For the investigations in this thesis, we will use two derived definitions.

CONV I: There is convection, if the updraft velocity is stronger than the particle fall velocity ($w > v_T$, Sec. 2.3.1). This is practical for radar applications because it is – as we will discuss in the following section – equivalent to a negative Doppler velocity ($v_{D,\mathrm{radar}} < 0$). We will use this definition in particular for embedded convective cells.

CONV II: There is convection, if the vertical wind velocity is positive ($w > 0$) that means that there are updrafts present. This is suitable for the following investigation, but different from the WMO definition where downdrafts are equally convective as updrafts. CONV II is compared to CONV I the stronger criterion, and also more suitable for quantification of convection, since it is not dependent on particle fall velocity.

Both definitions (CONV I and II) are independent of the source of vertical winds. In contrast to the first definition, the second is applicable no matter if there are precipitation particles present or not. In Section 2.3 the terms buoyancy (Eq. 2.47) and CAPE (Eq. 2.50) were introduced. These are measures for the potential for convectivity to arise: if it is finally triggered or not. They could be used as a basis for prediction of convection.

4.3.2 Negative Doppler velocity as indicator for (embedded) convection: CONV I

The approach CONV I is to define precipitation as convective, where the upward vertical air motion w (positive if upward) is not only positive but even stronger than the terminal fall velocity v_T (positive if downward). This is closely related to radar meteorology, because a vertically pointing Doppler radar measures the resulting velocity of air motion and fall velocity $v_{D,\mathrm{radar}} = v_T - w$. Here, a downward Doppler velocity has positive sign. Thus, $v_{D,\mathrm{radar}}$ is a direct measure for convective regions.[1]

A high time resolution is required for a non-scanning radar to resolve small and short lived structures of embedded convection (the equivalent would be a high spatial resolution for a scanning radar). The mobile radar by the Institute for Atmospheric and Climate Sciences (IAC***ETH***) has a time resolution of 1 s. The vertical extent E_v of a convective cell can directly be determined from the measurements while the horizontal extent E_h of the cell cannot be deduced as easily because the radar is not scanning and fixed at one point. Consequently, it needs the precipitation system to pass horizontally over the radar. But with a constant advection velocity v_a, a cross section through the precipitation system can be measured. The horizontal extent is then given by

$$E_h = v_a \cdot t_a \quad , \tag{4.4}$$

where t_a is the time an embedded convective cell needs to cross over the radar. Stationary vortices would remain above the radar but have not been observed during any of the later-on shown cases; also the influence of the orography on the pattern of the motion above the radar is negligible for the given setup: Mosimann et al. (1994) cite calculations by Smolarkiewicz and Rotunno (1989) for conditions comparable to the specific setup at Mt. Rigi (Sec. 3.1), and conclude that the influence of this mountain on the vertical air motion can be neglected. This is valid for the given horizontal distance of the radar site from the mountain top, and for winds coming from a sector between north and west. Thus, for cases with positive lag times (Sec. 4.1), orographic influences on the convection measurement can be neglected.

---

[1]In the following images of Doppler velocity negative Doppler velocities are marked in red. Thus, embedded convective cells appear as "red cells".

The translation velocity v_a can be determined by wind field retrieval with scanning radars in single- or dual-Doppler mode, if the setup and positioning requirements are fulfilled (Wüest, 2001). Also some radio soundings measure winds; and additionally, the lag time (Sec. 4.1) is a method to estimate the velocity of advection.

4.3.3 Vertical winds as quantification of convection: CONV II

The velocities of vertical winds according to the second definition CONV II are a direct quantification of convection. For our definition and for the resulting influences on precipitation microphysics it does not matter if the vertical air movement is dynamically induced or caused by density differences. In Section 4.2 we introduced a method for the estimation of vertical wind velocity. This method requires a specific setup and instrumentation (Sec. 3.1). Results for w are most accurate for that height above the radar that corresponds to the height of the upper measurement site. But, additionally an estimate for the mean of the vertical wind speed $\langle w \rangle_{2\,\mathrm{km}}$ over the 2 km above this height can be given (Sec. 4.2).

In stratiform precipitation from nimbostratus clouds, there is a steady updraft of a couple of tens of cm s^{-1} (Houze, 1993). Such a steady updraft can be identified or could, if necessary, be separated by the vertical wind estimation method.

4.3.4 Analysis of the convection index defined by Mosimann (1995)

Based on radar data only, Mosimann (1995) chose a different property of convective precipitation for classification: the variability. The author cites Liljequist and Cehak (1984) that convective precipitation exhibits turbulence and convective cells, and concludes that for a vertically pointing Doppler radar these features lead to a strong variability of the mean Doppler velocity with time. Mosimann defines a "convection index"

$$\kappa = \frac{|v_D - \bar{v}_D|}{\bar{v}_D} \quad , \tag{4.5}$$

where $\bar{v}_D$

$$\bar{v}_D = \frac{1}{\Delta t} \int_{t-\Delta t/2}^{t+\Delta t/2} v_D \, dt \Bigg|_{z=h} \tag{4.6}$$

is a running average over the Doppler velocity at a constant height h over (in his case) three data points corresponding to a 15 min interval. The numerator $|v_D - \bar{v}_D|$ is a measure for the deviation of the Doppler velocity v_D from the long time average $\bar{v}_D$; this is then normalized by $\bar{v}_D$ to yield κ. Two difficulties are obvious: for $\bar{v}_D = 0$, there is a singularity, and for $\bar{v}_D < 0$, which is in a way more convective than small positive values, κ becomes negative. Thus, if κ is averaged over height for, e.g., following the growth history of a particle, positive and negative values may cancel. Mosimann (1995) defined the small range $0 < \kappa < 0.2$ for strictly stratiform precipitation, where he could apply a remote sensing technique for the identification of riming.

In order to take a closer look at the definition of κ and to see its relation to the above definitions of convection (CONV I and II), we split each of the two contributions to the Doppler velocity $v_D = v_T - w$ into two parts:

$$v_T = \bar{v}_T + v'_T \quad , \tag{4.7}$$
$$w = \bar{w} + w' \quad . \tag{4.8}$$

One part corresponds to the long time averages $\bar{v}_T$ and $\bar{w}$, and the second part to fluctuations v'_T and w'. The latter fluctuations may come from convection as well as from turbulence. Thus we can re-write Equation 4.5 as

$$\kappa = \frac{|v_D - \bar{v}_D|}{\bar{v}_D} = \frac{\left| \bar{v}_T + v'_T - (\bar{w} + w') - (\bar{v}_T - \bar{w}) \right|}{\bar{v}_T - \bar{w}} = \frac{|v'_T - w'|}{\bar{v}_T - \bar{w}} \quad . \tag{4.9}$$

Now it makes sense to distinguish three cases:

Case I: $\kappa < 0$

It can easily be seen that $\kappa < 0$ is equivalent to $\bar{w} > \bar{v}_T$ and to $\bar{v}_D < 0$, respectively. Thus, in this case even the long term average is convective in the sense of CONV I and CONV II.

Case II: $\kappa > 0$ **and** $v_D < \bar{v}_D$ **- The updraft branch.**

$\kappa > 0$ means first of all that $\bar{v}_D > 0$. If we split also the Doppler velocity

$$v_D = \bar{v}_D + v'_D \tag{4.10}$$

into a mean $\bar{v}_D$ and a fluctuating v'_D part, then $v_D < \bar{v}_D$ is equivalent to $v'_D < 0$ as well as to the

argument of the absolute value $|v_D - \bar{v}_D|$ being negative. Thus, $-v_D + \bar{v}_D = \kappa \cdot \bar{v}_D$ which can be converted to

$$v_D = (1 - \kappa) \cdot \bar{v}_D \quad . \tag{4.11}$$

With $\kappa > 1$ the current value of the Doppler velocity becomes negative $v_D < 0$. This is also clearly convective in both senses. For $\kappa < 1$ approaching 1, the state comes closer to being convective. Thus, increasing κ signifies becoming more convective. Figure 4.8 shows a parameter plot of v_D versus $\bar{v}_D$ for different values of κ.

What happens with the singularity in the limit $\bar{v}_D$ approaching zero? We can split up $\bar{v}_D - v_D$ as in Equation 4.9 into $w' - v_T'$. Resolving for the part of the vertical wind w' deviating from the average we receive

$$w' = \kappa \cdot \bar{v}_D + v_T' \quad . \tag{4.12}$$

Thus, κ is also a measure of how much stronger, in units of the average Doppler velocity, the vertical wind deviates from the average than the particle fall velocity does. It is not expected that the terminal fall velocity varies strongly in snow; thus v_T' will be small. Because κ and $\bar{v}_D$ are in this case II both positive, and a high κ means a strong upward deviation of the vertical wind, thus $v_D < \bar{v}_D$ could be called the "updraft branch" of κ. But if $\bar{v}_D$ comes close to zero κ can become very large without any significant meaning. Therefore, it would make sense to restrict κ to a maximum value.

Case III: $\kappa > 0$ and $v_D > \bar{v}_D$ - The downdraft branch.

If $v_D > \bar{v}_D$, the argument of the absolute value $|v_D - \bar{v}_D|$ is positive and $v_D' > 0$, resp. Thus, $v_D - \bar{v}_D = \kappa \cdot \bar{v}_D$, or

$$v_D = (\kappa + 1) \cdot \bar{v}_D \quad . \tag{4.13}$$

The instantaneous value of the Doppler velocity deviates by a factor $\kappa + 1$ from its average value. For instance, for $\kappa = 1$, $v_D = 2 \cdot \bar{v}_D$.

For the case III, the variable part of the vertical wind becomes

$$w' = v_T' - \kappa \cdot \bar{v}_D \quad . \tag{4.14}$$

If the term $\kappa \cdot \bar{v}_D$ is large and v_T' small, w' becomes negative. Thus, $v_D > \bar{v}_D$ could be called the "downdraft branch" of κ (Fig. 4.8).
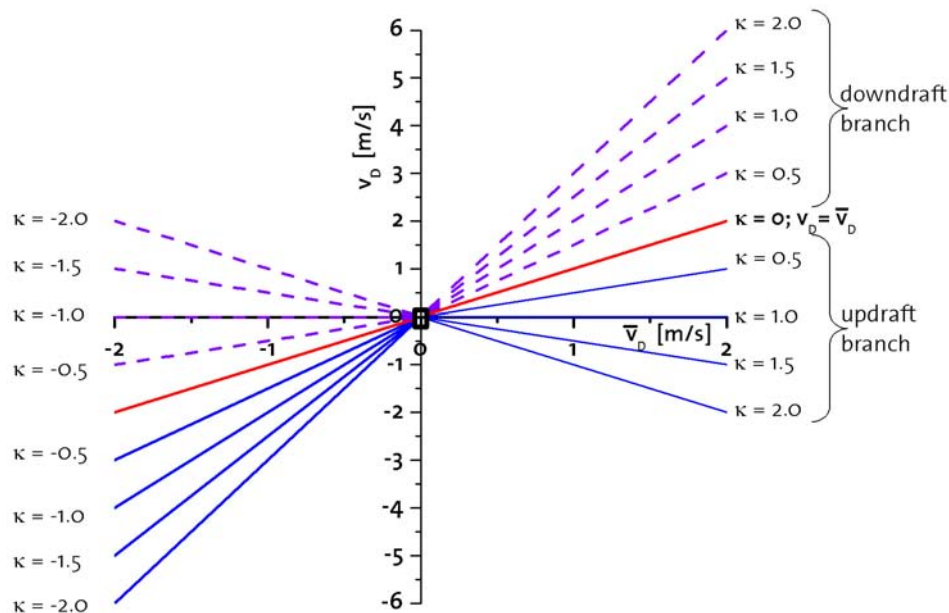
Figure 4.8: *Analysis of the "convection index" κ defined by Mosimann (1995).*

This analysis shows that κ is not a clear cut criterion: It contains as a main basis the also not well-defined variability, and otherwise a mixture of turbulence and convection. It has elements of turbulence because the "updraft" and "downdraft branches" describe the variable w' and not the mean part of the vertical wind and this is related to the WMO definition of turbulence (Sec. 4.3.1). But because w' is here a function of the average Doppler velocity v_D, κ also contains elements of the average part and is thus also related to convection. Besides, the case I is clearly convective in both senses of the definitions CONV I and II. Consequently, the above (Sec. 4.3.1) mentioned definition by Mosimann (1995) that the small range $0 < \kappa < 0.2$ is strictly stratiform precipitation is neither identical to the classical definition of stratiform precipitation (Sec. 2.3.1) nor to CONV I, respectively. If w' is of the same order as v_T', $\bar{w}$ can be very large (and thus convective) and still yield a small value of κ, especially also between 0 and 0.2.

In the next section a quantity called Doppler delta Δ_D will be defined that is related to κ, but contains predominately the turbulent aspects.

4.3.5 The Doppler delta as a measure of turbulence

We define the Doppler delta Δ_D as

$$\Delta_D := \bar{v}_D - v_D \quad . \tag{4.15}$$

This is – except for the different sign and without the absolute value – part of the nominator of the definition of κ (Eq. 4.5). $\bar{v}_D$ is averaged over the time Δt defined by Equation 4.6. Again, we will split v_D as well as $\bar{v}_D$ into vertical wind $w = \bar{w} + w'$ and particle fall velocity $v_T = \bar{v}_T + v_T'$ (cf. Eq. 4.8 and 4.7). Now, Equation 4.15 can be rewritten and yields

$$\Delta_D := \bar{v}_D - v_D = \bar{v}_T - \bar{w} - (\bar{v}_T + v_T' - (\bar{w} + w')) = w' - v_T' \quad . \tag{4.16}$$

Resolving for w', this gives

$$w' = \Delta_D + v_T' \quad . \tag{4.17}$$

If $\left| v_T' \right| \ll \left| w' \right|$, we can approximate Equation 4.17 to read

$$w' \approx \Delta_D \quad . \tag{4.18}$$

For snow, $\left| v_T' \right|$ is usually small and below 1 m s^{-1}. Consequently, for large values of Δ_D (positive or negative) will be $\left| v_T' \right| \ll \left| w' \right|$. Thus, then the Doppler delta Δ_D is a measure of the deviation of the vertical wind from its mean value and thus, with the definition in Section 4.3.1, a measure of turbulence especially if $|\Delta_D| > 1$. Especially turbulent structures of different scales will become visible in a plot of Δ_D for snow, if the averaging time Δt for $\bar{v}_D$ is varied.

Chapter 5

Results of case studies and discussion

In winter 2002/2003, the field campaign RAMS (**R**iming, **A**ggregation, and **M**ass of **S**now) took place. In the period from November until April, measurements were made at occasions when based on forecasts a frontal system or a meso-scale blocking condition was expected. These systems should preferably approach from northerly or westerly direction with relatively small wind velocities and significant amounts of snow at heights below the upper measuring site at Mt. Rigi. The setup is described in detail in Section 3.1. We will present here the case of November 7, 2002, in detail and the other cases only in summarized form. A discussion of these results but also of general aspects of the methods is done in parallel sections.

5.1   Case of Nov. 7: Synoptic overview

From the case studies of the winter season 2002/2003 November 7 has been chosen as an example for detailed analysis. At that day, the weather conditions in the area of Lake Lucern were characterized by an occluded frontal system. The clouds of this occlusion can be seen on the infrared Meteosat satellite image from 8:30 LT (Fig. 5.1). Mt. Rigi is marked by a red cross.

The precipitation event, and thus the intensive observation period, was an approximately 7.5 hour period between 8:30 and 15:50 LT. Except for short time intervals, as for example from 12:30 till 13:00 LT, the air pressure was steadily rising. At the lower site it started from 957.3 hPa and reached 960.2 hPa at 15:50 LT (Fig. 5.2a). The temperature at the bottom station rose from 4.2 °C to 6.2 °C, and fell again for the last half hour back to 5 °C. Whereas at the top station, the temperature stayed constant at -1.5 °C between 9:00 and 13:30 LT. Then it fell continuously to -2.5 °C (cf. Fig. 5.2b). The dew point difference at the lower station ranged between 3.5 and 1.5 °C. The disdrometer measured a total amount of rain of 4.8 mm, and the rain gauge of 4.4 mm (Fig. 5.2c). This corresponds to a relatively low average rain rate of 0.65 mm h^{-1} and
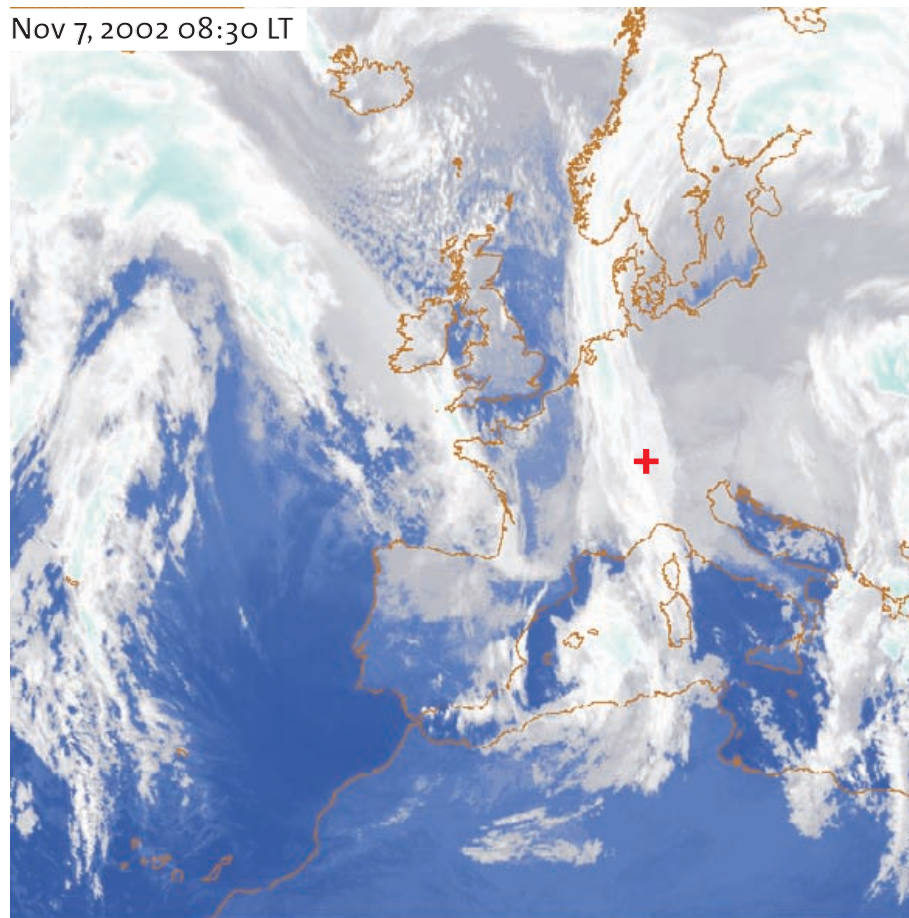
Figure 5.1: *Occluded frontal system in the infrared Meteosat satellite image from Nov. 7, 2002, 8:30 LT. The area of Mt. Rigi is marked by a red cross.*

0.60 mm h^{-1}, resp. The prevailing rain rates based on 30 s periods are shown in Figure (5.2d). The most intense periods were at 9:30 till 10:00 LT and at 13:30 till 14:15 LT. Wind velocity and direction (Fig. 5.3) were measured on the roof of the radar van. The winds close to the ground were generally weak with a slight increase around 9:30 LT and after 15:00 LT and with a very weak period between 12:00 and 14:00 LT. The data has to be taken with care, as it was measured in a height of only 2 m and only about 5 m away from a building. The measured winds were mainly from a south-westerly direction. Deviating wind directions were present at higher elevations as derived from the single-Doppler wind fields measured by the scanning C-Band radar at ETH-Hönggerberg (cf. Sec. 3.3): The wind direction over Lake Lucern at a height of Mt. Rigi was from west and changed to north-west ($\approx 300°$) by about 11:00 LT (Fig. 5.4).

(a) Pressure at lower measurement site.

(b) Temperatures and dew point at lower and upper site.
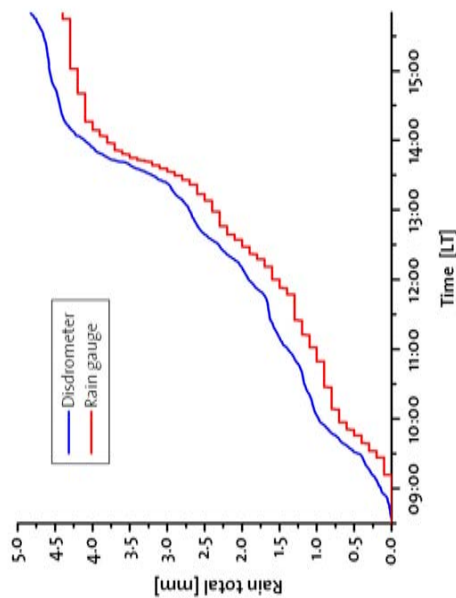
(c) Rain total at lower measurement site based on disdrometer and rain gauge data.

(d) Disdrometer rain rates. Based on 30 s periods.

Figure 5.2: *Part I of overview over weather conditions of the period 8:30 till 15:50 LT on Nov. 7, 2002.*

(a) Wind direction.
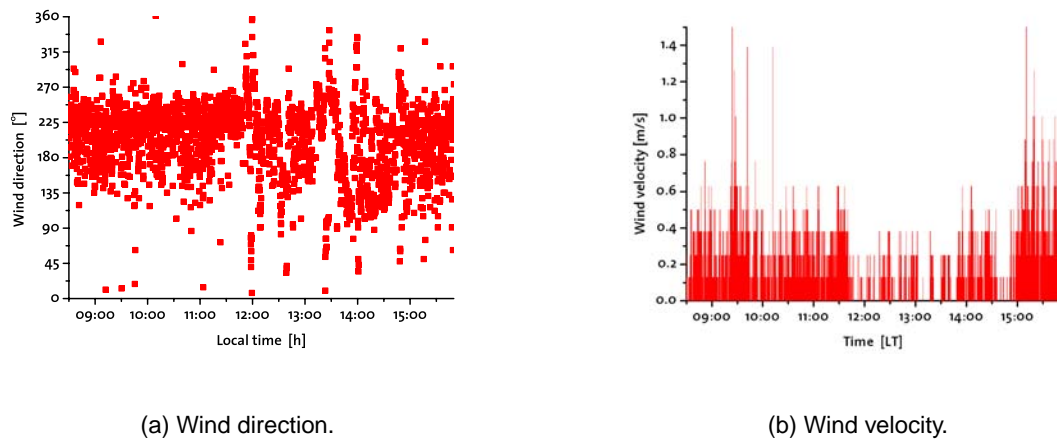
(b) Wind velocity.

Figure 5.3: *Part II of overview over weather data for the period 8:30 till 15:50 LT on Nov. 7, 2002: Wind direction and velocity measured on the radar van. These measurements were partly influenced by a building.*

(a) Wind direction.
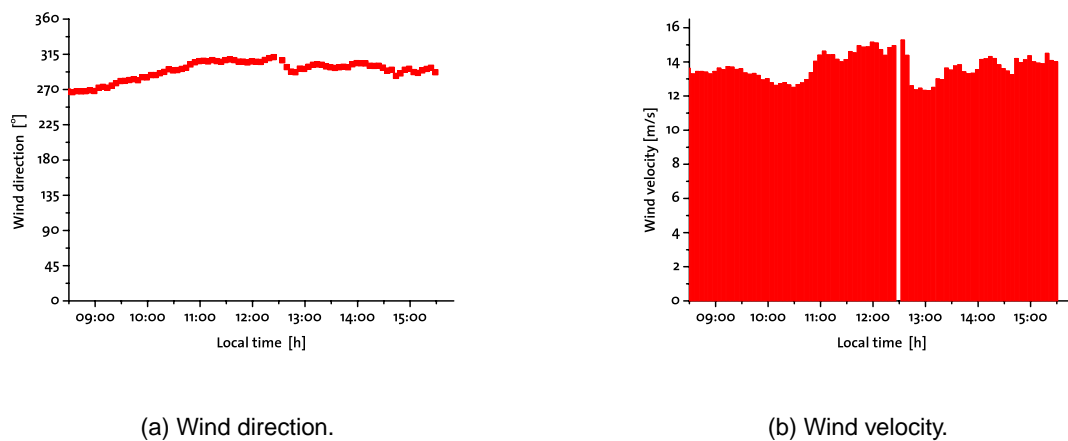
(b) Wind velocity.

Figure 5.4: *Part III of overview over weather data for the period 8:30 till 15:50 LT on Nov. 7, 2002: Wind direction and velocity based on the single Doppler wind field of the ETH C-band radar.*

Figure 5.5 displays the data of the sounding performed at $\approx$ 14:00 LT launched from the lower measurement site. For the whole height range that is relevant for the radar observations of this study, the air was saturated or close to saturation with a temperature gradient of $\approx$ -0.55°C per 100 m: this corresponds to a nearly saturated mixed layer. An additional sounding that includes wind measurement was made by the Swiss military weather service. It was performed at 13:00 LT in the area of Merlischachen, which is from the lower measurement site across Lake Lucern (see map in Fig. 3.2) and about 2 km apart. This sounding detected the 850 hPa pressure level at 1424 m above sea level. At this height, temperature was -1.1 °C with a dew point difference of 0.6 °C, and a wind speed of 13 m s^{-1} from 265° was measured. The wind velocity was constant up to a height of about 4.5 km, but there was wind shear and the wind direction in the upper part of this layer was $\approx 310°$.
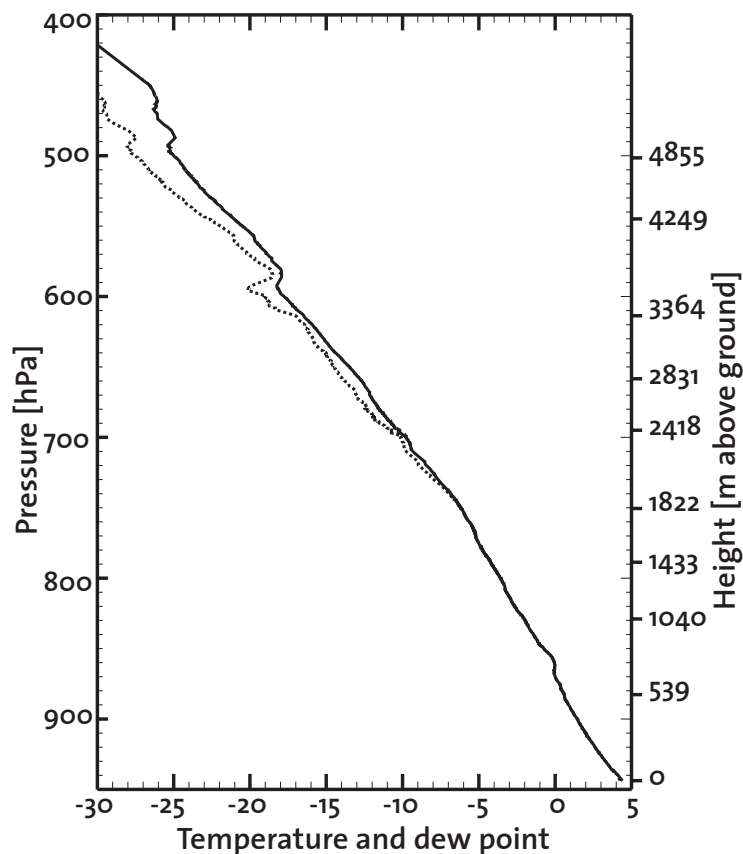
Figure 5.5: *Sounding started at $\approx$14:00 LT on Nov. 7 directly besides the radar van.*

Riming

The determination of the degree of riming is based on Formvar samples (cf. Sec. 3.7) which were taken at the upper station in 10 min intervals. The linear average of the degree of riming of different crystal types on a single Formvar sample is further referred to as the degree of riming of a Formvar sample. It is shown together with the spread of riming of different crystal types within one Formvar sample in Figure 5.6. The average degree of riming of the different samples was for a first period between 8:30 and 11:00 LT moderately rimed RIM = 1.9 ± 0.4. Then it increased and reached an average of RIM = 3.3 ± 0.3, which is more than densely rimed, for the period 12:15 till 15:50 LT.
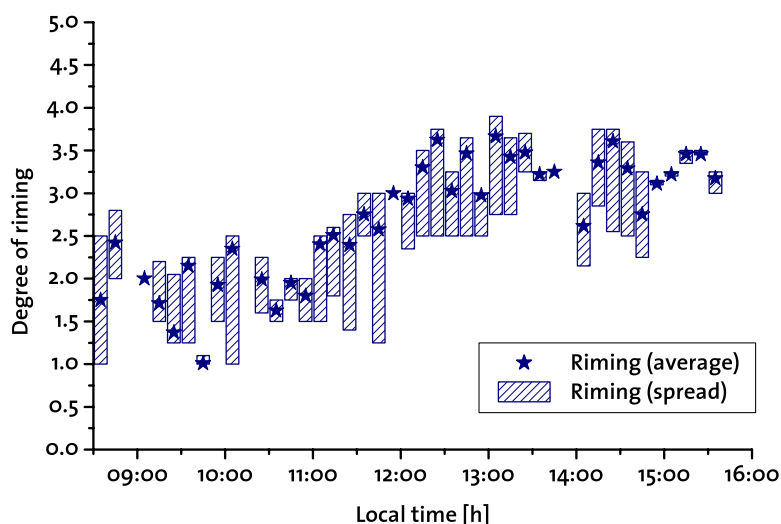
Figure 5.6: *Degree of riming for case November 7, 2002.*

Data of the X-band radar

The character of precipitation can be seen on the radar images. Figure 5.7 shows the height-time-indicator (HTI) of reflectivity (a) and of the Doppler velocity (b) for the Nov. 7 case. In the reflectivity HTI, a bright band with varying strength can be seen. It is approximately 700 m above the radar, a bit lower in the beginning and at the end of this event. Thus, it shows a height variation fitting to the development of temperature at the lower site (Fig. 5.2b). Because of the presence of a bright band, the whole event could be classified as stratiform by this simple criterion (Sec. 2.3.1). But, in the Doppler velocity HTI (Fig. 5.7b) an increasing number and size of regions with negative Doppler velocity can be seen. These are embedded convective cells (Sec. 4.3.2).
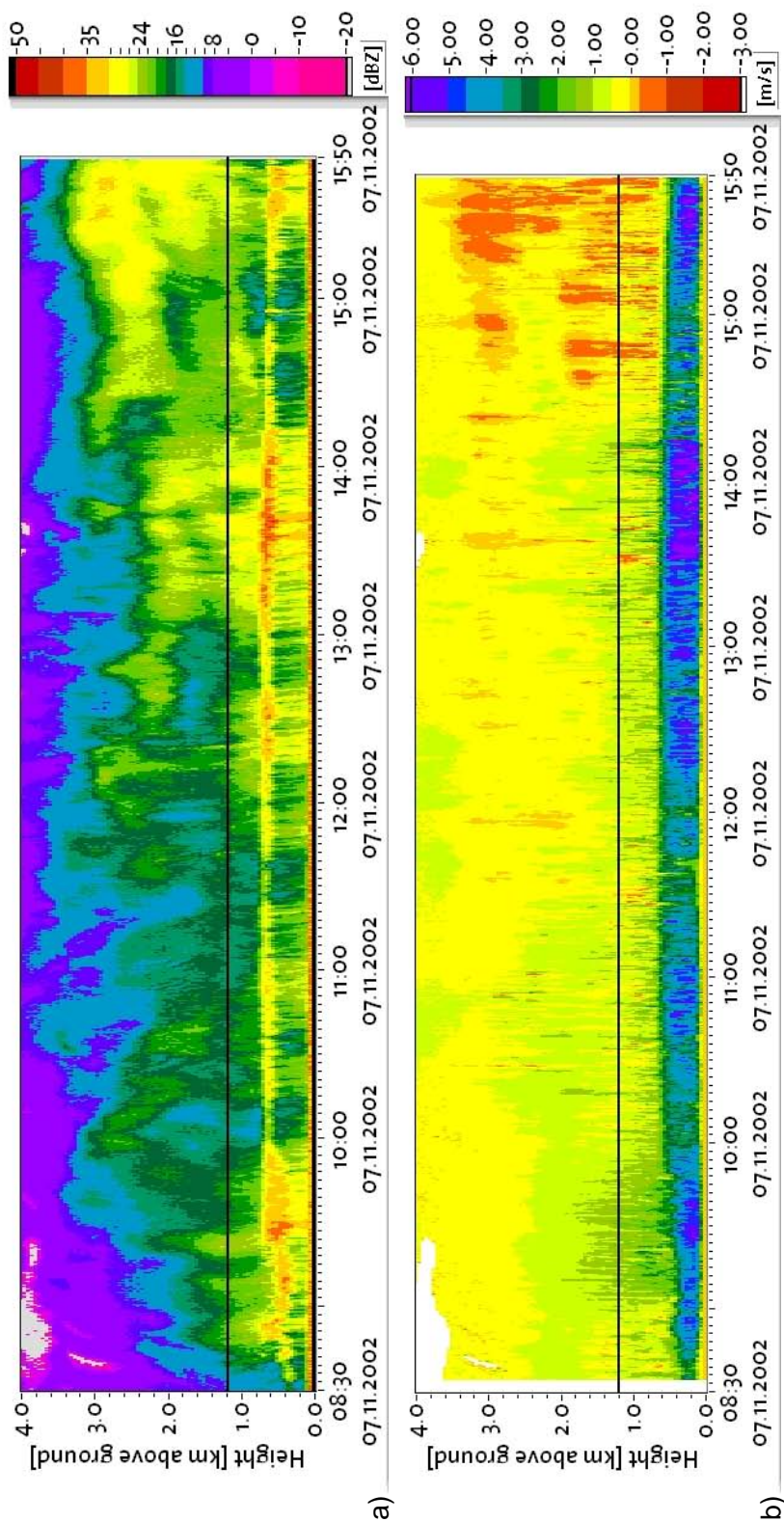
Figure 5.7: *Height time diagram (HTI) of reflectivity (a) and Doppler velocity (b) for the period between 8:30 and 15:50 LT on Nov. 7, 2002. The black line marks the height of the upper measurement site.*

Doppler velocity determined from HVSD data

Equation 3.4 was used to calculate $v_{D,\mathrm{HVSD}}$ for the case Nov. 7. Again, three different mass-size relations of the form given by Equation 2.11 were used to test the influence of a specific choice on the results: $a_m = 0.059$ and $b_m = 2.1$ for graupel-like snow of intermediate density, $a_m = 0.013$ and $b_m = 1.74$ corresponding to stellar crystals with rimed spatial branches, and $a_m = 0.059$ and $b_m = 3.31$ for hexagonal plates (cf. Sec 2.1.5). But, as we will discuss in the following section, the choice of a value for a_m has no influence on $v_{D,\mathrm{HVSD}}$. Only the exponents b_m has an influence on the results. The average values of $v_{D,\mathrm{HVSD}}$ over the whole event were 1.51, 1.54 and 1.59 m s^{-1} and showed thus only negligible differences. Figure 5.8 shows the development of $v_{D,\mathrm{HVSD}}$ for $b_m = 2.1$. The spread of the data in the plot is ≈ 0.2 m s^{-1}.
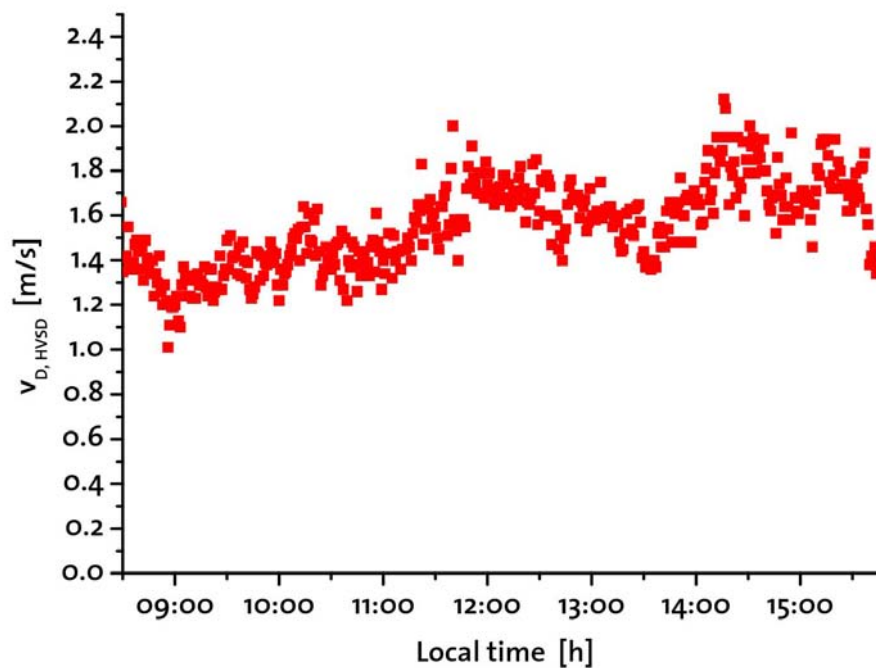
Figure 5.8: $v_{D,\mathrm{HVSD}}$ in [ms^{-1}] versus local time [h] for case Nov. 7. Computed with $b_m = 2.1$.

5.2   Discussion of HVSD data: reflectivity and velocity

In Section 3.8.2 the algorithms are presented that are used for the calculation of reflectivity and Doppler velocity out of HVSD data. Hereby, it is a basic question which specific mass-diameter relation is selected, i.e. which parameters a_m and b_m are chosen (Eq. 2.11), and with which of the typical dimensions derived from the HVSD (Fig. 3.14, examples in Sec. 4.1.2) reflectivity is calculated. Mass-diameter relations vary within the literature, and depend on habit and degree of riming of ice particles (Tab. 2.3). Moreover, because of changes in hydrometeor composition, mass-size relations are changing continuously. Thus, parameters are difficult to determine from measurements. Furthermore, mass-size relations might differ within the measured volume. As long as these uncertainties remain, it is of limited use to apply more accurate but also more complicate algorithms for calculation of reflectivities as, for example, applying as a first step Mie (Sec. 2.2.4) instead of Rayleigh scattering theory.

In this thesis, reflectivity from HVSD data is used as basis for cross correlation analysis (Sec. 4.1). Because the coefficients of linear correlation are unchanged under linear transformation of the data series (App. B), the actual value of parameter a_m of the mass-size relation has no influence on the correlation coefficients: In Equation 3.3 $a_m{}^2$ is outside the sum and thus contributes only with a constant factor to reflectivity. For the evaluation of cases, correlation is applied to values not in linear but in logarithmic (dBZ) units, to avoid an over-emphasis of high reflectivities. Also then a_m yields only a linear offset to reflectivity of the form $10 \log 2a_m$, and thus it does not contribute to the correlation coefficients. In order to minimize the influence of the selection of a specific mass-size relations, there are one intermediate and two extreme values for the exponent b_m included in the algorithm for the computation of lag times (Sec. 4.1).

Also the computation of Doppler velocity $v_{D,\mathrm{HVSD}}$ (Eq. 3.4) is independent of a_m. Due to normalization with the total reflectivity Z, the factor a_m^2 cancels in numerator and de-numerator term: Only the shape of the Doppler spectrum is relevant and not its scaling. As seen in Section 5.1 on page 78, also the influence of a choice of b_m is marginal. The spread of data in the plot for the case Nov. 7 that is ≈ 0.2 m s^{-1}, can be taken as an approximate maximal error on the velocity computation caused by splitting the HVSD data into one minute intervals.

Errors in fall velocity measurement influence the extrapolation from the area-based data measured by the HVSD to volume data (Sec. 3.8.2). If fall velocities are measured too small, the corresponding particles represent a smaller volume and the reflectivity, extrapolated to a cubic meter, increases.

Horizontal winds can produce errors on the measurement of fall velocity by HVSD. In case they transport an ice particle which passes the upper line camera to such an extent that it misses the lower line camera, there might erroneously another ice particle be selected by the matching algorithm or, if not, there is no corresponding lower image. Consequently in the latter case, no

velocity can be measured and shapes can not be corrected. As long as only a small percentage of the ice particles remains unmatched, the error that is produced by taking the median of velocity of the matched particles of the same diameter bin should be small (cf. Sec. 3.8.2). The data algorithms of the HVSD provide an additional parameter which quantifies the quality of the matching process. The choice of a threshold has to balance between taking only the velocity distribution of a small high quality data part as representative for the rest and including too many low quality matches. For more details about the HVSD see Schefold (2004) and Barthazy et al. (2004).

5.3   Case Nov. 7: Lag time correction and filter rules

The plot of the lag times for the case Nov. 7, has already been shown in Figure 4.5. The correction of lag times is important for comparison of data between the lower and the upper site which are sensitive on exact timing. One example for this is the estimation of vertical winds. But, lag time is, as mentioned in Section 4.1.3, a possibility for filtering data and improving its quality. Only lag times between 0 and 600 s and correlation coefficients above 0.5 have been accepted. Another filter rule was that rain rates at the lower site had to be larger than 0.1 mm h^{-1} to ensure ongoing precipitation. For analysis, where Formvar samples are included, it makes sense to request as a last filter rule, namely that the temperature at the upper site should be below -1 °C. This is because for higher temperatures the quality of Formvar samples could not always be ensured. If the temperature of the glass plate for the Formvar sample were too high, artifacts as, for example, melting of the outer layer of ice particles and thus eventually of accreted cloud droplets take place. These filter rules have, besides for the case of November 7, later on also been applied to the remaining cases.

5.4   Discussion of the lag time correction

As discussed in Section 4.1.1, some assumptions have to be made for the comparison of measurement data originating from instruments of the two different measurement sites. Assuming that the composition of hydrometeors with respect to distribution of habits, sizes, and terminal fall velocities are identical at both places in the same height, would mean to assume complete stratification and uniform layering of precipitation. There might be cases, where this assumption holds. But especially for the analysis of embedded convection, this can not generally taken to be true or would even contradict the definition of embedded convective cells (Sec. 2.3.1). In contrast, a less strict assumption is to say that a given horizontal region of the precipitation sys-

tem keeps for a relatively short period of time a similar vertical composition. The method of lag time correction offers especially in its ameliorated form, where lag times are computed for every minute of measurement (Sec. 4.1.3), the possibility to correct for the time needed for horizontal advection. While neglecting so far influences of orography on vertical motion, a consideration of geometry (cf. sketch in Fig. 5.9) makes clear that only one distinct direction of advection leads to a translation of the part of the region measured by the radar (above the lower site) directly to the upper site. This direction is given by the direct line between lower and upper site that for the given setup is 280° (Sec. 3.1, Fig. 3.2). For deviating advection angles

$$\alpha_a = 280° - \alpha_{\text{wind}} \quad , \tag{5.1}$$

where α_{wind} is the actual wind direction, a horizontal similarity of hydrometeor composition perpendicular to the direction of movement has to be given. For embedded convection this means, point C (Fig. 5.9) should be so close to the lower site be in the same or at least in a similar cell, that is in a comparable position within the moving front.
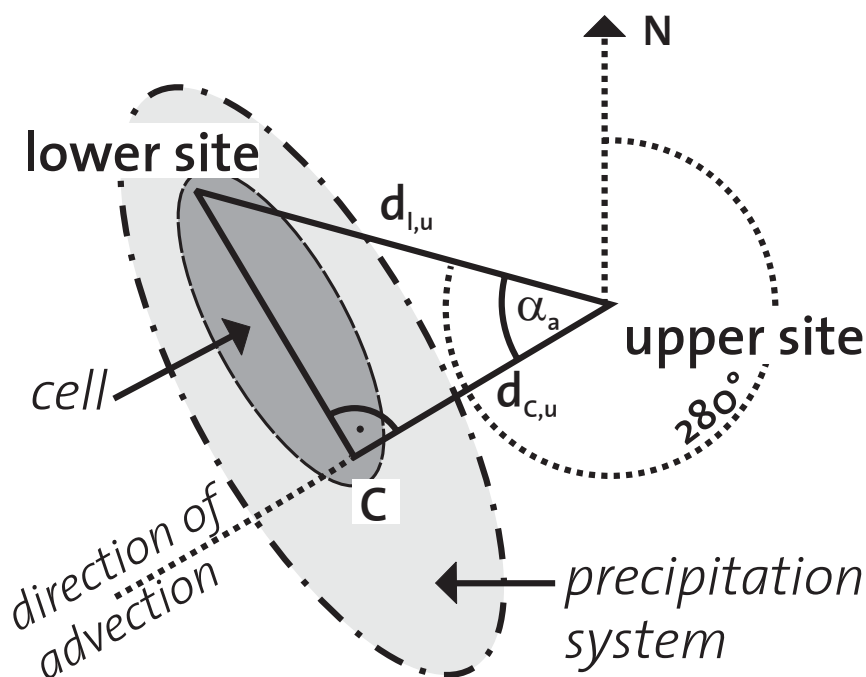
Figure 5.9: *Sketch of the geometry of the measurement area with respect to advection.*

Consequently, the lag time gives only an approximate value for the time for the advection of the precipitation system for the distance $d_{l,u}$ from above the lower site to the upper site. More precisely, it is representative for the distance $d_{C,u}$ between point C and the upper site, where

$$d_{C,u} = \cos \alpha_a \cdot d_{l,u} \quad . \tag{5.2}$$

Thus, high values of α_a should be excluded. However, there are no direct measurements of wind direction that would be representative for the whole range between lower and upper site, and thus α_a is unfortunately not available. Even if α_a is taken from the single Doppler wind field of the scanning radar located at IAC*ETH*, it depends on the situation which values of α_a would have to be taken as an upper limit. Instead, again the lag time correction method offers a solution. By only accepting high values of correlation coefficients (cf. Sec. 4.1.3) data can be filtered. The correlation coefficients give a measure for the assumption of small changes in hydrometeor size composition. But, besides the generally problematic interpretation of correlation coefficients, and other possible errors in the calculation of reflectivity for the HVSD, there is the difficulty of choosing the correct mass-size relation as discussed in the previous Section 5.2. In order to minimize the influence of the selection of a specific mass-size relations, three different values for the exponent b_m have been chosen (cf. Sec. 4.1).

Additional filtering has been done by only accepting lag times between 0 and 600 s. Positive lag times limit the cases to those where the precipitation systems arrive at the lower site before they reach the upper site. The upper limit minimizes the time for changes of hydrometeor composition to take place. These strong filtering criteria reduce the amount of data but is important for its quality.

Small advection angles α_a were postulated for a relatively direct movement of a precipitation system from above the lower to the upper measurement site. This coincides with the requirement of Section 4.3.3 that winds come from a sector between west and north-west. Then, there is no direct orographic influence of the mountain on the flow above the lower measurement site (Sec. 4.3.2). If the main flow is around the mountain, it is assumed that advection does not lead to a significant disturbance of the layers over the lower site which are above the height level of the upper site. For situations with a flow over the mountain, there will be some influence by lifting of hydrometeors, which is difficult to quantify. But the opposing movement of the falling hydrometeors reduces this influence.

As a test for the values of the received lag times, soundings with wind measurements can be used. A sounding by the Swiss military weather service (Sec. 5.1) started at 13:00 LT on November 7, 2002. It measured at a height of 1424 m a wind velocity of 13 m s^{-1} with a direction of 265°. This can be converted into an expected lag time $t_{\text{lag,exp}}$ by combining the Equations 5.1 and 5.2. The distance $d_{C,u}$ (Fig. 5.9) is covered with the advection velocity v_a. Thus, $t_{\text{lag,exp}}$ is the time needed for this distance given by Equation 5.2, and we can write

$$t_{\text{lag,exp}} = \frac{d_{l,u} \cdot \cos\left(280^\circ - \alpha_{\text{wind}}\right)}{v_a} \quad . \tag{5.3}$$

With $d_{l,u}$ = 3650 m this yields $t_{\text{lag,exp}}$ = 270 s. The lag times determined by the cross correlation method are 360 s at 13:10 LT decreasing to 250 s at 13:20 LT. Thus, both methods result in a same order of magnitude. Nevertheless, lag times are probably not more accurate than by ap-

proximately 100 s. But further the resulting lag times show for the case of November 7, 2002, (Fig 4.5) some – presumably artificial – sudden jumps and otherwise mostly smooth variations. One idea is that this could be caused by sudden changes in wind direction. To investigate this, lag times have been compared with the single Doppler wind fields (Fig. 5.4). Unfortunately no dual Doppler wind fields were available for which measurement errors are smaller. Errors for single Doppler wind fields are calculated in Wüest et al. (1999). Especially, because on this day the wind direction in the area of Lake Lucern is almost perpendicular to the direction of the radar beam (cf. map in Fig. 3.2), which is unfavorable for single Doppler analysis, larger errors can occur. Besides the orographic situation is complicated. These errors can add up to approximately 5 m s^{-1}(Personal communication by Marc Wüest, IAC**ETH**, ETH-Zürich.). With the single Doppler analysis, of which the detailed results are not shown here, most lag times of the case are reasonable, but still this can not explain the sudden jumps to high lag times of about 800 s. To give a possible explanation, we perform a thought experiment. Taking the case that there is a short graupel shower that finishes shortly after it passed over the lower measurement site, and does not reach the upper station. Then the hydrometeor composition at the upper station will look more similar – and will yield in higher correlation coefficients – to a region which had been much earlier or much later at the lower station. This would result in unrealistic, very high positive or much lower and maybe negative lag times. But such lag times below 0 s or above 600 s are filtered out by the lag time filtering method (Sec. 4.1). Thus, the filtering via lag times and their correlation coefficients performs another important task. It improves for the remaining data the validity of the assumption that lag times are short compared to the life time of a region within a precipitation system (Sec. 4.1.1).

5.5 Case Nov. 7: Vertical wind velocity and riming

The method for the estimation of vertical winds has been described in Section 4.2. Figure 5.10 contains the riming information (Fig. 5.6 re-plotted) together with the estimates of vertical wind velocity. The Doppler velocities from HVSD data $v_{D,\mathrm{HVSD}}$ originate from the times where the filtered Formvar samples are taken. The measured radar velocities $v_{D,\mathrm{radar}}$ are also averaged over one minute, shifted by the calculated lag times. The plot contains two different graphs: Firstly, there is w with $v_{D,\mathrm{radar}}$ only taken at the height 1.2 km above ground, which is equivalent to the height of the upper site. Here, w ranges between -0.03 and 2.29 m s^{-1}. Additionally, the vertical wind velocity $\langle w \rangle_{2\,\mathrm{km}}$ has been calculated, i.e. with $v_{D,\mathrm{radar}}$ averaged over the 2 km between the height of the upper site and 3.2 km above ground. $\langle w \rangle_{2\,\mathrm{km}}$ lays between 0.55 and 2.05 m s^{-1}.
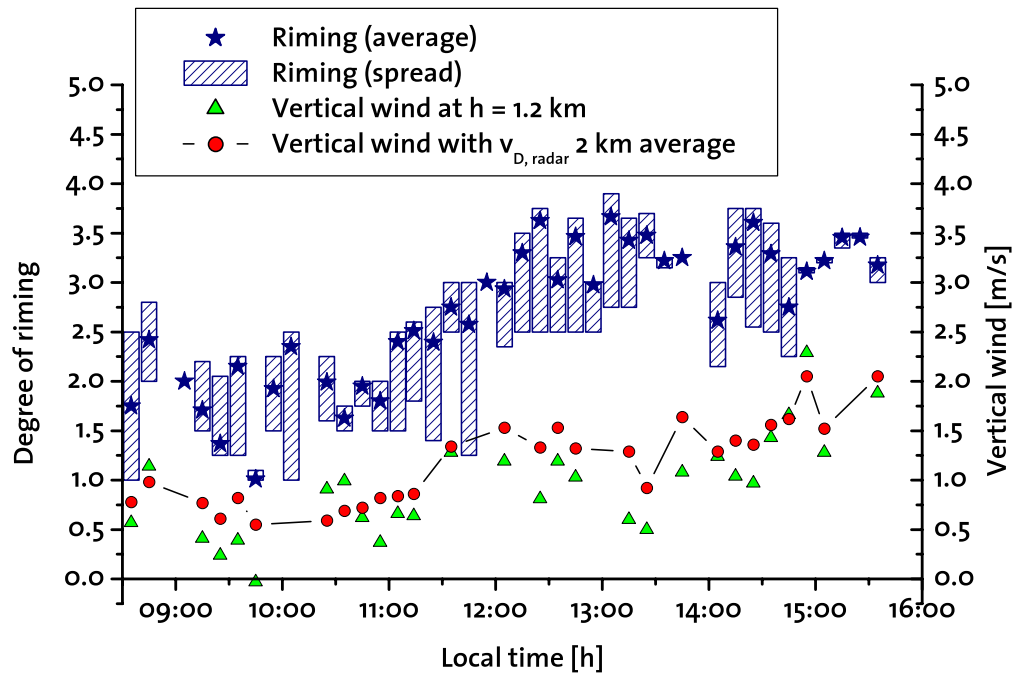
Figure 5.10: *Development of riming (taken from Fig. 5.6) and vertical winds (right ordinate, in m s^{-1}). For the determination of vertical winds, the radar Doppler velocity has been once taken at the height 1.2 km above ground only (green triangles). For the second data set $\langle w \rangle_{2\,\mathrm{km}}$, $v_{D,\mathrm{radar}}$ was averaged over 2 km between the height of the upper site and 3.2 km above ground (red dots).*

Both wind velocities increase at about 11:30 LT. $\langle w \rangle_{2\,\mathrm{km}}$ stays high and $v_{D,\mathrm{radar}}$ is showing the stronger variation of the two plots. But, the plots of riming and the vertical wind velocities, here especially of the averaged one, show remarkably parallel trends.

The correlation coefficients between vertical wind velocity and riming is 0.58 for w, and 0.78 for $\langle w \rangle_{2\,\mathrm{km}}$. Scatter plots are shown in Figure 5.11. The horizontal bars are equivalent to the bars in Figure 5.10, and mark the spread of riming. The results will later on be discussed in more detail.
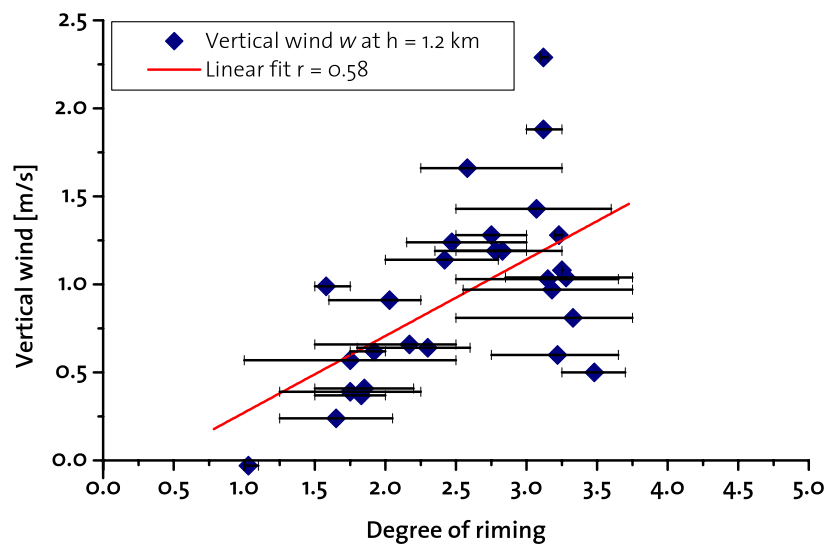
a)
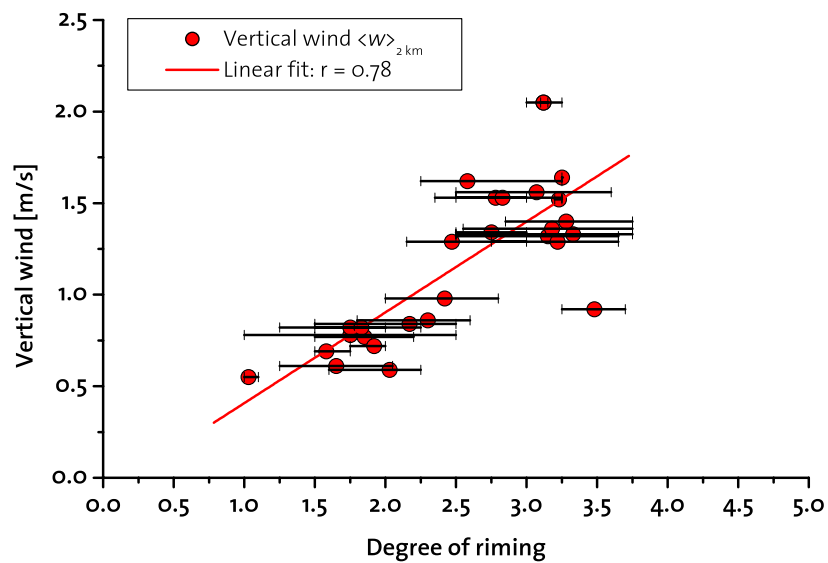
b)

Figure 5.11: *Correlation between vertical wind velocities and riming. For the determination of vertical winds, $v_{D,\mathrm{radar}}$ was first at the height 1.2 km above ground (a), and second averaged over a 2 km layer up to 3.2 km above ground (b). The horizontal bars mark the spread of riming. Additionally the linear fits are given.*

5.6   Discussion of the estimation of vertical winds

After the lag time correction, vertical winds could be estimated from the combination of radar and in-situ data. For situations without embedded convection, the wind velocities derived by the method for the estimation of vertical winds have the same order of magnitude as the literature values (Sec. 2.3.1). Unfortunately, independent measurements of the vertical wind velocities could not be made for comparison. Because the sources of error for the estimation of vertical winds are difficult to quantify, it is termed "estimation" and not "calculation". But errors can be addressed qualitatively.

Essential but in its error not easily quantifiable is the validity of the assumption that for an advected region of a precipitation system the composition of hydrometeors at a given height changes only slowly or that hydrometeors falling out of the volume are substituted by similar particles from higher levels. More precisely this postulate is – after lag time correction – identical to saying that the particles which are scanned by the HVSD are representative for the radar resolution volume in the corresponding height. As discussed in Section 5.4, the values of the correlation coefficients are a test for this, though they are limited by the errors of reflectivity computation from HVSD data and by the assumptions of mass-size relations (cf. Sec. 5.2). Furthermore, theoretically but not very likely even identical reflectivities could be produced by quite different compositions of hydrometeors. Generally, the estimation of vertical winds is the more sensitive to errors in deter-mination of lag times the more convective a system is and the more the hydrometeor composition varies.

Under the assumption that the hydrometeor composition remains identical and lag time was de-termined correctly, errors of vertical wind estimation still can be caused by errors of radar and HVSD Doppler velocity measurement. The latter was discussed in Section 5.2 and the error of radar Doppler velocity is at best estimated by the velocity resolution (cf. Eq. 2.31) of 0.125 m s^{-1}, if the horizontal wind can be neglected and there is no shear of the vertical wind. Even strong horizontal winds do not influence the measured Doppler velocity if the radar is perfectly vertically aligned. By the small but finite opening angle of the beam, only the spectrum will widen, if parti-cles are close to uniformly distributed in the volume. If an infinite narrow radar beam is tilted by α_{tilt} degree, an error will be added to the measured Doppler velocity. This error is for a horizontal wind v_h given by

$$\Delta v_D = v_h \cdot \cos\left(90° - \alpha_{\mathrm{tilt}}\right) \quad . \tag{5.4}$$

v_h is here not generally equivalent to the advection velocity v_a. The velocities within a cloud can be much different from the velocity of the cloud. Equation 5.4 yields with v_h = 10 m s^{-1} and α_{tilt} = 1° a Δv_D of 0.17 m s^{-1}. This error has the same order of magnitude as the veloc-ity resolution of the radar. The radar was adjusted with help of a level to a precision better than 1°.

5.7 Case Nov. 7: Comparison of two phases

Outgoing from riming (Fig. 5.6), we select two phases with significantly different degrees of riming for comparison of the characteristics. The time between 10:00 and 11:00 LT showing moderately riming is addressed here as phase I. The 50 minutes between 15:00 and 15:50 LT denoted in the following as phase II is chosen because riming was more than dense. We now want to look at these two different phases in more detail. Figures 5.12 and 5.13, resp., show data from the X-band radar for the two phases. These are reflectivity Z, Doppler velocity $v_{D,\mathrm{radar}}$ and Doppler delta Δ_D (cf. Sec. 4.3.5). For the latter a time scale with $\Delta t = 900$ s was chosen. The black line marks the height of the upper measurement site. The first phase has a generally lower reflectivity, and has a vertical profile of reflectivity and velocity that is more similar to the one typical for stratiform precipitation as shown in Figure 2.6: Compared to phase I, the second phase exhibits a pronounced secondary maximum of reflectivity besides the bright band. It is at about 2 to 3 kilometers height as can also be seen in the Doppler spectrum from the end of phase II (Fig. 5.14b): The secondary maximum of reflectivity is 3 km above ground and about as strong as the bright band. The reflectivity HTI and the Doppler spectrum from phase I (Fig 5.13a) show a distinct bright band signature, but low reflectivities above. Large parts of the secondary maximum in phase II coincide with the regions of Doppler velocities smaller than 0 m s^{-1} (Fig 5.13b). In phase II, there are additional regions of negative Doppler velocity in the 1 to 2 kilometers above the bright band.

The position of the bright band can also be seen in the Doppler velocity HTI by the change from the lower fall velocities of snow to the higher fall velocities of rain. In phase I, the large patches of negative Doppler velocity are missing, especially those in higher altitudes. Only smaller patches can be seen, mostly directly above the bright band. But, between 10:25 and 11:00 LT there is a phase with some small negative patches below three kilometers height. But most of all, there is a strong variance in Doppler velocity in this height. This pattern is amplified in the Doppler delta plot. This is a region of strong deviations from the mean Doppler velocity.
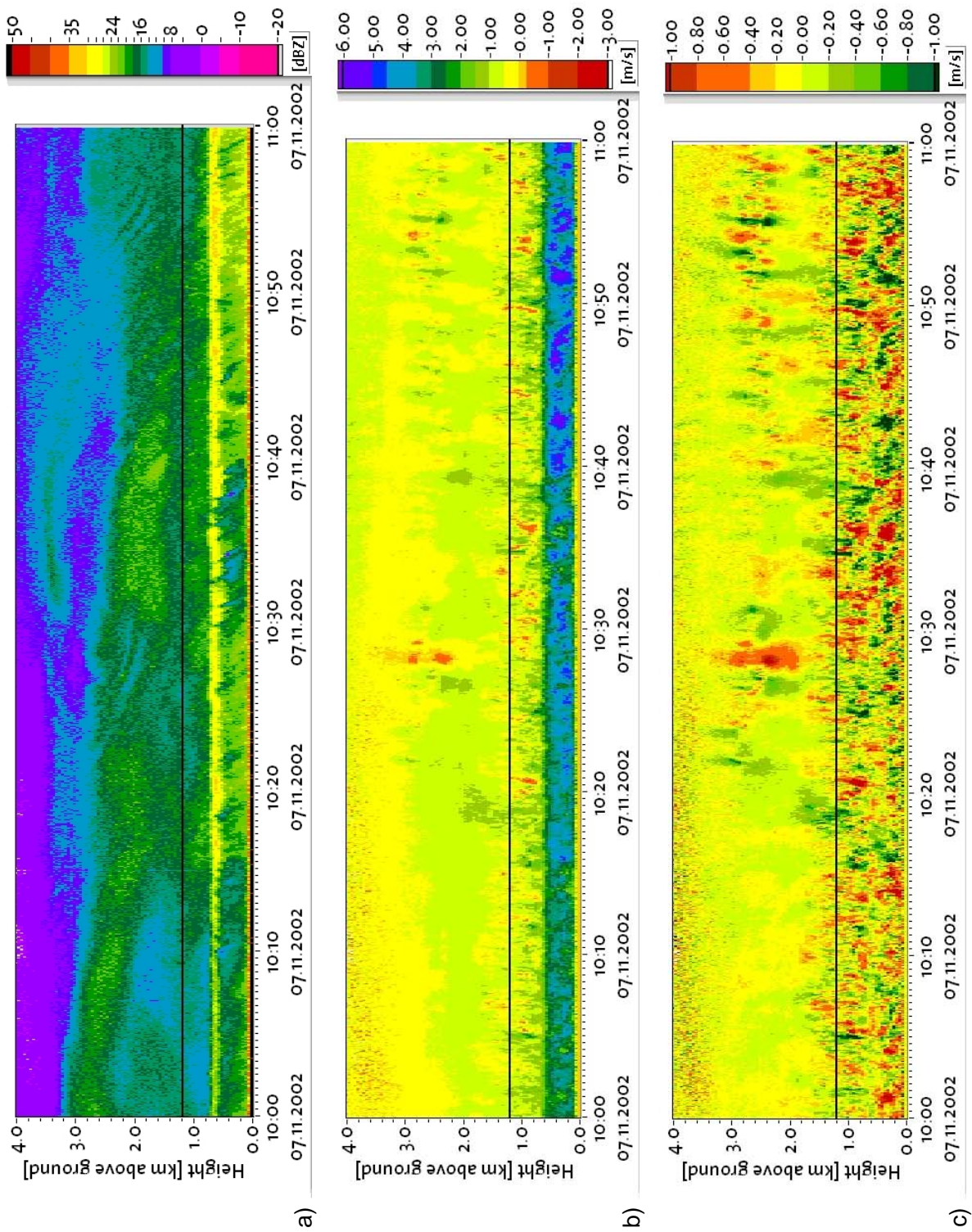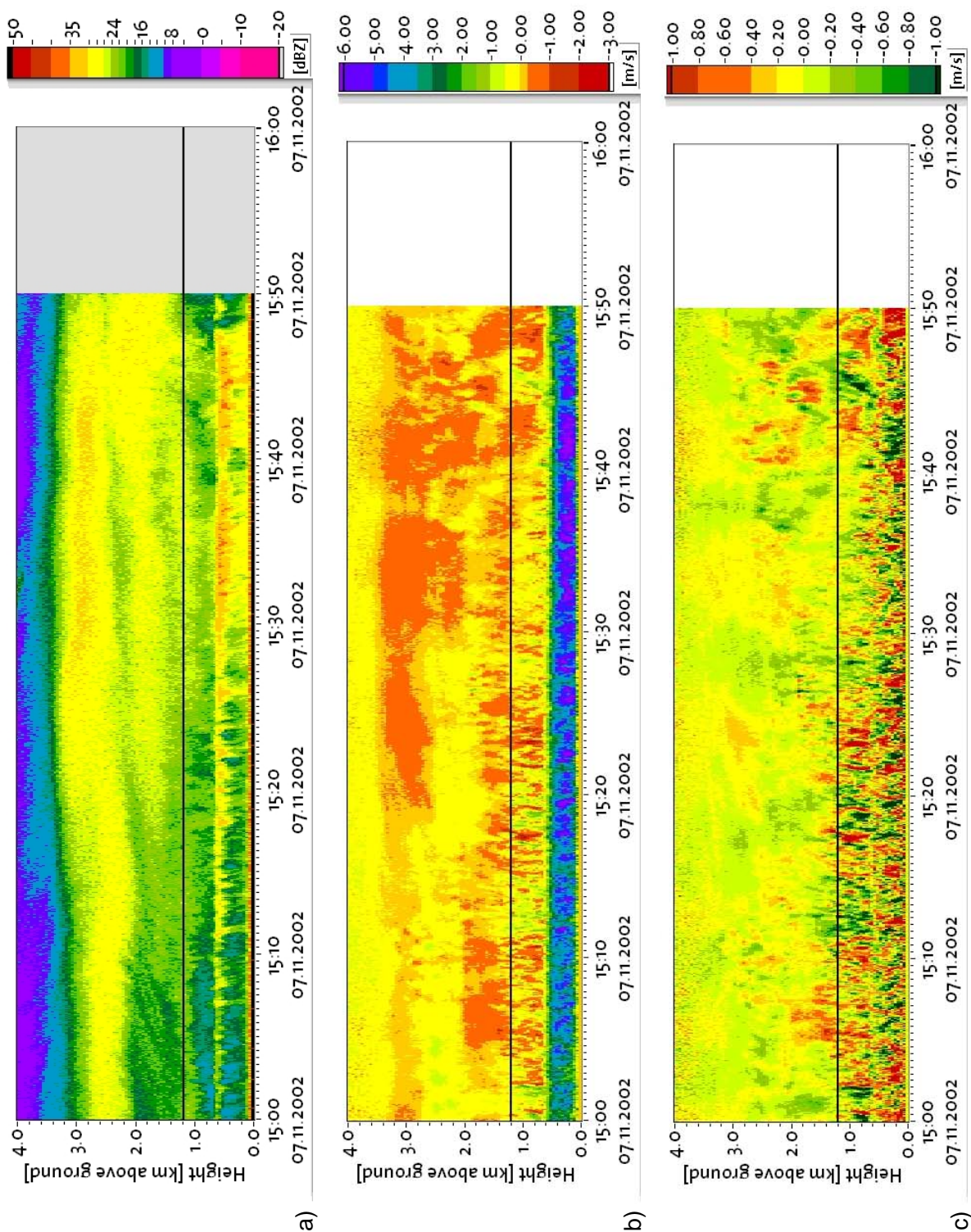
Figure 5.12: *X-band radar data for phase I: 10:00 until 11:00 LT on Nov. 7, 2002. Shown are (a) Reflectivity Z [dBZ], (b) Doppler velocity $v_{D,\mathrm{radar}}$ [$m\,s^{-1}$] and (c) Doppler delta Δ_D [$m\,s^{-1}$] with $\Delta t = 900$ s. The black line marks the height of the upper measurement site.*
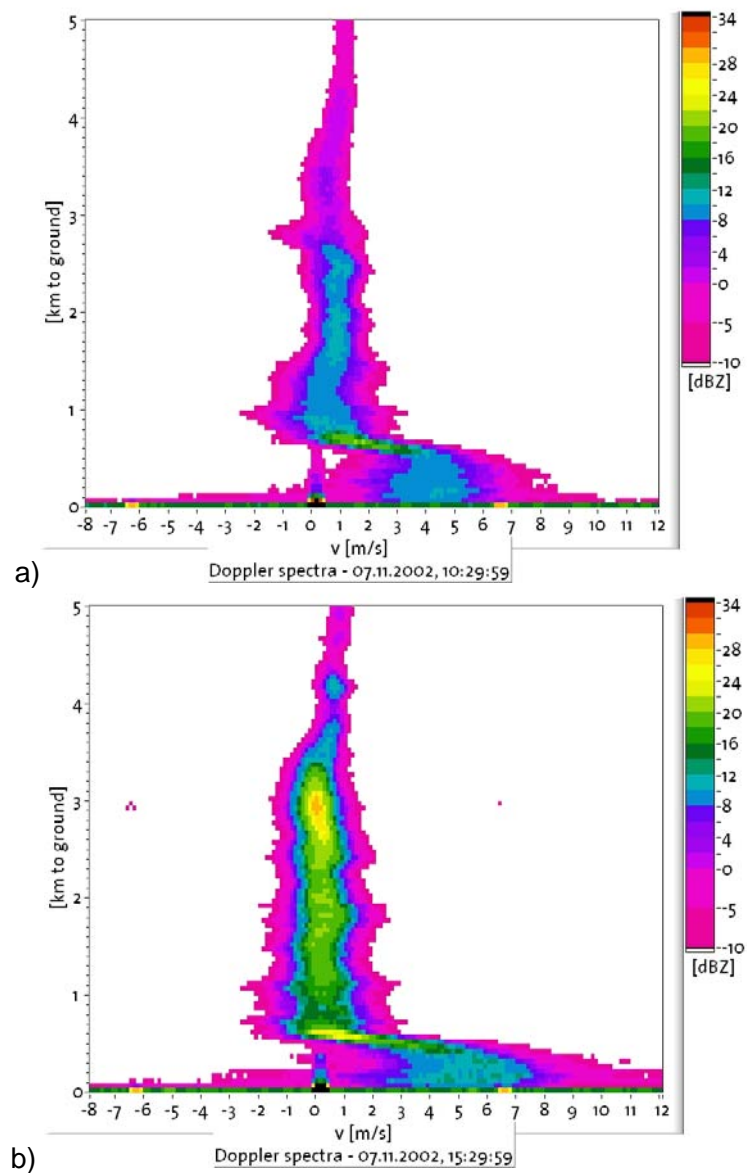
Figure 5.13: *X-band radar data for phase II: 15:00 until 15:50 LT on Nov. 7, 2002. Shown are (a) Reflectivity Z [dBZ], (b) Doppler velocity $v_{D,radar}$ [$m\,s^{-1}$] and (c) Doppler delta Δ_D [$m\,s^{-1}$] with $\Delta t = 900$ s. The black line marks the height of the upper measurement site.*

a)

b)

Figure 5.14: *Doppler Spectra from 10:30 LT (a: phase I) and 15:30 LT (b: phase II). The spectra are averaged over 60 s.*

5.8 Interpretation of the two phases and of the Doppler delta

Two different phases of the November 7 case have been classified and analyzed in detail in the previous Section 5.7. It is noticeable that phase I has more characteristic structures in the Doppler delta Δ_D. As mentioned before, this can be seen in 2 to 3 km height at the end of phase I (Fig. 5.13c). Δ_D changes quickly from positive values close to 1 m s^{-1} to negative

values of comparable amplitude. Because this region is in snow, $|v'_T|$ will probably be small and as discussed in Section 4.3.5 this structure can be interpreted as alternating patches of upward and downward deviation of the vertical wind velocity from its mean value, and thus as "whirls" or turbulence. In contrast, the high absolute values of the Doppler delta below the bright band can be caused by the higher variance of particle fall velocity in rain.

The horizontal extent of these whirls E_h can be estimated by the advection velocity of the precipitation system v_a (Eq. 4.4) and the time needed for crossing the radar t_a. This can be different from the time scale of $\Delta t = 900$ s for the computation of Δ_D in which the whirls became visible. For v_a, the wind velocity from the single Doppler wind field (Fig. 5.4) is taken, which is 13 ± 5 m s^{-1} for the sector of phase I shown in Figure 5.15a. Here, the bar marks a t_a of 125 s. This yields a horizontal extent of 1.6 ± 0.6 km. In Figure 5.15b an embedded convective cell from phase II with a large updraft region is shown. Here, the bar corresponds to 500 s. v_a is 14 ± 5 m s^{-1}, and thus is E_h 7 ± 2.5 km. Thus is the horizontal extent of the embedded convective cells in phase II approximately 4 times larger than the turbulent structures in phase I. The vertical extents are roughly 1.5 and 0.6 km, resp.
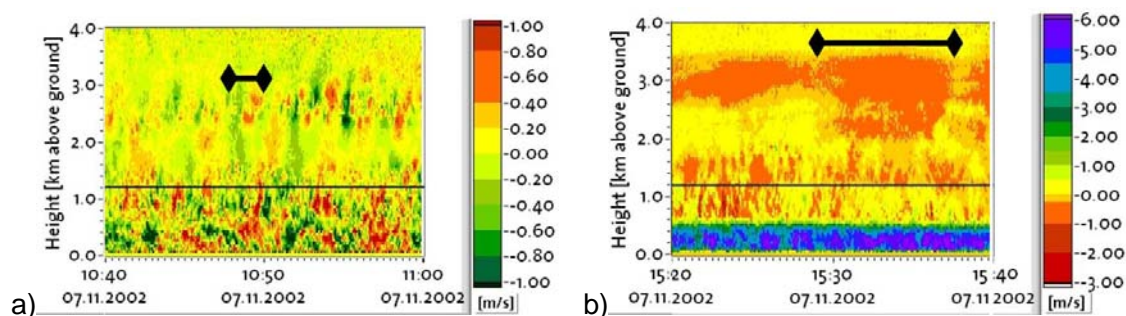
Figure 5.15: *Cutout of Fig. 5.12c and 5.13b, resp., but with bars marking approximate scales of turbulence (a: the bar corresponds to 1.6 ± 0.6 km) and embedded convection (b: the bar corresponds to 7.0 ± 2.5 km).*

The strong secondary maximum of reflectivity at the end of phase II at high altitudes might either be interpreted as an accumulation of particles due to vertical winds or as a region, where the Hallett-Mossop effect takes place, and thus splinter production by riming and ice multiplication (cf. Sec. 2.1.4 p. 16). In phase I the degree of riming is 1.9 and in phase II 3.3, whereas the vertical wind $\langle w \rangle_{2\,\mathrm{km}}$ increased from an average of 0.7 to 1.8 m s^{-1}. These two wind averages are only based on few data points, therefore the correlation between vertical wind velocity and riming will be investigated statistically for all cases in the following sections.

5.9   Extension to the other cases of winter 2002/2003

Table 5.1 gives an overview over the different cases of RAMS including dates and meteorological characteristics. Note that the given times are based on the availability of data from the "MeteoXrad" weather station at the lower site (cf. Sec. 3.4). The other instruments have not all the time been running simultaneously. For further analysis, the filter rules explained in Section 5.3 have been applied to all 7 cases of winter season 2002 / 2003 that have been taking place at Mt. Rigi. In total 49 Formvar slides remained, which corresponds to 490 minutes of measurements.

Table 5.1: *Overview over the different case studies of the field campaign RAMS taking place at Mt. Rigi including dates and meteorological characteristics. Note that the given times are based on the availability of data from the "MeteoXrad" weather station at the lower site (cf. Sec. 3.4). The other instruments have not all the time been running simultaneously.*

Start		End		Temperature range at lower site		Rain total	Meteorological condition
Date	LT [h]	Date	LT [h]	Minimal [°C]	Maximal [°C]	[mm]	
Nov 03, 2002	17:09	Nov 04, 2002	12:39	6	13	10.0	North/west blocking
Nov 06, 2002	19:41	Nov 07, 2002	15:50	1	6	4.4	Occluded frontal system
Dec 16, 2002	15:29	Dec 17, 2002	11:44	5.5	6.5	13.4	North blocking
Jan 27, 2003	17:03	Jan 29, 2003	16:06	4	10	1.6	North/west blocking
Mar 01, 2003	18:48	Mar 02, 2003	16:49	6	10	11	Several fronts
Mar 06, 2003	15:07	Mar 07, 2003	08:34	1.5	12	13	Cold front
Apr 01, 2003	23:50	Apr 02, 2003	14:00	3.5	14	10	Cold front

For the Formvar samples remaining after filtering, Figure 5.16a is the scatter plot of the radar Doppler velocity $v_{D,\mathrm{radar}}$ versus the degree of riming. The stars show $v_{D,\mathrm{radar}}$ at 1.2 km above the ground, and dots display $\langle v_{D,\mathrm{radar}}\rangle_{2\,\mathrm{km}}$, which is the average of $v_{D,\mathrm{radar}}$ over the height level 1.2 till 3.2 km above ground. The situations were there are zero or negative velocities, correspond to in average hovering or upward moving particles, and would be called convective in the sense of CONV I (cf. Sec. 4.3.2). Respective data points have been found for degrees of riming larger than RIM = 3.
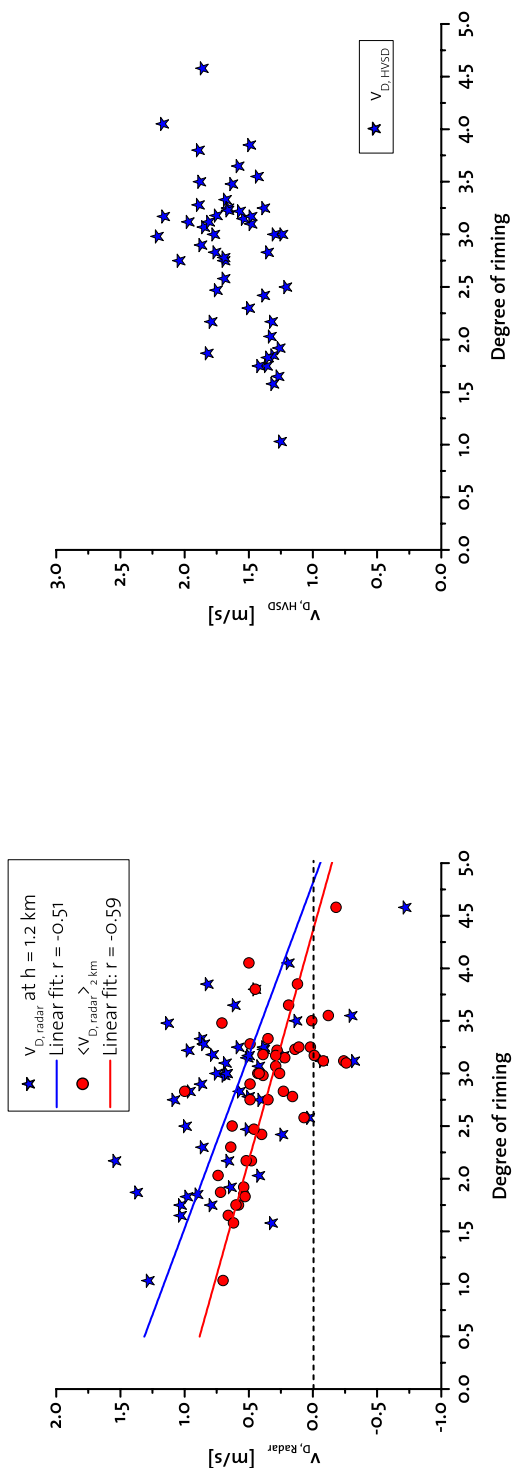
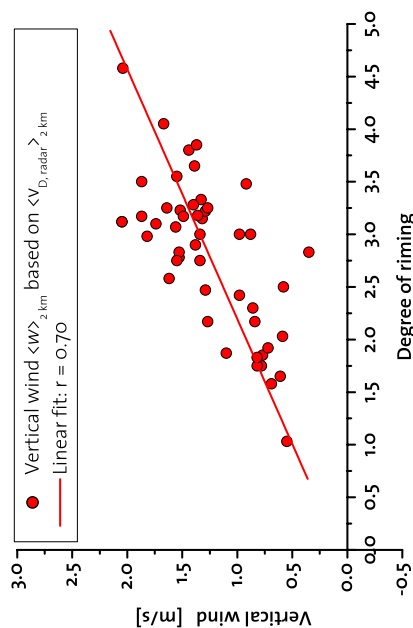(a) $v_{D,\mathrm{radar}}$ at h = 1.2 km and $\langle v_{D,\mathrm{radar}}\rangle_{2\mathrm{km}}$ versus riming.
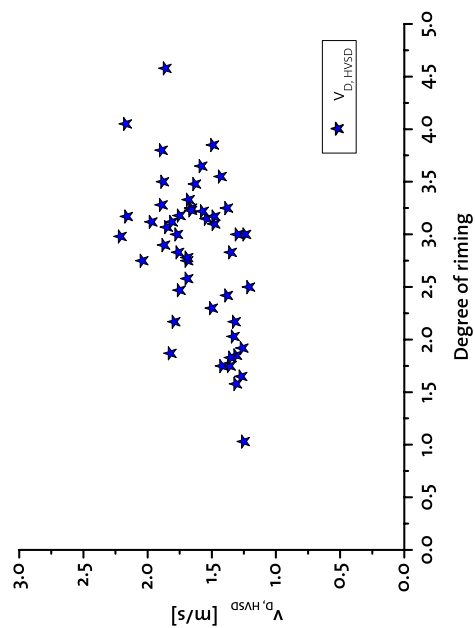
(b) $v_{D,\mathrm{HVSD}}$ versus riming.
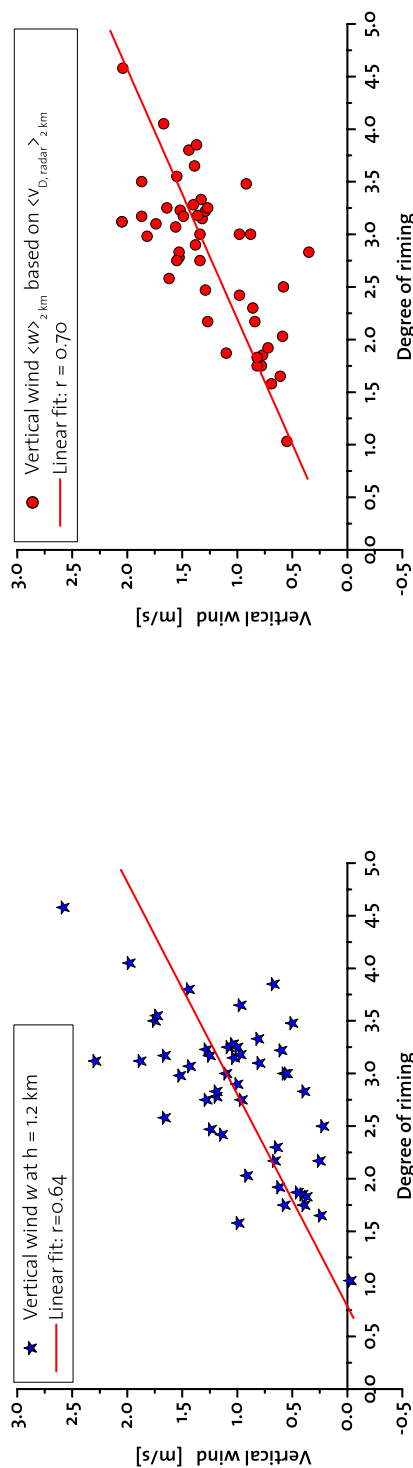
(c) Vertical wind w based on $v_{D,\mathrm{radar}}$ at h = 1.2 km.

(d) $\langle w\rangle_{2\mathrm{km}}$ versus riming.

Figure 5.16: *Scatter plots of the data of all cases: radar and HVSD Doppler velocities and vertical winds versus riming.*

$\langle v_{D,\text{radar}} \rangle_{2\,\text{km}}$ has mostly smaller values than $v_{D,\text{radar}}$ has at h = 1.2 km. Though the data points show a considerable spread, $v_{D,\text{radar}}$ and $\langle v_{D,\text{radar}} \rangle_{2\,\text{km}}$ (Fig. 5.16a) decrease with increasing riming. The fit line for $\langle v_{D,\text{radar}} \rangle_{2\,\text{km}}$ lays $\approx$ 0.5 m s^{-1} lower than and almost parallel to the one of $v_{D,\text{radar}}$. For the two cases are the correlation coefficients $r = -0.51$ and -0.59, respectively. But the Doppler velocity computed out of HVSD data $v_{D,\text{radar}}$ (Figure 5.16b) increases weakly with increasing riming. The difference between the velocities measured by radar and HVSD is the vertical wind speed. Figure 5.16c shows the scatter plot of w from 1.2 km above ground, whereas $\langle w \rangle_{2\,\text{km}}$ is given in Figure 5.16d. Here, the correlation coefficients between vertical wind velocity and riming is 0.64 for w, and 0.70 for $\langle w \rangle_{2\,\text{km}}$; and w shows the stronger spread of data. Table 5.2 summarizes statistical parameters of the plots and of the corresponding linear fits. The values will be discussed in the following section. For the correlation for all cases between $\langle w \rangle_{2\,\text{km}}$ and riming the standard deviation with respect to riming is 0.46 RIM, and the average spread of riming on the filtered Formvar samples is 0.5 RIM.

The Doppler delta Δ_D is a measure related to turbulence (Sec. 4.3.5). In Figure 5.17, the absolute value of Δ_D ($\Delta t = 900$ s) averaged over the 2 km between 1.2 and 3.2 km above ground is plotted versus the degree of riming. The correlation for a linear fit is only 0.37, and the slope of the fit line is with 0.07 very small. Also these results will be discussed in the following section.
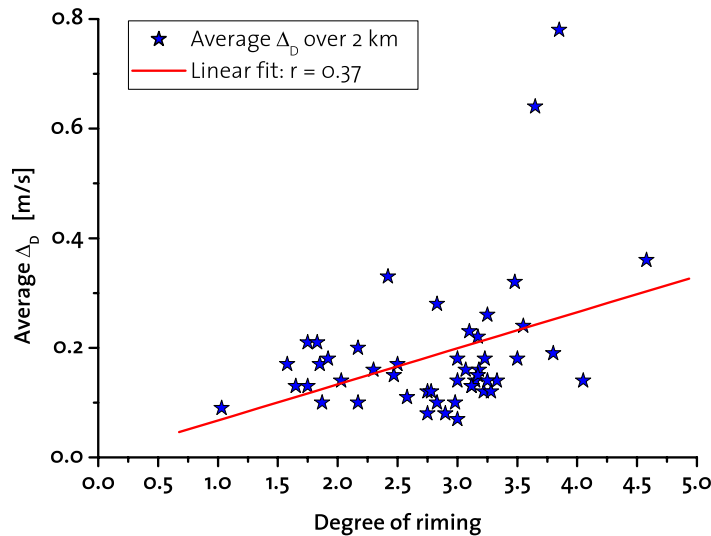
Figure 5.17: *Average of the absolute value of the Doppler delta Δ_D ($\Delta t = 900$ s) versus riming.*

5.10 Discussion: correlations of vertical winds, embedded convection and riming

The parallel development of riming and vertical wind velocity as seen in Figure 5.10 for the case of Nov. 7 is remarkable. It fits especially well for $\langle w \rangle_{2\,\mathrm{km}}$. Table 5.2 summarizes the statistical results of the investigation of the correlation between Doppler velocity, vertical winds, or Doppler delta and riming.

Table 5.2: *Statistics for correlation between Doppler velocity, vertical winds, and Doppler delta (averaged over 2 km) and the degree of riming. r is the correlation coefficient. The p-value as a test for significance is explained in Appendix B.*

Case	Type Y	r	r^2 [%]	p	A [m/s]	B $[\frac{\mathrm{m/s}}{\mathrm{RIM}}]$
				Linear fit: $Y = A + B \cdot \mathrm{RIM}$		
Nov. 7	w at h = 1.2 km	0.58	33	0.00126	-0.16±0.32	0.43±0.12
	$\langle w \rangle_{2\,\mathrm{km}}$	0.78	61	< 0.0001	-0.08±0.20	0.50±0.08
	v_D at h = 1.2 km	-0.51	26	0.0002	1.46±0.22	-0.30±0.08
	$\langle v_D \rangle_{2\,\mathrm{km}}$	-0.59	35	< 0.0001	1.00±0.13	-0.22±0.05
All	w at h = 1.2 km	0.64	41	< 0.0001	-0.39±0.25	0.49±0.09
	$\langle w \rangle_{2\,\mathrm{km}}$	0.70	49	< 0.0001	0.08±0.19	0.42±0.06
	Δ_D	0.37	14	0.0082	0.00±0.07	0.07±0.02

The high correlation coefficients of up to 0.78 for the correlation between vertical wind velocity and riming show the strong influence, vertical winds have on the degree of riming. The coefficients are higher for $\langle w \rangle_{2\,\mathrm{km}}$ than for w at h = 1.2 km. Thus, for riming the vertical winds in the whole region above the height of the measurement seems to be important. This makes sense because the particles grew in this layer. The r^2 values explain up to 50% of the scatter of riming. The correlations are very strongly significant with a p value < 0.0001, except for the case of w at h = 1.2 km where the correlation is only strongly significant (cf. App. B). The vertical wind increases by approximately 0.5 m s^{-1} per degree of riming. Problematic is only the extension to extreme values of riming: after filtering, there are no data points with RIM = 0 and only two with RIM > 4. So far, linear fits were investigated, and this with high resulting correlation coefficients.

If additional data points for extreme values are available, non-linear fits might be more appropriate: The degree of riming is a non-linear scale with respect to mass and also the influence of vertical winds on riming is not necessarily linear, though both non-linearities might compensate each other.

The Doppler velocity measured by the radar $v_{D,\mathrm{radar}}$ is a measure of convectivity in the sense of CONV I (cf. Sec. 4.3.2). Therefore, CONV I is especially useful to find embedded convective cells in radar data. In the data displayed in Figure 5.16a, there are only a few data points with negative Doppler velocity corresponding to convectivity in this sense, but here the detected degree of riming is high with values of at least RIM = 3. As shown for the case of Nov. 7 but also valid for the other cases, the regions with high reaching negative Doppler velocity are embedded in stratiform precipitation. Thus, there is a correlation between embedded convection and riming. But especially for the investigation of the influence of convection on the microphysics of precipitation, as e.g. on riming, the use of the definition that there is convection if there are updrafts (CONV II, cf. 4.3.3) is more suitable. All regions that are convective in the sense of *CONV I* are this also in the sense of *CONV II*, i.e. there are updrafts, but not necessarily vice versa. There can be more or larger regions, which are convective in the sense of CONV II. Furthermore, CONV II has the advantage that it is better quantifiable, and directly describing a likely reason for riming and not a phenomena combining particle and dynamical properties. We remember (cf. Sec. 4.3), that $v_{D,\mathrm{radar}} = 0$ could be realized by small, slowly falling particles (≈ 0.5 m s^{-1}) and a very weak updraft as well as by faster falling graupel (≈ 3 m s^{-1}) and accordingly stronger updrafts.

For the correlation for all cases between $\langle w \rangle_{2\,\mathrm{km}}$ and riming, the standard deviation with respect to riming is 0.46 RIM. This is in the same order of magnitude as the average spread of riming on the filtered Formvar samples of 0.5 RIM. Thus, the strong spread of data could be explainable by the strong spread of riming within a small volume of ice precipitation. But beside this strong spread of riming degree within single Formvar samples and thus also within a sampling volume, there are several other possible causes for the scatter of data as measurement errors (Sec. 5.6) and other factors on riming that could not unambiguously be excluded. These are, e.g., changes in size distribution of supercooled cloud droplets with changing air masses. For instance, in the case Nov. 7 the front passed at roughly 13:00 LT the measurement site. This is short time (≈ 1.5 h) after the vertical winds increased (CONV II) and about two hours before the larger embedded convective cells came (CONV I). This front might also have brought other size distributions of super-cooled cloud droplets that are not only explainable by condensation caused by updrafts, even if the humidity at the ground (Fig. 5.2b) stayed at a similar level. Other influencing factors as, e.g., habit and size distribution of ice crystals and also temperature have been mentioned in Sec. 2.1.4. But in the observed cases, strong vertical winds always caused high riming. Whereas for weak vertical winds also sometimes higher riming was observed. This would lead to a conceptual model that strong updrafts cause high riming - either by condensation or by an increased particle residence time. But if there aren't any strong updrafts present, there

might be other sources of super-cooled cloud droplets that can lead to higher degrees of riming.

The correlation between Δ_D with $\Delta t = 900$ s and riming has a low correlation coefficient of 0.37 and is with a p-value of 0.0082 only weakly significant. On this scale turbulence seems to have a smaller influence on riming than high reaching updrafts. This might be different on smaller turbulence scales, as the influence of turbulence on riming is theoretically given by modifying the air flow around the particles. Furthermore, we have seen in Section 5.8 that in the investigated case study of Nov. 7 the horizontal extent of the structures in Δ_D in phase I are approximately 4 times smaller than the embedded convective cells at the end of phase II. Thus, the investigation of correlations between Δ_D and riming is more sensitive to small advection angles (see discussion in Sec. 5.4).

5.11 Comparison to literature and related studies

In addition to relations between this thesis and literature already shown either in the introduction (Chap. 1), the Chapter 2 with explanations of the theoretical background, or, for instance, in the section defining convection (Sec. 4.3), we want to reveal and discuss some aspects here.

Because there are for this study no direct independent measurements of vertical wind speed available, the results can only be compared to literature. Houze (1993) states that there is typically a steady updraft of a couple of tens of cm s^{-1} in stratiform precipitation from nimbostratus clouds. Together with the definition that in stratiform precipitation (cf. Sec. 2.3.1) the vertical winds velocities are smaller than the particle fall velocities, which are for snow typically in the range 1 to 3 m s^{-1}, the range of 0 to 2.25 m s^{-1} for the estimated wind velocities seems to be reasonable for stratiform precipitation with weak embedded convection.

Compared to previous work (e.g. by Mosimann, 1995) on related topics but performed with the radar preceding its modernization, the ameliorated temporal resolution offers the possibility of a more detailed investigation of small scale structures. For instance, the embedded convective cell shown in Figure 5.15b needed 500 s to pass over the radar. For the modernized version of the radar, this corresponds to 500 vertical profiles – with $n_p = 512$ pulses each, simultaneously giving a high velocity resolution – instead of only about 17 profiles (with $n_p = 128$ or later also 512 pulses each (Göke, 1999)). Further in e.g. Figure 5.15b, there are also smaller structures of embedded convection visible in the Doppler velocity HTI or in Figure 5.15a in the plots of the Doppler delta Δ_D corresponding to turbulence. In the latter figure, the bar marks a structure corresponding to 125 s equivalent to 125 vertical profiles with the new and only 4 with the previous version of the radar. Thus, small but for this study relevant structures are with the modernized radar much better resolvable.

With the radar before its modernization, Mosimann (1995) found in his investigation, a relation used for the prediction of riming in stratiform precipitation of the form $RIM = (10.9 \cdot < v_D > -8.1)^{1/2}$, where v_D [m s^{-1}]. This relation was used for stratiform situations only, which where in his study defined by a range of the convection index κ (defined by Equation 4.5) between 0 and 0.2. This seems to contradict the results received in this study as, for instance, the plot of $v_{D,\mathrm{radar}}$ versus riming in Figure 5.16a. Mosimann gives a probability of approx. 76% for an accuracy of ± 1 degree of riming. In Section 4.3.4 κ was analyzed in detail, and it could be shown that it describes a mixture of convection and turbulence, and especially that a range of κ between 0 and 0.2 is not necessarily equivalent to a stratiform period. Even if it is received by averaging over a long time to cancel out effects by turbulence. A further possible explanation for the differences is that as explained in Section 5.4, the lag time filtering – not applied in this form by Mosimann – accomplishes the important task to filter data, and to increase the probability to see with the radar those particle in its growing regime which later fall down at the upper site. Finally, the study by Mosimann is supposed to be restricted to strictly stratiform precipitation, and in the plot Figure 5.16a also stronger vertical winds are included. If reducing the data to cases with low vertical wind speed, the differences might be explainable by the conceptual model proposed in Section 5.10 that strong updrafts cause high riming - either by condensation or by an increased particle residence time. But if there aren't any strong updrafts present, there might be other sources of super-cooled cloud droplets that can lead to higher degrees of riming.

Examples for investigation of the influence of orographically induced updrafts on riming are:

Houze and Medina (2003) investigated orographic enhancement and observed over the first chain of a larger scale ridge an enhanced probability for riming and/or aggregation. Because they interpreted the data of a 60 km apart scanning polarimetric radar, these two processes were not distinguishable but aircraft measurements found aggregates with evidence of riming. Basing on radial velocity measurements by the same scanning radar, they explain this enhancement by "cellular overturning" (as suggested by Smith (1979)). Compared to the work of Houze and Medina (2003), this thesis has the advantage to use a vertically pointing radar with the ability to split radar Doppler velocity into vertical winds and particle movement, because of the combination with in-situ measurements. Further, as well vertical winds as riming are analyzed quantitatively and their quantitative relation is shown.

The investigation of Harimaya and Nakai (1999) showed for case studies in Japan that rime mass increased with an increase in snowfall intensity, and with an increase in horizontal wind speed when the mass flux of ice crystals was subtracted. As an explanation, they postulated but did not prove that an increase in horizontal wind speed leads to an increased strength of updrafts and thus also to more supercooled cloud droplets and finally to riming, especially if the wind comes perpendicular to the ridge where the measurements took place. Thus, their results fit well to those of this thesis that provides the missing link to directly show the influence of updrafts on riming.

Chapter 6

Summary and conclusions

The measurements for the field campaign **RAMS** (**R**iming, **A**ggregation, and **M**ass of **S**now) combine remote sensing and in-situ measurements in order to investigate the microphysics of snowfall in parallel with dynamical aspects. The chosen setup allows for simultaneous measurements at different height levels, but especially also the interpretation of processes in the free atmosphere apart from both instruments: From the lower measurement station, a precipitation system is observed by radar, i.e. by remote sensing, at the height corresponding to the upper site only short time before the system arrives there. This time difference can be corrected for by the proposed lag time correction method, and the influence of the dynamics observed by the radar on the microphysical properties of ice precipitation measured at the upper station can be investigated.

The recently modernized mobile vertically pointing X-band Doppler-radar of the Swiss Federal Institute of Technology was tested as part of this thesis. Further, a software was developed for data acquisition as well as for analysis. This instrument proves to have excellent properties with high time (1 s) and velocity (0.125 m s^{-1}) resolution. Especially the high time resolution makes small scale structures visible, which has not been possible in the past.

Several existing and partly contradictory definitions of convection were presented in this thesis. They differ especially for weak convection. The definition of convective precipitation by the presence of updrafts that are stronger than the particle fall velocity (CONV I) was closer investigated. This is equivalent to negative Doppler velocities measured by a vertically pointing radar. This definition is thus relevant for radar investigation but less suitable for the investigations of influences of convection on riming: A vertically pointing Doppler-radar measures the sum of vertical wind speed w and terminal particle fall velocity v_T. Thus, there is an ambiguity that slow updrafts together with slow falling particles respective fast falling particles as, e.g., graupel together with strong updrafts can equally result in a, for instance, vanishing Doppler velocity. Furthermore, the criterion given by CONV I provides primarily a threshold between convective and not convective precipitation, but not a quantification. However, because of its relation to Doppler velocity, it is

especially suitable for the detection of embedded convective cells by means of radar.

To receive a quantification, a second definition of convection was introduced basing on the strength of vertical wind velocity (CONV II) – here restricted on updrafts. Further, a method was proposed for the estimation of vertical wind velocity based on a combination of measurements by radar and by the **H**ydrometeor **V**elocity and **S**hape **D**etector (**HVSD**). Now v_T and w can be separated. Preceding to this, data are corrected for the lag time which a precipitation system needs to cover the distance from above the lower measurement site to the upper one, where the HVSD is placed. For this correction, reflectivity is computed and cross correlations between radar and HVSD data performed. To determine the degree of riming, Formvar samples are taken at the upper station. Finally, the combination of the methods allows to investigate the influence of vertical winds on the degree of riming. The data were filtered on the basis of maximal temperature and minimal rain rate. Also, lag time and its correlation coefficients proved to be a powerful tool for filtering data, and to ensure that the measurements of both sites were performed on the same region of the precipitation system.

Because of the high time resolution of the radar, in the case studies turbulent structures of a scale of approximately 1.6 ± 0.6 km could be shown as well as embedded convective cells with negative Doppler velocity of a size up to about 7.0 ± 2.5 km.

For snow, the proposed Doppler delta, $\Delta_D = \bar{v}_{D,\mathrm{radar}} - v_{D,\mathrm{radar}}$, provides a measure closely related to turbulence. If on the selected time scale (Δt) the variation of terminal fall velocity of the hydrometeors v_T' is small compared to the deviation of vertical winds w' from the mean, it yields: $\Delta_D \approx w'$. But in the data, no predominant influence on the degree of riming could be found originating from turbulent structures that were not combined with high reaching updrafts.

After lag time filtering, embedded convection in form of negative Doppler velocities was only observed together with riming degrees of 3 or above. For the correlation between updrafts and degree of riming, a coefficient r of 0.58 is received for a case study. If the vertical wind is based not only on the radar Doppler velocity measured at the height level corresponding to the upper station (w at h = 1.2 km), but on its average over a 2 km thick layer above the upper site ($\langle w \rangle_{2\,\mathrm{km}}$), the correlation coefficient r increases to 0.78. Applying the same filtering rules to all data of the winter season 2002/2003 taken at Mt. Rigi the equivalent correlations have $r = 0.64$ for w and 0.70 for $\langle w \rangle_{2\,\mathrm{km}}$, respectively. The correlations between vertical wind and riming are, if based one height level, strongly significant and those based on the average are very strongly significant. Thus, the strong influence, vertical winds have on the degree of riming could be shown, and especially that the winds in a thick layer are of importance. This makes sense, because the riming growth of particles will also take place not only at one specific height.

However, the data show a considerable spread. Several contributions to this are possible: The composition of hydrometeors can alter on its way from above the radar to the upper measurement site or for higher advection angles different regions of the precipitation system are advected.

Besides riming degrees within a sampling volume are not uniform: The average spread of riming on the filtered Formvar samples is 0.5 RIM, and could thus explain the standard deviation with respect to riming of 0.46 RIM found for the correlation for all cases between $\langle w \rangle_{2\,\mathrm{km}}$ and riming. But also other factors possibly influencing riming as, e.g., habit and size distribution of ice crystals and cloud droplets have been discussed. Nevertheless, in the observed cases, if strong updrafts were observed, riming was always high. This would lead to a conceptual model that strong updrafts cause high riming - either by condensation or by an increased particle residence time. But if there are no strong updrafts present, there might be other sources of super-cooled cloud droplets that can lead to higher degrees of riming.

This possible relevance of other influences at low updraft velocity could also be an explanation for the seemingly deviating literature values of one work cited in the discussion for relations between Doppler velocity and riming. But those values were also restricted to measurements of stratiform precipitation, defined by a deviating definition that could be partly misguided by the ambiguous character of Doppler velocity. Otherwise, as investigated in the discussion, the findings of this thesis fit well to related literature or seem to provide an important completion, respectively.

Chapter 7

Outlook

As possible future expansion of this study, a higher amount of cases especially with extreme low or high riming would be desirable. A basic question in this context is: what could be changed in the instrumentation and measurement setup? Especially an automatized or even continuous sampling of the degree of riming would increase the amount of available data. If additional instrumentation was available, independent measurements of the vertical wind would offer a validation possibility. Also a scanning - or even polarimetric - radar at the lower site would improve the knowledge of the hydrometeor types and dynamics, and could follow more precisely the way of precipitation from the lower to the upper site. For this purpose one could think alternatively about a not scanning radar at the upper station looking horizontally to the area above the lower station. Both possibilities could contribute to study the phenomena of arising embedded convective cells. At an other measurement site, also dual Doppler wind fields could identify special synoptic and orographically induced conditions, which are the reason for the generation of updrafts and embedded convective cells in stratiform winter precipitation, and thus create pre-requisites for riming to occur. In this context the question has to be addressed, if dynamically caused possibly steady updrafts and thermally induced vertical winds equally influence riming – as so far has been assumed. Thus, the influence of the orographic situation will have to be further investigated in parallel with the transferability of the results to other locations.

To better understand the influence of other microphysical aspects more microphysical measurements as, e.g., on cloud droplet size distributions would be desirable. A smaller resolution volume or a switchable pulse repetition frequency would ameliorate the resolution of the X-band radar.

Plans exist to make the shape detection of the HVSD three dimensional. Further calculation of reflectivity could be improved by applying more accurate algorithms and by, for instance, applying Mie scattering theory. Extended parallel measurements of snow mass would not only improve the reflectivity calculation but would simplify the application to modelling. But also by ameliorating the comparison of radar and HVSD data, hypotheses for mass-diameter-relations might be testable or - despite of the many influencing factors - even be deducible.

Appendices

Appendix A

Table of abbreviations

a	Parameter in several equations	
a	Radius	
a	As subscript denoting ambient air	
A_{eff}	Effective lower area of falling particle	
A_a	Active measurement area of HVSD	Eq. 3.2
A_e	Effective antenna area	
a_i	Location dependent parameter in	Eq. 2.7
a_m	Parameter of mass-size relation	Eq. 2.11
a_V	Radar calibration parameters	Eq. 3.1
B	Buoyancy	Eq. 2.47
b	Parameter in several equations	
b_m	Parameter of mass-size relation	Eq. 2.11
b_V	Radar calibration parameters	Eq. 3.1
c	Speed of light (vacuum)	
CAPE	Convective available potential energy	Sec. 2.3.3
CCL	Cumulus condensation level	Sec. 2.3.3
CCN	Cloud condensation nuclei	Sec. 2.3.3
C_c	Correction for snow reflectivity factor	Eq. 2.37
C_D	Drag coefficient	
$C_{d,j}$	Correction for snow reflectivity factor	Eq. 2.38
CONV I	Type of convection	Sec. 4.3.1
CONV II	Type of convection	Sec. 4.3.1
c_p	Specific heat of dry air	
D, d	Diameter	
DSD	Drop size distribution	
$d_{C,u}$	Distance between point C and upper measurement site	Fig. 5.9
d_{in}	Inner width measured by the HVSD	Sec. 3.8

$d_{l,u}$	Distance between point lower and upper measurement site	Fig. 5.9
d_{out}	Outer width measured by the HVSD	Sec. 3.8
d_{max}	Maximal diameter measured by the HVSD	Sec. 3.8
D_v	Diffusion coefficient	
e	Water vapor pressure	
E_c	Collision efficiency	Eq. 2.10
E_h	Horizontal extent of embedded convective cell	Eq. 4.4
$e_s, e_{s,i}$	e at saturation with respect to plain water (resp. ice) surface.	
ETH	Swiss Federal Institute of Technology	
E_v	Vertical extent of embedded convective cell	
F	Free energy	
FFT	Fast Fourier transformation	
Fr	Froude number	Eq. 2.53
f_r	Rimed mass fraction	Eq. 2.8
g	Gravitational acceleration	
g_c	Antenna gain corrected for Gaussian beam profile	Eq. 2.18
g_{max}	Maximal antenna gain	
$g(\theta, \varphi)$	Antenna gain in direction given by θ and φ	Eq. 2.12
H	Thickness of fluid	Sec. 2.3.4
h, h_{max}	Height and maximal height used for radar measurement	
h_{in}	Inner height of particle	
h_m	Height of mountain	Sec. 2.3.4
HTI	Height time diagram of radar measurements	
HVSD	Hydrometeor velocity and shape detector	Sec. 3.8
i	Either subscript signifying ice or index for summation	
IAC***ETH***	Institute of Atmospheric and Climate Science of ETH Zürich	
j	Subscript marking property of the single particle j	
K	Related to complex refractive index m by $(m^2-1)/(m^2+1)$	
k_B	Boltzmann's constant	
K_s	Attenuation in snow Eq. 2.36	Eq. 2.36
l	As subscript signifying larger collecting particle in Eq. 2.10	Eq. 2.10
L_e	Latent heat of evaporation of pure water	
LCL	Lifting condensation level	Sec. 2.3.3
LFC	Level of free convection	Sec. 2.3.3
LNB	Level of neutral buoyancy	Sec. 2.3.3
ln, log	Natural logarithm and logarithm to base 10	
LT	Local time	
m	Complex refractive index	
m, M	Mass of a particle	

m_r, m_u	Mass of rime on an ice particle and mass of unrimed portion	Eq. 2.8
N_B	Brunt-Väisälä frequency	Eq. 2.49
N_n	Number of ice nuclei per liter of air	Eq. 2.7
$n(D)$	Number of particles with diameter between D and dD [m^{-3}]	
n_i, n_l	Number of molecules in solid and liquid phase [m^{-3}]	Eq. 2.6, 2.1
n_p	Number of pulses used for fast Fourier transform	
n_V	Digital output values	Eq. 3.1
n_0	Parameter in Marshall Palmer distribution	Eq. 2.4
p	Pressure	
p	As subscript denoting properties of an air parcel	
PRF	Pulse repetition frequency	
P_r	Received power, time average: $\overline{P}_r$ [W]	
P_t	Power transmitted by radar [W]	
R	Universal gas constant	
R	Rainfall rate [mm h^{-1}]	
r	Correlation coefficient	
r	Distance especially between scatterer and radar	
RAMS	Field campaign: riming, aggregation, and mass of snow	
R_c, R_{ci}	Critical radius for nucleation resp. ice nucleation	Eq. 2.1, 2.6
rH	Relative humidity [%]	
RIM	Degree of riming	
$r_{\max}$	Maximal unambiguous radius	Eq. 2.27
s	As subscript signifying smaller (collected) particle in Eq. 2.10	Eq. 2.10
S	Supersaturation	Eq. 2.2
S_r	Power flux at receiving antenna	
S_t	Flux of transmitted power	
SVS	Snow video spectrograph	
T	Temperature	
t	Time	
Δt	Average time for $\bar{v}_D$	Eq. 4.6
t_a	Time a cell needs to pass over the radar	Eq. 4.4
t_{lag}	Lag time	Sec. 4.1
t_{res}	Radar time resolution	
$u, \vec{u}$	Velocity (vector)	
v	Velocity [m s^{-1}]	
v_a	Velocity of advection [m s^{-1}]	
v_D	Doppler velocity. Mean part: $\bar{v}_D$ [m s^{-1}]	
$v_{D,\mathrm{radar}}$	v_D by radar. $\langle v_{D,\mathrm{radar}} \rangle_{2\,\mathrm{km}}$ averaged over 2 km height layer	
$v_{D,\mathrm{HVSD}}$	v_D computed from HVSD data	

v_h	Horizontal wind velocity [m s^{-1}]	
v_{Ny}	Nyquist velocity [m s^{-1}]	Eq. 2.35
V_{res}	Radar resolution volume	
v_{res}	Radar velocity resolution	
v_T	Terminal fall velocity. v_T' fluctuating and $\bar{v}_T$ mean part [m s^{-1}]	
w	As subscript signifying water	
w	Vertical wind velocity (positive updraft). w' fluctuating, $\bar{w}$ mean part	
$\langle w \rangle_{2\mathrm{km}}$	Vertical wind for 2 km thick layer (Sec. 4.2)	
w_D	Second moment of Doppler spectrum	
w_{max}	Maximal wind that can be caused by CAPE	
WMO	World meteorological organization	
Z	Short for Z$_e$; in practice often called reflectivity	
z	Vertical axis	
Z_e	Effective reflectivity factor	Eq. 2.24
Z_{HVSD}	Reflectivity computed from HVSD data	Eq. 3.3
Z_v	Reflectivity of particles with velocity between v and $v + dv$	
Z_w	Rayleigh (spherical water drops) reflectivity factor	
α_{tilt}	Tilt of radar	
α_a	Angle of advection	
α_i	Shape parameter for nucleated ice particle	Eq. 2.6
α_{wind}	Wind direction	
β_i	Shape parameter for nucleated ice particle	Eq. 2.6
Δ_D	Doppler delta	Sec. 4.3.5
η	Reflectivity (cross section per unit volume)	
Γ, Γ_s	Dry and saturated-adiabatic lapse rate	Eq. 2.42, 2.43
κ	Convection index by Mosimann et al. (1994)	Eq. 4.5
Λ	Parameter in Marshall Palmer distribution	Eq. 2.4
λ	Electromagnetic wavelength	
ρ, ρ_a, ρ_v	Density of a fluid and air density and water vapor density	
$\rho_{w,\mathrm{sat}}$	Saturation density of water vapor in air	
σ	Standard deviation	Eq. B.2
σ, σ_b	Scattering and back scattering cross section	
σ_{il}, σ_{vi}	Free energy of ice-liquid and vapor-liquid interface	Eq. 2.6, Eq. 2.1
τ_p	Duration of radar pulse	
Θ	Beam opening angle	
θ, φ	Angels of position in radar beam	Eq. 2.3
θ, θ_v	Potential and virtual potential temperature	
Φ	Phase	
Ω	Surface area	

Appendix B

Statistics

This section gives a short overview over the statistical definitions, which are used in this thesis. For more details see, e.g., Stahel (1999).

Braces betoken sets of data, e.g. $\{x_i\}$. The average or mean value of a data set $\{x\}$ is defined as

$$\bar{x} = \sum_{i=1}^{n} x_i \quad .$$ (B.1)

The standard deviation

$$\sigma\{x_i\} = \frac{1}{n-1} \sum_i (x_i - \bar{x})^2$$ (B.2)

is a measure for the scatter of data. Based on the standard deviation one can define the correlation r (Eq. B.3) between two data sets $\{x_i\}$ and $\{y_i\}$:

$$r = \frac{1}{n-1} \sum_j \frac{(x_j - \bar{x})(y_j - \bar{y})}{\sigma\{x_i\} \cdot \sigma\{y_i\}} \quad .$$ (B.3)

The correlation ranges between -1 and 1, and is a measure for the linear connection between these two data sets.

Compared to the average, the median, $med(x)$, gives a more stable method and minimizes the influence of outliers:

$$\text{med(x)} = \begin{cases} \{x_{[(n+1)/2]} & n \text{ uneven} \\ \frac{1}{2}(x_{[n/2]} + x_{[n/2+1]}) & n \text{ even} \end{cases} \quad .$$ (B.4)

The rank of a value

$$rank(x_i) = 1 + number\{j\,|\,x_j < x_i\} + \frac{1}{2}number\{j\,|\,\neq i\,and\,x_j = x_i\} \qquad \text{(B.5)}$$

in a data set describes the position in which the value is in an ordered data set. The rank is used in the Spearman rank correlation, r^{Sp} (Eq. B.3), which is a test not for linear but for the monotone relation between two data sets $\{x_i\}$ and $\{y_i\}$. It is defined as the normal correlation of the ranks of the x_i and y_i. Thus its value also ranges between -1 and 1.

$$r^{(Sp)} = \frac{1}{n-1}\sum_j \frac{(rank(x_j) - \frac{n+1}{2})(rank(y_j) - \frac{n+1}{2})}{sd\{rank(x_i)\} \cdot sd\{rank(y_i)\}} \qquad \text{(B.6)}$$

The p-value is a measure for the significance of a correlation, i.e. a test of a certain null hypothesis is performed. If the p-value is smaller than a given significance level, the null hypothesis can be discarded and this gives a stronger significance to the correlation. Table B.1 gives an interpretation of several significance levels (cf. Stahel, 1999). For the test of the significance of correlations in this thesis, the assumption of a correlation coefficient $r = 0$ has been used as null hypothesis .

Table B.1: *Classes of significance for different p-values.*

p-value	interpretation
$p > 0.05$	not significant
$0.05 \geq p > 0.01$	weakly significant
$0.01 \geq p > 0.001$	strongly significant
$0.001 \geq p$	very strongly significant

Bibliography

Atlas, D., Srivastava, R. C., and Sekhon, R. S. (1973). Doppler radar characteristics of precipitation at vertical incidence. *Reviews of Geophysics*, 11(1):1–35.

Barthazy, E., Göke, S., Schefold, R., and Högl, D. (2004). An optical array instrument for shape and fall velocity measurements of hydrometeors. *Journal of Atmospheric and Oceanic Technology*, 21(9):1400–1416.

Barthazy, E. and Joss, J. (2000). Air motion, estimated by vertically pointing radars. *Physics and Chemistry of the Earth Part B-Hydrology Oceans and Atmosphere*, 25(10-12):1209–1214.

Battan, L. J. (1973). *Radar observation of the atmosphere*. The University of Chicago Press, Chicago.

Battan, L. J. and Theiss, J. B. (1966). Observations of vertical motions and particle sizes in a thunderstorm. *Journal of the Atmospheric Sciences*, 23(1):78–87.

Battan, L. J. and Theiss, J. B. (1968). Detection of hail by means of Doppler radar. sci. rept. no. 24. Technical report, Inst. Atmos. Phys., Univ. of Ariz.

Bentley, A. and Humphreys, W. J. (1931). *Snow crystals*. Wilson.

Black, R. A. and Hallett, J. (1998). The mystery of cloud electrification. *American Scientist*, 86(6):526–534.

Böhm, H. P. (1989). A general equation for the terminal fall speed of solid hydrometeors. *Journal of the Atmospheric Sciences*, 46(15):2419–2427.

Born, M. and Wolf, E. (1964). *Principles of optics electromagnetic theory of propagation, interference and diffraction of light*. Pergamon Press, Oxford, 2. rev. edition.

Borys, R. D. (2003). Snow video spectrometer operations manual. Technical report, Storm Peak Laboratory, Desert Research Institute.

Borys, R. D., Lowenthal, D. H., Cohn, S. A., and Brown, W. O. J. (2003). Mountaintop and radar measurements of anthropogenic aerosol effects on snow growth and snowfall rate. *Geophysical Research Letters*, 30(10):art. no.–1538.

Bringi, V. N. and Chandrasekar, V. (2001). *Polarimetric doppler weather radar principles and applications*. Cambridge University Press, Cambridge.

Byers, H. R. and Braham, jr., R. R. (1949). The thunderstorm. *U.S. Gov. Printing Office*, page 287.

Colbeck, S., on Snow, I. C., and on Snow Classification, I. W. G. (1990). *The international classification for seasonal snow on the ground*. International Commission on Snow and Ice of the International Association of Scientific Hydrology, [Hanover, NH].

Collett, J. L. J. and Steiner, M. (1992). Investigations of the relationship between cloudwater and precipitation chemestry using Doppler radar. In Schwartz, S. E. and Slinn, W. G. N., editors, *Precipitation scavenging and atmosphere-surface exchange*, page 3 vol. Hemisphere Publishing Corporation, Washington.

Cooper, W. E., Sand, W. R., Politovich, M. K., and Veal, D. L. (1984). Effects of icing on performance of research aircraft. *J. Aircr.*, 21:708–715.

Dixon, R. W., Mosimann, L., Oberholzer, B., Staehelin, J., and Waldvogel, A. (1995). The effect of riming on the ion concentrations of winter precipitation I: A quantitative-analysis of field-measurements. *Journal of Geophysical Research-Atmospheres*, 100(D6):11517–11527.

Doviak, R. J. and Zrnić, D. S. (1993). *Doppler radar and weather observations*. Academic Press, San Diego, CA [etc.], 2. edition.

Emanuel, K. A. (1994). *Atmospheric convection*. Oxford University Press, New York [etc.].

Fletcher, N. H. (1962). *The physics of rainclouds*. University Press, Cambridge.

Göke, S. (1999). *Microphysics of the Melting Layer*. PhD thesis, ETH Zürich. Diss. No. 13352.

Hallett, J. and Mossop, S. C. (1974). Production of secondary ice particles during riming process. *Bulletin of the American Meteorological Society*, 55(6):679–679.

Harimaya, T. and Nakai, Y. (1999). Riming growth process contributing to the formation of snowfall in orographic areas of japan facing the japan sea. *Journal of the Meteorological Society of Japan*, 77(1):101–115.

Harimaya, T. and Sato, M. (1989). Measurement of the riming amount on snowflakes. *Jour. Fac. Sci. Hokkaido Univ. Ser.*, 8(4):355–366.

Herzegh, P. H. and Hobbs, P. V. (1981). The mesoscale and microscale structure and organization of clouds and precipitation in mid-latitude cyclones IV: Vertical air motions and microphysical structures of prefrontal surge clouds and cold-frontal clouds. *Journal of the Atmospheric Sciences*, 38(8):1771–1784.

Heymsfield, A. J. and Kajikawa, M. (1987). An improved approach to calculating terminal velocities of plate-like crystals and graupel. *Journal of the Atmospheric Sciences*, 44(7):1088–1099.

Hobbs, P. V., Matejka, T. J., Herzegh, P. H., Locatelli, J. D., and Houze, R. A. (1980). The mesoscale and microscale structure and organization of clouds and precipitation in midlatitude cyclones I: A case-study of a cold-front. *Journal of the Atmospheric Sciences*, 37(3):568–596.

Houghton, H. G. (1968). On precipitation mechanisms and their artifical modification. *J. Appl. Meteor.*, 7:851–859.

Houze, R. A. (1993). *Cloud dynamics.* Academic Press, San Diego.

Houze, R. A. (1997). Stratiform precipitation in regions of convection: A meteorological paradox? *Bulletin of the American Meteorological Society*, 78(10):2179–2196.

Houze, R. A., Hobbs, P. V., Biswas, K. R., and Davis, W. M. (1976). Mesoscale rainbands in extratropical cyclones. *Mon.Wea.Rev.*, 104:868–878.

Houze, R. A. and Medina, S. (2003). Orographic enhancement of precipiation in midlatitudes: Results from map and improve II. In *ICAM/MAP*, pages 1–3, Brig, Switzerland.

Hultgren, P. (2002). Triggering of convection. DM-88, Department of Meteorology Stockholm University.

Joss, J. and Waldvogel, A. (1967). Ein Spektrograph für Niederschlagstropfen mit automatischer Auswertung. *Pure Appl. Geophys.*, 68:240–246.

Klaassen, W. (1983). Accurate determination of vertical air velocities in rain by doppler-radar. *Journal of Climate and Applied Meteorology*, 22(10):1788–1793.

Klaassen, W. (1988). Radar observations and simulation of the melting layer of precipitation. *Journal of the Atmospheric Sciences*, 45(24):3741–3753.

Korolev, A. V. and Mazin, I. P. (2003). Supersaturation of water vapor in clouds. *Journal of the Atmospheric Sciences*, 60(24):2957–2974.

Lew, J. K., Montague, D. C., Pruppacher, H. R., and Rasmussen, R. M. (1986). A wind-tunnel investigation on the riming of snowflakes I: Porous disks and large stellars. *Journal of the Atmospheric Sciences*, 43(21):2392–2409.

Liljequist, G. H. and Cehak, K. (1984). *Allgemeine Meteorologie.* Vieweg, Braunschweig, 3. edition.

List, R. (1965). In *Cloud Phys. Conf.*, page 481, Tokyo. Meteor. Soc. of Japan.

Locatelli, J. D. and Hobbs, P. V. (1974). Fall speeds and masses of solid precipitation particles. *Journal of Geophysical Research*, 79(15):2185–2197.

Löffler-Mang, M. and Blahak, U. (2001). Estimation of the equivalent radar reflectivity factor from measured snow size spectra. *Journal of Applied Meteorology*, 40(4):843–849.

Ludlam, F. H. (1958). The hail problem. *Nubila*, 1(12):12–96.

Magono, C. and Lee, C. W. (1966). Meteorological classification of natural snow crystals. *Jour. Fac. Sci., Hokkaido Univ. Ser.*, VII:322–335.

Marshall, J. S. and Palmer, W. M. (1948). The distribution of raindrops with size. *Journal of Meteorology*, 5(4):165–166.

Mie, G. (1908). Beiträge zur Optik trüber Medien, speziell kolloidaler Metallösungen. *Ann. Phys.*, 25:377–445.

Mitchell, D. L., Zhang, R., and Pitter, R. L. (1990). Mass-dimensional relationships for ice particles and the influence of riming on snowfall rates. *Journal of Applied Meteorology*, 29(2):153–163.

Mosimann, L. (1995). An improved method for determining the degree of snow crystal riming by vertical Doppler radar. *Atmospheric Research*, 37(4):305–323.

Mosimann, L., Weingartner, E., and Waldvogel, A. (1994). An analysis of accreted drop sizes and mass on rimed snow crystals. *Journal of the Atmospheric Sciences*, 51(11):1548–1558.

Mosimann, L. R. (1994). *Die Bestimmung der Verreifung von Schneekristallen mittels vertikalem Doppelerradar*. PhD thesis, ETH Zürich. Diss. Nr. 10510.

Pinsky, M. B. and Khain, A. P. (1998). Some effects of cloud turbulence on water-ice and ice-ice collisions. *Atmospheric Research*, 48:69–86.

Poulida, O., Schwikowski, M., Baltensperger, U., Staehelin, J., and Gaeggeler, H. W. (1998). Scavenging of atmospheric constituents in mixed phase clouds at the high-alpine site Jungfraujoch - part II. influence of riming on the scavenging of particulate and gaseous chemical species. *Atmospheric Environment*, 32(23):3985–4000.

Pruppacher, H. R. and Klett, J. D. (1997). *Microphysics of clouds and precipitation*. Kluwer Academic Publishers, Dordrecht, 2nd edition.

Rango, A., Foster, J., Josberger, E. G., Erbe, E. F., Pooley, C., and Wergin, W. P. (2003). Rime and graupel: Description and characterization as revealed by low-temperature scanning electron microscopy. *Scanning*, 25(3):121–131.

Rinehart, R. E. (1999). *Radar for meteorologists or you, too, can be a radar meteorologist, part III.* Rinehart Publications, Grand Forks, ND, 3. edition.

Saunders, C. P. R. and Hosseini, A. S. (2001). A laboratory study of the effect of velocity on Hallett-Mossop ice crystal multiplication. *Atmospheric Research*, 59:3–14.

Schaefer, V. (1956). The preparation of snow crystal replicas. *Weatherwise*, 9:132–135.

Schefold, R. (2004). *Messungen von Schneeflocken: Die Fallgeschwindigkeit und eine Abschätzung weiterer Grössen.* PhD thesis, ETH Zürich. Diss. Nr. 15431.

Scott, B. C. (1978). Parameterization of sulfate removal by precipitation. *Journal of Applied Meteorology*, 17(9):1375–1389.

Seifert, A. (2002). *Parametrisierung wolkenmikrophysikalischer Prozesse und Simulation konvektiver Mischwolken.* PhD thesis, University of Karlsruhe.

Smith, P. L. (1984). Equivalent radar reflectivity factors for snow and ice particles. *Journal of Climate and Applied Meteorology*, 23(8):1258–1260.

Smith, R. (1979). The influence of mountains on the atmosphere. *Adv. Geophys.*, 21:87–230.

Smolarkiewicz, P. K. and Rotunno, R. (1989). Low froude-number flow past 3-dimensional obstacles i: Baroclinically generated lee vortices. *Journal of the Atmospheric Sciences*, 46(8):1154–1164.

Stahel, W. A. (1999). *Statistische Datenanalyse eine Einführung für Naturwissenschaftler.* Vieweg, Braunschweig, 2. edition.

Vohl, O., Mitra, S. K., Wurzler, S. C., and Pruppacher, H. R. (1999). A wind tunnel study of the effects of turbulence on the growth of cloud drops by collision and coalescence. *Journal of the Atmospheric Sciences*, 56(24):4088–4099.

Waldvogel, A. (1974). N0 jump of raindrop spectra. *Journal of the Atmospheric Sciences*, 31(4):1067–1078.

WMO (1992). *International meteorological vocabulary.* Secretariat of the World Meteorological Organization (WMO), Geneva, Switzerland, 2 edition.

Wüest, M. (2001). *Dealiasing wind information from Doppler radar for operational use.* PhD thesis, ETH Zürich. Diss. Nr. 14378.

Wüest, M., Schmid, W., and Zawadzki, I. (1999). Improving single-doppler wind retrievals with secondary wind field data. In *Preprints, 29th International Conference on Radar Meteorology, Montreal, Quebec, Canada*, pages 138–141.

Zawadzki, I. (1991). A method for real-time dealiasing of very noisy clear air doppler data. In *Preprints 25th International Radar Conference, Paris*, pages 879–881.

Zawadzki, I., Fabry, F., and Szyrmer, W. (2001). Observations of supercoled water and secondary ice generation by a vertically pointing x-band doppler radar. *Atmospheric Research*, 59:343–359.

Zikmunda, J. and Vali, G. (1972). Fall patterns and fall velocities of rimed ice crystals. *Journal of the Atmospheric Sciences*, 29(7):1334–1347.

List of Figures

List of Tables

Curriculum vitae

Björn Roland Baschek
Born on 04 May 1974 in Heidelberg, Germany
E-mail: Bjoern.Baschek@alumni.ethz.ch

Education and work:

Oct 2001 - Nov 2004	Ph.D. student at the Swiss Federal Institute of Technology (ETH), Zürich Institute for Atmospheric and Climate Science
Nov 2002	Short Course on Polarimetric - Doppler Radar for Weather Observations and Analysis, Neuss, Germany
Nov 2000 - Dec 2000	Internship on rain sensors Robert Bosch GmbH, Bühlertal, Germany
Jun 2000 - Oct 2000	Internship on Optical Coherence Tomography ZEISS Humphrey Systems, Dublin, California, USA
May 2000	Diploma in physics
May 2000	Certificate in interdisciplinary environmental studies University of Heidelberg, Germany
Apr 1999 - Apr 2000	Diploma thesis "Development of a Hartmann-Shack wavefront sensor for sphero-cylindrical precorrected measurements of the human eye" Kirchhoff Institute for Physics, University of Heidelberg, Germany
Mar 1997 - Feb 1998	ERASMUS-exchange student, University of Uppsala, Sweden partly scholarship by Mälardalen University, Eskilstuna, Sweden Project work on "Atomic Force Microscopy study of proteins adsorbed on mica and antibody antigen docking" at ion physics group
1994 - 2000	Studies of physics at the University of Heidelberg
1984 - 1993	Gymnasium, Neckargemünd, Germany
1980 - 1984	Elementary school, Neckargemünd, Germany

International Conferences:

Sep 2004	German, Austrian, Swiss Meteorology Conference (DACH 2004)
	Karlsruhe, Germany
Jul 2004	14th International Conference on Clouds an Precipitation, Bologna, Italy
Aug 2003	31th Conference on Radar Meteorology, Seattle, WA, USA
May 2003	ICAM/MAP Meeting, Brig, Switzerland
Nov 2002	2nd European Conference on Radar Meteorology, Delft, Neatherlands
Jun 2002	11th Conference on Cloud Physics, Ogden, Utah, USA

Field campaigns:

Winter 2003/2004	Riming, Aggregation, and Mass of Snow (RAMS II) and
	Cloud and Aerosol Characterization Experiment (CLACE 3)
	Jungfraujoch, Switzerland
Winter 2002/2003	Riming, Aggregation, and Mass of Snow (RAMS I)
	Mt. Rigi, Mt. Üetliberg, Switzerland
Summer 2002	Vertical Exchange and Orography (VERTIKATOR)
	part: Alps, Germany
Summer 2002	Vertical Exchange and Orography (VERTIKATOR)
	part: Black Forest, Germany
Winter 2001/2002	Riming, Aggregation, and Mass of Snow (RAMS I)
	Mt. Rigi, Mt. Üetliberg, Switzerland

List of publications:

Baschek, B., R. Schefold, and E. Barthazy, 2004: Wie beeinflussen Aufwinde und eingebettete Konvektionszellen die Bereifung? *Preprints, German, Austrian, Swiss Meteorology Conf. (DACH 2004), Karlsruhe, Germany.*

Baschek, B., R. Schefold, and E. Barthazy, 2004: How do updrafts and embedded convection influence riming? *Proceedings, 14th Int. Conf. on Clouds and Precipitation, Bologna, Italy.*

Baschek, B., R. Schefold and E. Barthazy, 2004: How do updrafts and embedded convection influence riming? *Preprints, 3rd Europ. Conf. on Radar Meteorology, Visby, Sweden.*

Baschek, B., R. Schefold, M. Wüest, and E. Barthazy, 2003: Influence of embedded convection on microphysics of snowfall. *Preprints, 31th Conf. on Radar Meteorology, Seattle, WA, USA.*

Baschek, B., R. Schefold, and E. Barthazy, 2003: Influence of embedded convection on microphysics of precipitation. *Preprints, ICAM/MAP Meeting, Brig, Switzerland.*

Baschek, B., R. Schefold, M. Wüest, and E. Barthazy, 2002: Influence of embedded convection on microphysics of precipitation. *Preprints, 11th Conf. on cloud physics, Ogden, UT, USA.*

Baschek, B., 2000: Entwicklung eines Hartmann-Shack-Wellenfrontsensors für sphäro-zylindrisch vorkorrigierte Messungen am menschlichen Auge. *Diploma thesis, Nr. HD-KIP 00-09, University of Heidelberg.*

Wille, V. and B. Baschek, 1996: Ergebnisse der Gänsezählungen im Winter 1992/93 und 1993/94 *Charadrius 32, p. 1-7.*

Schefold, R., B. Baschek, A. Bansemer, and E. Barthazy, 2004: Combined measurements of snowflake characteristics in the melting layer. *Proceedings, 14th Int. Conf. on Clouds and Precipitation, Bologna, Italy.*

Schefold, R., B. Baschek, M. Wüest, and E. Barthazy, 2002: Fall velocity and axial ratio of snowflakes *Proceedings, 2nd Europ. Conf. on Radar Meteorology, Delft, Netherlands.*

Schefold, R., B. Baschek, M. Wüest, and E. Barthazy, 2002: Fall velocity and axial ratio of snowflakes in a wide size and habit range. *Preprints, 11th Conf. on cloud physics, Ogden, UT, USA.*

Wüest, M., B. Baschek, R. Schefold, and E. Barthazy, 2002: About the use of wind field retrievals from Doppler radar for dynamical analyses of stratiform snowfall. *Preprints, 11th Conf. on cloud physics, Ogden, UT, USA.*

Acknowledgements